

Copyright  
by  
Yafis Barlas  
2008

The Dissertation Committee for Yafis Barlas  
certifies that this is the approved version of the following dissertation:

## Role of electron-electron interactions in Chiral 2DEGs

Committee:

---

Allan H MacDonald, Supervisor

---

Alex Demkov

---

Qian Niu

---

Maxim Tsoi

---

James Chelikowsky

**Role of electron-electron interactions in Chiral 2DEGs**

by

**Yafis Barlas, B.S.; M.A.**

**DISSERTATION**

Presented to the Faculty of the Graduate School of  
The University of Texas at Austin  
in Partial Fulfillment  
of the Requirements  
for the Degree of

**DOCTOR OF PHILOSOPHY**

THE UNIVERSITY OF TEXAS AT AUSTIN

August 2008

Dedicated to Ammi, Abbu and Amma.

# Acknowledgments

I have been fortunate to work with Prof. Allan H MacDonald, who has been an excellent teacher, mentor and friend. He taught me physics that cannot be learnt from textbooks, and his intuition and deep insight in condensed matter theory has been a source of inspiration to me. I am specially indebted to his extraordinary degree of patience, kindness and sense of humor. He is not only a great physicist but also one of the best people I have known.

I would also like to thank my collaborators: Tami Pareg-Berena, Marco Polini, Reza Asgari, Rene Cote and especially Kentaro Nomura, without whom this work would not have been possible. I would also like to acknowledge discussions and support from our group members: Paul Haney, Dagim Tilahun, Hongki Min, Ion Garate, Wei-Cheng Lee, Zhang Fan, Alvaro Nunez, Jason Hill, Murat Tas and Sergey Maslennikov. I would especially like to thank Becky Drake for patience, kindness and immense help she provided during my work with the group. I would also like to thank Prof. Alex Demkov, Maxim Tsoi, Jim Chelikowsky and Qian Niu for taking the time to be on my dissertation committee.

I would like to thank my Jibroni friends and friends from the climbing wall for friendship and support. The road trips we took over weekends and breaks were essential to my morale. I could not have asked for better company on top of the Colorado fourteeners and New Mexico's peaks.

Finally I would like to thank my family especially my parents for their uncon-

ditional love and support through out the course of my life. Your financial and emotional sacrifices especially during my study in the States will never be forgotten. You have always been close to my heart, mere words cannot convey my immense gratitude and love.

# Role of electron-electron interactions in Chiral 2DEGs

Publication No. \_\_\_\_\_

Yafis Barlas, Ph.D.

The University of Texas at Austin, 2008

Supervisor: Allan H MacDonald

In this thesis we study the effect of electron-electron interactions on Chiral two-dimensional electron gas (C2DEGs). C2DEGs are a very good description of the low-energy electronic properties of single layer and multilayer graphene systems. The low-energy properties of single layer and multilayer graphene are described by Chiral Hamiltonians whose band eigenstates have definite chirality. In this thesis we focus on the effect of electron-electron interactions on two of these systems: monolayer and bilayer graphene.

In the first half of this thesis we use the massless Dirac Fermion model and random-phase-approximation to study the effect of interactions in graphene sheets. The interplay of graphene's single particle chiral eigenstates along with electron-electron interactions lead to a peculiar suppression of spin susceptibility and compressibility, and also to an unusual velocity renormalization. We also report on a theoretical study of the influence of electron-electron interactions on ARPES spectra in graphene. We find that level repulsion between quasiparticle and plasmaron resonances gives rise to a gap-like feature near

the Dirac point.

In the second half we anticipate interaction driven integer quantum Hall effects in bilayer graphene because of the near-degeneracy of the eight Landau levels which appear near the neutral system Fermi level. We predict that an intra-Landau-level cyclotron resonance signal will appear at some odd-integer filling factors, accompanied by collective modes which are nearly gapless and have approximate  $q^{3/2}$  dispersion. We speculate on the possibility of unusual localization physics associated with these modes.

# Table of Contents

<b>Acknowledgments</b>	<b>v</b>
<b>Abstract</b>	<b>vii</b>
<b>List of Tables</b>	<b>xi</b>
<b>List of Figures</b>	<b>xii</b>
<b>Chapter 1. Introduction</b>	<b>1</b>
1.1 Outline of the thesis . . . . .	3
<b>Chapter 2. Two dimensional Chiral Hamiltonians</b>	<b>6</b>
2.1 Graphene . . . . .	8
2.1.1 Low energy theory of graphene . . . . .	12
2.1.2 Cyclotron Mass and Density of States . . . . .	17
2.2 Bilayer Graphene . . . . .	19
2.3 Chiral Fermions in a magnetic field . . . . .	23
2.3.1 Quantum Hall Effect of Chiral Fermions . . . . .	25
<b>Chapter 3. Chirality and Correlations in Graphene</b>	<b>29</b>
3.1 RPA Theory of Graphene . . . . .	35
3.2 Charge and Spin Susceptibilities . . . . .	40
3.3 Discussion . . . . .	43
<b>Chapter 4. Graphene: A Pseudochiral Fermi Liquid</b>	<b>46</b>
4.1 Random Phase Approximation of Self-energy . . . . .	50
4.2 Results . . . . .	53
4.3 Discussions . . . . .	55

<b>Chapter 5. Plasmons and The Spectral Function of Graphene</b>	<b>62</b>
5.1 Introduction . . . . .	62
5.2 Doped Dirac Sea Charge Fluctuations . . . . .	64
5.3 Dirac Quasiparticle Decay . . . . .	66
5.4 Spectral function . . . . .	69
<b>Chapter 6. Quantum Hall Ferromagnets</b>	<b>76</b>
6.1 Review of Quantum Hall Effect . . . . .	77
6.2 Quantum Hall Ferromagnets . . . . .	80
<b>Chapter 7. Octet Quantum Hall Ferromagnets in Bilayer Graphene</b>	<b>87</b>
7.1 Graphene Bilayer Landau Levels . . . . .	88
7.2 Octet Hund's Rules . . . . .	90
7.3 Landau-Level Pseudospin Dipoles . . . . .	93
7.4 Intra-Landau-Level Cyclotron Resonance . . . . .	97
<b>Chapter 8. Conclusion</b>	<b>100</b>
<b>Appendices</b>	<b>103</b>
<b>Appendix A. Graphene's Lindhard Function</b>	<b>104</b>
A.1 Half-Filling . . . . .	105
A.2 Pauli-blocking effects . . . . .	107
<b>Appendix B. Correlation Self-energy of a quasiparticle in graphene</b>	<b>111</b>
<b>Bibliography</b>	<b>114</b>
<b>Index</b>	<b>124</b>
<b>Vita</b>	<b>125</b>

# List of Tables

# List of Figures

2.1	This figure shows an atomic layer of graphene identified using Atomic Force Microscopy . . . . .	10
2.2	(Adapted from [22]) Energy gap vs ribbon width. The inset shows energy gap vs relative angle for the device sets. Dashed lines in the inset represent the value of energy gap as predicted by empirical scaling of energy gap vs ribbon width. . . . .	12
2.3	Left: Lattice structure of graphene composed from two triangular lattices ( $\vec{a}$ and $\vec{b}$ are the lattice vectors), with sublattices A(Blue) and B(Red). Right: Shows the corresponding Brillouin zone. The Dirac cones are located at $K$ and $K'$ . . . . .	13
2.4	(Adapted from [10]) Left: Numerically calculated energy spectrum of graphene (in units if $t$ ). Right: Magnified linear energy dispersion near the Dirac point. . . . .	15
2.5	(Adapted from [10]) Cyclotron mass of quasiparticles in graphene as a function of their concentration( $n$ ), positive and negative $n$ correspond to electron and holes respectively. Experimental data extracted from SdH oscillations. . . . .	18
2.6	Lattice structure of bilayer graphene with a honeycomb lattice constant $a = 2.46A$ and interlayer separation $d = 3.35A$ . . . .	19
2.7	(Adapted from [26]) This figure shows the evolution of gap closing and reopening by changing the doping level by potassium adsorption. Experimental and theoretical bands (solid lines) (A) for an as-prepared graphene bilayer and (B and C) with progressive adsorption of potassium are shown. The number of doping electrons per unit cell, estimated from the relative size of the Fermi surface, is indicated at the top of each panel . . .	23
2.8	(Adapted from [3]) Hall conductivity $\sigma_{xy}$ and longitudinal $\rho_{xx}$ of graphene as a function of the concentration at $B = 14T$ . The inset show bilayer graphene's hall conductivity as a function of concentration. . . . .	27
3.1	Random-phase-approximation in terms of Feynman diagrams.	30
3.2	(Adapted from [10])Particle-hole continuum and collective modes of:(a) 2DEG ;(b) neutral graphene; (c) doped graphene . . . .	32

3.3	Dirac cone for n-doped graphene, the yellow arrows represents the chirality of the bands $s = +(-)$ for clockwise and anti-clockwise, and the red arrows represent particle-hole transitions.	33
3.4	(Color online) Cut-off dependence of the regularized exchange energy $\delta\varepsilon_x$ in units of the Fermi energy $\varepsilon_F$ .	37
3.5	(Color online) Cut-off dependence of the regularized correlation energy $\delta\varepsilon_c^{\text{RPA}}$ in units of the Fermi energy $\varepsilon_F$ .	39
3.6	(Color online) Cut off $\Lambda$ and coupling constant $f$ dependence of $\kappa/\kappa_0$ . The color coding is as in Figs. 3.4-3.5.	41
3.7	(Color online) Cut-off $\Lambda$ and coupling constant $f$ dependence of the spin susceptibility $\chi_S$ . The color coding is as in Figs. 3.4-3.5.	42
4.1	Honeycomb lattice of a single layer graphite flake with one sublattice in yellow and the other sublattice in blue. In the continuum limit the sublattice degree of freedom may be regarded as a pseudospin. When momentum $\mathbf{k}$ is measured away from the Dirac points at the $K$ and $K'$ Brillouin zone corners, band eigenstates have definite projection of pseudospin in the $\mathbf{k}$ direction, <i>i.e.</i> definite pseudochirality. The angle $\phi_{\mathbf{k}}$ above denotes the momentum-dependent phase difference between wavefunction amplitudes on the two sublattices. For spin-1/2 quantum particles this angle is the azimuthal orientation of a pseudospin coherent state in the equatorial plane.	58
4.2	In a weakly doped material, graphene's energy bands can be described by a massless Dirac equation in which the role of spin is played by pseudospin. Like an ordinary 2DES, doped graphene has a circular Fermi surface. The Fermi liquid properties of graphene are a consequence of both exchange interactions between quasiparticles near the Fermi surface and states in the positive and negative energy Fermi seas and of interactions with both intra-band (short red vertical arrow) and inter-band (long red vertical arrow) virtual fluctuations of the electronic system. The yellow arrows in this figure indicate the pseudospin chirality of band eigenstates. Because of the difference in chirality between positive and negative energy bands, the velocity of graphene quasiparticles is enhanced by inter-band exchange interactions, tending to protect the system from magnetic and other instabilities, and reducing both charge and spin response functions.	59

- 4.3 “Lindhard” function  $\chi^{(0)}(\mathbf{q}, i\Omega)$  of a C2DES, in units of the non-interacting density-of-states at the Fermi surface  $\nu = gk_F/(2\pi v)$ , as a function of  $q/k_F$  and  $\Omega/\mu$  on the imaginary frequency axis.  $k_F = (4\pi n/g)^{1/2}$  is the Fermi wavenumber,  $\mu = vk_F$  the Fermi energy,  $n$  the electron density and the flavor multiplicity  $g = g_s g_v = 4$  for graphene because of its two-fold valley degeneracy. Because of interband fluctuations  $\chi^{(0)}$  diverges linearly with  $q$  for  $q \rightarrow \infty$  and decays only like  $\Omega^{-1}$  for  $\Omega \rightarrow \infty$  in the C2DES, in contrast to the  $q^{-2}$  and  $\Omega^{-2}$  behaviors of the ordinary 2DES. In the static  $\Omega = 0$  limit  $\chi^{(0)}(\mathbf{q}, 0) = -\nu$  for all  $q \leq 2k_F$  for both chiral and ordinary 2DESs. . . . . 60
- 4.4 Density and coupling constant  $f$  dependence of some C2DES Fermi-liquid parameters. The density is specified by  $\Lambda \equiv q_c/k_F$ . The density range studied most extensively in experiment,  $n \sim 10^{11} \text{ cm}^{-2}$  to  $n \sim 10^{13} \text{ cm}^{-2}$ , corresponds to  $\Lambda = 100$  to  $\Lambda = 10$ . In all panels the black solid line corresponds to the highest value of the cut-off parameter we have considered,  $\Lambda = 2.7 \times 10^5$ . The red dashed line illustrates the RPA Fermi-liquid parameters of an ordinary non-chiral 2DES with parabolic bands. In this case the  $f = \sqrt{2} r_s$  [see Eq. (4.11)], where  $r_s = (\pi n a_B^2)^{-1/2}$  is the usual Wigner-Seitz density parameter and  $a_B = \epsilon \hbar^2 / (m_b e^2)$  the effective Bohr radius. From the left the three panels show: (a) the quasiparticle renormalization factor  $Z$  evaluated from Eq. (4.7); (b) the velocity renormalization factor evaluated from Eq. (4.8); and (c) the  $\ell = 0$  dimensionless Landau parameter  $F_0^a$  which characterizes spin-dependent quasiparticle interactions. The color coding for  $\Lambda$  is the same in all panels. . . . . 61
- 5.1 Spectral function  $\mathcal{A}(\mathbf{k}, \omega)$  of an n-doped graphene sheet as a function of  $k$  (in units of Fermi wavevector  $k_F$ ) and  $\omega$  (in units of and measured from the Fermi energy  $\hbar v k_F$  where  $v$  is the Fermi velocity). These results are for coupling constant  $\alpha_{\text{gr}} = g e^2 / (\epsilon \hbar v) = 2$  (here  $g = 4$  is a spin-valley degeneracy factor and the dielectric constant  $\epsilon$  depends on the material which surrounds the graphene layer). For each  $k$  ARPES detects the portion of the spectral function with  $\omega < 0$ . The  $k$ -dependence is represented in this figure by results for twenty discrete  $k \in [0.0, 0.95]$ . . . . . 72
- 5.2 Left panel:  $-\Im m[\varepsilon^{-1}(\mathbf{q}, \omega)]$  as a function of  $q/k_F$  and  $\omega/\varepsilon_F$  for  $\alpha_{\text{gr}} = 2$ . The solid line is the RPA plasmon dispersion relation. The dashed lines are the boundaries of the electron-hole continuum. Right panel:  $-v_q \Im m[\chi^{(0)}(\mathbf{q}, \omega)]$  as a function of  $q/k_F$  and  $\omega/\varepsilon_F$ . The left and right panels become identical in the non-interacting  $\alpha_{\text{gr}} \rightarrow 0$  limit. . . . . 73

5.3	(Color online) Top left panel: $\omega_{\text{pl}}^*$ (solid line) and $\Gamma^*$ (filled squares) as functions of $\alpha_{\text{gr}}$ . Other panels: The absolute value $ \Im m[\Sigma_s(\mathbf{k}, \omega)] $ of the imaginary part of the RPA quasiparticle self-energy (in units of $\varepsilon_{\text{F}}$ ) of an n-doped system as a function of energy $\omega$ for $k = 0, 0.25$ , and $0.75$ and $\alpha_{\text{gr}} = 2$ . . . . .	74
5.4	(Color online) $\Re e[\Sigma_+(\mathbf{k}, \omega)]$ , $\Im m[\Sigma_+(\mathbf{k}, \omega)]$ , and spectral function $\mathcal{A}_+(\mathbf{k}, \omega)$ for $k = 0.25$ and $k = 0.75$ . The band energy and $\Re e[\Sigma_+]$ are measured from the band $\varepsilon_{\text{F}}$ and interaction $[\Sigma_+(k_{\text{F}}, \omega = 0)]$ contributions to the chemical potential. . . . .	75
6.1	This figure shows hall plateaus at integer and fractional filling as a function of the magnetic field strength $B$ . . . . .	77
6.2	The direction of the local magnetization is $\vec{m} = (\sin \theta \cos \phi, \sin \theta \sin \theta, \cos \theta)$	81
6.3	Phase diagram of a double layer quantum hall system. The phase boundary indicates the collapse of hall plateau as a function of layer separation and tunnelling. . . . .	85
7.1	(Color online) Filling factor dependence of the integer filling factor HF theory occupied state (spectrum of the bilayer graphene octet at $\Delta_V = 0$ ). Energies of occupied (red - solid lines) and unoccupied (blue - dashed lines) are in units of $(\pi/2)^{1/2} e^2 / \varepsilon l_B$ . The Zeeman field $\Delta_Z$ value in these units is 0.023 at a magnetic field of $20T$ . Octet space fractional pseudospin polarizations offset for clarity: spin (red boxes), valley (green circles) and LL pseudospin (blue triangles). . . . .	92
7.2	Collective mode $\omega_q$ of the Landau-level pseudospin polarized state in units of interaction strength $e^2 / \varepsilon l_B = 11.2 \sqrt{B [\text{Tesla}]} \text{ meV}$ as a function of $q l_B$ at different values of the external potential difference $\Delta_V$ at a magnetic field of 20 T. The black (solid) line indicates the $q l_B \rightarrow \infty$ asymptote for $\Delta_B = 0$ . . . . .	97
A.1	The surface plot shows graphene's Lindhard function for $\tilde{\Omega} = \Omega / \mu$ and $\tilde{q} = q / v$ . . . . .	110

# Chapter 1

## Introduction

The discovery of quantum mechanics in the early twentieth century led to a number of unintuitive and fascinating insights into matter at atomic length scales. It only seems natural to extend the laws of quantum mechanics to assemblies of many atoms and molecules in matter. However a brute force calculation of Schrödinger's equation for just a few particles becomes intractable even on the world's most powerful computers. Condensed matter physics involves study of systems with huge degrees of freedom (of order  $10^{23}$ ) with various couplings between these degrees of freedom (usually due to interactions). For example in a solid the atoms or molecules are close to each other and normally crystallize or form other novel exotic states in order to reduce the interaction energy between each other. It seems we are at an impasse; to understand the nature of these systems we must understand the effect of interactions with a microscopic number of degrees of freedom.

Fortunately, however, we are generally interested in the long distance or low energy physics of these systems and hence only the degrees of freedom that are involved in the low energy excitations of such systems. For example in metals the core electrons are strongly bound to the nuclei and require a high energy for excitation, whereas the conduction electrons which are free to

move are essentially important in low-energy processes such as transport. It is then prudent to ignore the core electrons. In fact when considering a physical process there are always certain low-energy degrees of freedom that are more important than others. Condensed matter systems can then be described by a "low-energy effective theory" by writing an effective Lagrangian involving only the relevant low-energy degrees of freedom. The effect of the high energy physics is to "renormalize" the bare parameters of the low-energy effective theory [1].

Landau's Fermi liquid theory is a perfect example of a low-energy effective theory. The interacting electrons act as weakly interacting "quasiparticles" with renormalized mass and a finite lifetime. In the renormalization group language Landau's Fermi liquid theory is a fixed-point theory parameterized by marginal couplings  $m^*$  (effective mass) with some effective interaction between the quasiparticles. The effect of the high energy physics is encoded in the effective mass and effective interactions. The other manifestation of low-energy effective theory is the "emergence" of a collective coordinate, often called an order parameter. In this case the microscopic degrees of freedom condense into some symmetry broken collective state where the phase can be described by this collective variable or order parameter. Notable examples include superconductivity and ferromagnetism. Here we can also write an effective theory in terms of the order parameter. This leads to the notion of "emergent phenomena" in condensed matter systems[2].

Condensed matter systems also exhibit a wealth of strongly correlated

systems where the notion of "quasiparticle" and "order parameter" breaks down. Common examples of such systems include high  $T_c$  superconductors, heavy fermions, Luttinger liquids and Quantum Hall Systems. For example Quantum Hall Systems have incompressible ground states that support collective excitations with fractional charge and statistics which do not conform to a quasiparticle picture or with a broken symmetry phase. In these systems the kinetic energy is quenched by the magnetic field and electron-electron interactions play a dominant role in determining the low-energy physics. Their low-energy description is then taken into account by model hamiltonians or effective theories in some "dual" sector<sup>1</sup>. Strongly correlated systems are generally related to low dimensionality i.e. they exist in one or two dimensions. This is related to the interesting topological properties of low dimensional space; it seems there is more room for exotic behavior in lower dimensions.

## 1.1 Outline of the thesis

In this thesis we study the effect of electron-electron interactions in graphene sheets. We also study the effect of electron-electron interactions on bilayer graphene in the Quantum Hall regime. These systems can be classified under a general class of systems which will be referred to as Chiral two dimensional electron gas (C2DEGs). Below we describe the contents of each chapter.

---

<sup>1</sup>Jain's composite fermion picture maps Fractional Hall Effect of electrons to Integer Hall Effect of composite fermions using the method of flux attachment, thereby mapping strongly interacting electrons to non-interacting quasiparticles.

**Ch.(2)** introduces the concept of two-dimensional Chiral Fermions and Chiral two-dimensional electron gas (C2DEGs), focusing on the single particle properties of two-dimensional Chiral Fermions. In particular we show that graphene and bilayer graphene fall within this family of C2DEGs with chirality index  $J = 1$  and  $J = 2$  respectively. Towards the end of this chapter we also study two-dimensional Chiral Fermions in a magnetic field.

**Ch.(3)** investigates the influence of electron-electron interactions in doped graphene sheets based on the random-phase-approximation. We show that the tendency of Coulomb interactions in lightly doped graphene to favor states with larger net chirality leads to suppressed spin and charge susceptibilities. Our conclusions are based on an evaluation of graphene's exchange and random-phase-approximation (RPA) correlation energies. This suppression is a consequence of the quasiparticle chirality switch which enhances quasiparticle velocities near the Dirac point.

**Ch.(4)** addresses graphene's Fermi liquid properties quantitatively using a microscopic random-phase-approximation theory. We find a weak doping dependence on the renormalized velocity and quasiparticle spectral weight. We also comment on the importance of using exchange-correlation potentials based on the properties of a chiral two-dimensional electron gas in density-functional-theory applications to graphene nanostructures.

**Ch.(5)** reports on a theoretical study of the influence of electron-electron interactions on ARPES spectra in graphene that is based on the random-phase-approximation and on graphene's massless Dirac equation con-

tinuum model. We find that level repulsion between quasiparticle and plasmaron resonances gives rise to a gap-like feature at small  $k$ . ARPES spectra are sensitive to the electron-electron interaction coupling strength  $\alpha_{\text{gr}}$  and might enable an experimental determination of this material parameter.

**Ch.(6)** reviews the exotic and novel properties of single layer and bilayer Quantum Hall Ferromagnets. We study the the ground state and the neutral low energy collective excitations of Quantum Hall Ferromagnets. We also comment on the topologically charged excitations within these systems.

**Ch.(7)** reports on a study of interaction driven integer quantum Hall effects in bilayer graphene. These systems are of interest due to the near-degeneracy of the eight Landau levels which appear near the neutral system Fermi level. We predict that an intra-Landau-level cyclotron resonance signal will appear at some odd-integer filling factors, accompanied by collective modes which are nearly gapless and have approximate  $q^{3/2}$  dispersion. We speculate on the possibility of unusual localization physics associated with these modes.

Parts of this thesis have been or will be published separately.

## Chapter 2

### Two dimensional Chiral Hamiltonians

In this chapter we discuss a particular class of single particle hamiltonians from here on referred to as Chiral Hamiltonians restricting ourselves to two dimensions. We refer to the quasiparticles described by Chiral Hamiltonian as Chiral Fermions. The main theme of this dissertation is to study the effect of electron-electron interactions in systems where the single particle properties are determined by Chiral hamiltonians in two dimensions. We refer to this collective system as a Chiral two dimensional electron gas (C2DEG).

The single particle Chiral Hamiltonian with chirality index  $J$  can be written as

$$\mathcal{H}_J(\vec{q}) \propto \xi^J q^J [\cos(J\phi_{\vec{q}})\sigma^x + \sin(J\phi_{\vec{q}})\sigma^y], \quad (2.1)$$

where  $\sigma^\alpha$  is a Pauli matrix acting on a pseudospin doublet,  $\vec{q}$  is an envelop function momentum measured from some nodal points in the Brillouin-zone(BZ),  $\xi = \pm$  accounts for the presence of two nodal points  $K$  and  $K'$  in the BZ generally referred to as valley degree of freedom,  $q = |\vec{q}|$  and  $\phi_{\vec{q}} = \tan^{-1}(q_y/q_x)$ . The pseudospin doublets in their respective valleys  $K(\xi = +)$  and  $K'(\xi = -)$  are defined as  $\Phi_{\xi=+1}^\dagger = (\phi_\uparrow^\dagger, \phi_\downarrow^\dagger)$  and  $\Phi_{\xi=-1}^\dagger = (\phi_\downarrow^\dagger, \phi_\uparrow^\dagger)$ . In  $\mathcal{H}_J$   $J$  is the chirality index of the pseudospin doublet. It can be easily seen that the energy

dispersion of 2.1 is  $\epsilon_J(\vec{q}) \propto \pm q^{J/2}$  with chiral band eigenstates:

$$|\pm, \vec{q}\rangle = \frac{1}{\sqrt{2}} \begin{pmatrix} 1 \\ \pm e^{iJ\phi_{\vec{q}}} \end{pmatrix}, \quad (2.2)$$

where the sign  $s = \pm$  of the eigenstate is called the chirality. With our inverted definition of the pseudospin components of the wavefunction, quasiparticles in different valleys have opposite chirality.

In semiconducting language these systems are called zero-gap semiconductors with the positive(negative) energies identified with the conduction(valance) bands. The energy bands exhibit degeneracy points  $K$  and  $K'$  in momentum space where the conduction and valence bands meet. For a neutral structure (i.e undoped with holes or electrons) the Fermi energy lies at the degeneracy points. As we see later time reversal symmetry requires the presence of the two valleys  $K$  and  $K'$ .

The quasiparticles described by  $\mathcal{H}_J$  acquire a Berry phase of  $J\pi$  upon an adiabatic propagation along a closed orbit. This has unusual consequences on the single particle properties of chiral systems most notable of which is the presence of anomalous Half-integer Quantum Hall effect of odd  $J$ , which has been measured in some of these systems [3–5]. We leave discussion of the properties of Chiral fermions in a magnetic field towards of this chapter.

Apart from the single particle properties the existence of chiral eigenstates has interesting consequences on the many-body properties of the system [6–8]. The effects of disorder and electron-electron interactions have recently been an area of intense theoretical and experimental study [9, 10]. As we see through out this thesis the presence of chiral eigenstates has interesting

consequences on the electronic and thermodynamic properties of C2DEGs.

The existence of two valleys is crucial for time reversal symmetry of Chiral hamiltonians. Time reversal symmetry for chiral hamiltonian can be described by  $(\Pi \otimes \sigma_x)\mathcal{H}_J^*(\vec{q})(\Pi \otimes \sigma_x) = \mathcal{H}_J(-\vec{q})$  where  $\Pi$  swaps  $\xi = +1$  and  $\xi = -1$  in valley space. Chiral hamiltonians also satisfy spatial inversion symmetry given by  $(\Pi \otimes \sigma_0)\mathcal{H}_J(\vec{q})(\Pi \otimes \sigma_0) = \mathcal{H}_J(-\vec{q})$ . Note that vanishing of the energy at the nodal points is essential for the existence of Chiral Hamiltonians. Such a structure can also appear due to Fermi surface nesting properties: for example d-wave superconductors can be described by  $J = 1$  chiral systems [11].

This family of chiral hamiltonians is a good description of the low-energy electronic properties of graphene multilayers, where the stacking sequence of an N-layer graphene system determines the exact decomposition of the chiral pseudospin doublets and the chirality index [12]. A special case of this is monolayer graphene ( $J = 1$  chiral system) [10] and Bernal stacked bilayer graphene ( $J = 2$  chiral system) [13] and remains the focus of this dissertation. Below we show how to derive the low energy properties of single layer and bilayer graphene in the process indicating that they belong to a much wider class of chiral hamiltonians with chirality index  $J = 1, 2$  respectively.

## 2.1 Graphene

Graphene is a two-dimensional array of carbon atoms stacked on a honeycomb lattice that is isolated from its parent compound Graphite by me-

chanical exfoliation[9, 10] . Graphite is a well known and extensively studied three dimensional allotrope of carbon most commonly used in pencils and lubricants. Graphite is composed of stacks of graphene layers weakly coupled together due to van der Waals forces. It was originally assumed that graphene was unstable could not exist in a free state. However the real fact is that even though it is deposited every time one writes with a pencil it is hard to detect as no experimental tool existed to detect a one-atom-thick flake. It was not until the seminal work of researches at University of Manchester [14] that graphene was eventually spotted it due to the subtle optical effect it creates on SiO<sub>2</sub> substrate.

P. R. Wallace [15] was the first person to show that the band structure of graphene exhibits unusual semimetallic behavior. The low energy theory of graphene can be described by massless Dirac Fermions, resembling the physics of quantum electrodynamics(QED) of massless particles with a material specific speed of light  $v_F$  (approximately 300 times smaller than the speed of light in vacuum) [16–18]. Graphene is a condensed matter realization of a relativistic system where many of the unusual properties of QED can show up in graphene at much smaller speeds. Dirac Fermions also behave in unusual ways, compared to ordinary electrons, when subjected to magnetic fields, leading to an anomalous half-integer quantum hall effect(IQHE) [3, 4].

A particularly interesting feature of Dirac fermions is their insensitivity to external electrostatic potentials due to the Klein paradox which states that Dirac fermions can be transmitted with a nonzero probability through a

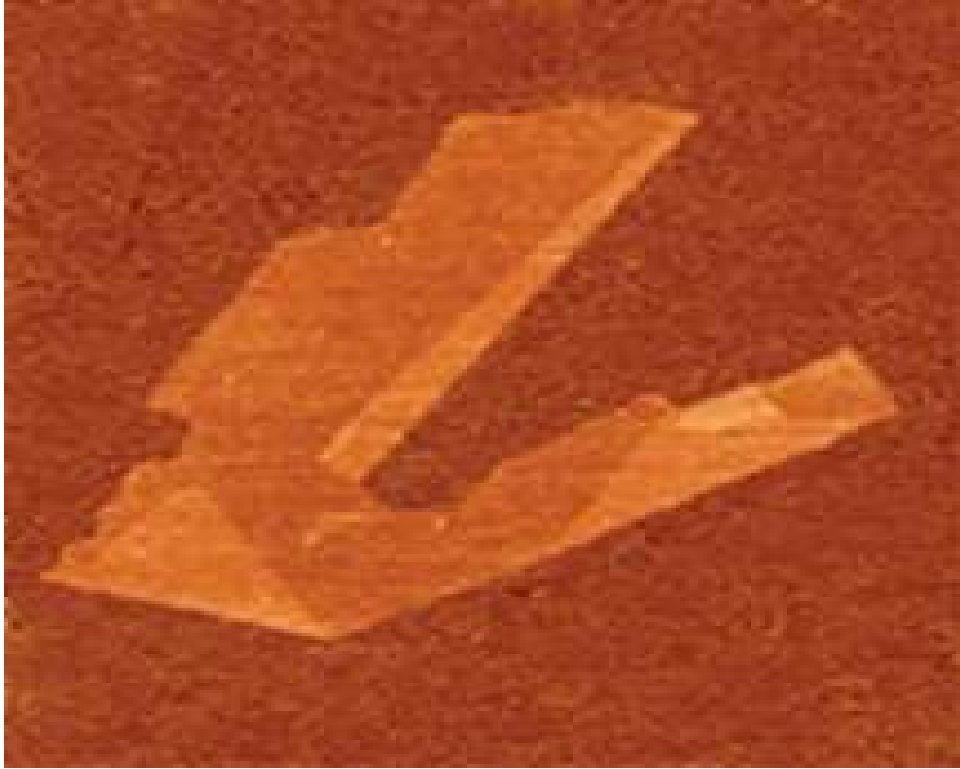


Figure 2.1: This figure shows an atomic layer of graphene identified using Atomic Force Microscopy

classically forbidden region [19, 20]. Due to this fact Dirac fermions behave in an unusual way in the presence of a confining electrostatic potential leading to the phenomenon of *zitterbewegung*, or jittery motion of the wavefunction. Such an electrostatic potential can be generated by disorder, and recent efforts have focused on trying to understand how disorder can effect these massless Dirac quasiparticles and transport properties of graphene [10].

The role of electron-electron interactions is particularly interesting in graphene. As mentioned earlier relativistic quasiparticles in graphene have a

Fermi velocity much smaller than the speed of light, and therefore the electron-electron interactions are non-relativistic long-range Coulomb interactions. The strength of electron-electron interactions in graphene is given by the dimensionless constant  $\alpha_{gr} = e^2/(\epsilon\hbar v_F)$  very different from the density dependent parameter  $r_s$  which determines the strength of interactions in 2DEGs. This interplay of relativistic quasiparticles interacting through long-range Coulomb interaction has interesting consequences most striking of which is the absence of screening in neutral graphene and a peculiar renormalization of Fermi velocity in graphene [8, 21]. We discuss the role of electron-electron interactions in graphene extensively in the up coming chapters.

Apart from the theoretical interest in massless Dirac quasiparticles, graphene might have possible applications in the semiconductor industry. It exhibits very high mobility ( $\mu > 10^4 \text{cm}^2/\text{Vs}$ ), an order of magnitude higher than modern Si transistors [4]. This fact makes graphene a strong candidate for future device applications. The mobility remains high even at the highest electric-field induced concentrations ensuring ballistic transport at submicrometer scale even at room temperature. However the fact that graphene remains metallic at the neutrality point is a hindrance to future device application. Recent work on graphene nanoribbons indicates that a gap can be induced by spatial confinement leading to the possibility of future graphene based transistors [22].

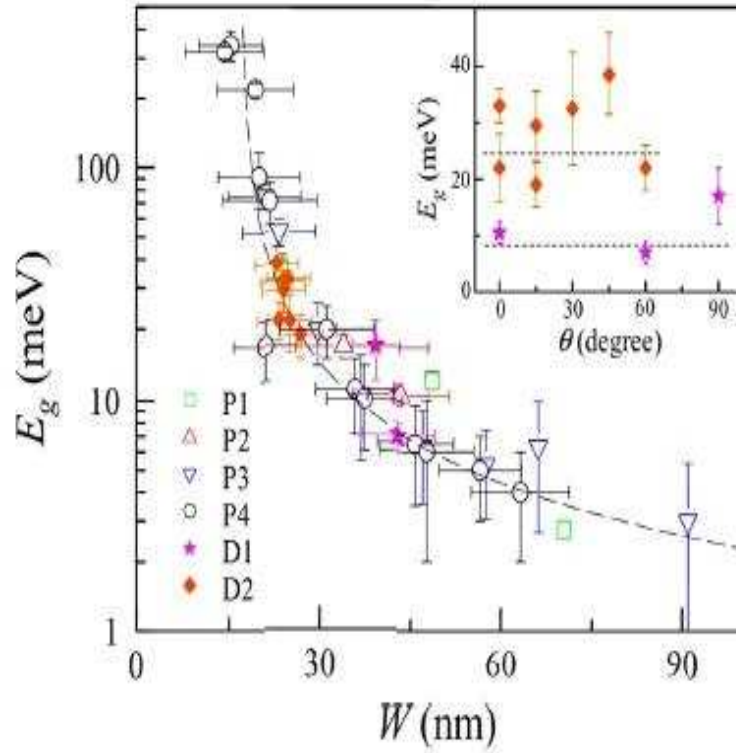


Figure 2.2: (Adapted from [22]) Energy gap vs ribbon width. The inset shows energy gap vs relative angle for the device sets. Dashed lines in the inset represent the value of energy gap as predicted by empirical scaling of energy gap vs ribbon width.

### 2.1.1 Low energy theory of graphene

Graphene is made out of carbon atoms arranged in a hexagonal structure as shown in Figure 2.3. A honeycomb lattice is a textbook example of a non- Bravias lattice usually referred to as a lattice with a basis of two atoms per unit cell [23]. In this section starting from a nearest neighbor tight-binding description of electrons on a planar honeycomb lattice we show how the low-

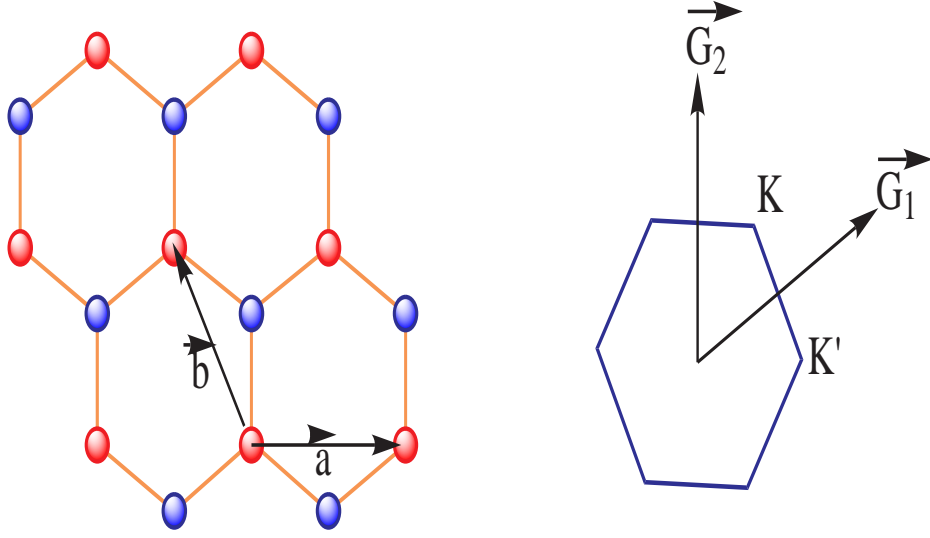


Figure 2.3: Left: Lattice structure of graphene composed from two triangular lattices ( $\vec{a}$  and  $\vec{b}$  are the lattice vectors), with sublattices A (Blue) and B (Red). Right: Shows the corresponding Brillouin zone. The Dirac cones are located at  $K$  and  $K'$ .

energy theory of graphene is a condensed-matter analog of (2+1)-dimensional QED. The basis vectors of a honeycomb lattice can be written as

$$\vec{a} = (1, 0)a, \quad \vec{b} = \left(-\frac{1}{2}, \frac{\sqrt{3}}{2}\right)a, \quad (2.3)$$

where  $a/\sqrt{3} = 1.42A$  is the carbon-carbon atom distance. With a judicious choice of lattice vectors graphene's hamiltonian in the nearest neighbor tight-binding approximation can be written as

$$\mathcal{H}_{TB}(\vec{k}) = \begin{pmatrix} 0 & -t\gamma(\vec{k}) \\ -t\gamma^*(\vec{k}) & 0 \end{pmatrix}, \quad (2.4)$$

where  $t(\sim 2.8\text{eV})$  is the nearest neighbor hopping energy (hopping between different sublattices A and B) and  $\gamma(\vec{k})$  is defined as

$$\gamma(\vec{k}) = 1 + e^{i\vec{k}\cdot\vec{a}} + e^{i\vec{k}\cdot(\vec{b}+\vec{a})} \quad (2.5)$$

The energy dispersion derived from this hamiltonian can be written as  $E(\vec{k}) = \pm t|\gamma(\vec{k})|$ . The reciprocal lattice vectors in the hexagonal BZ are given by

$$\vec{G}_1 = \frac{2\pi}{a}(1, \frac{1}{\sqrt{3}}), \quad \vec{G}_2 = \frac{4\pi}{\sqrt{3}a}(0, 1). \quad (2.6)$$

It is easy to see that  $\gamma(\vec{k})$  and hence the energy  $E(\vec{k})$  vanishes at two points  $K$  and  $K'$  at the corners of the Brillouin zone, these points are called Dirac points for reasons that will become clear towards the end of this section. The Dirac points are given by

$$\vec{K} = \frac{2\pi}{a}(\frac{1}{\sqrt{3}}, \frac{1}{\sqrt{3}}), \quad \vec{K}' = -\frac{2\pi}{a}(\frac{1}{\sqrt{3}}, \frac{1}{\sqrt{3}}). \quad (2.7)$$

Expanding  $\gamma(\vec{k})$  around the Dirac point  $K$  with  $\vec{p} = \vec{K} + \vec{q}$  gives:

$$\gamma(\vec{k}) = \vec{q} \cdot \frac{\partial\gamma}{\partial\vec{p}}|_{\vec{p}=\vec{K}} = \frac{\sqrt{3}}{2}ta(q_x + iq_y). \quad (2.8)$$

The effective hamiltonian around the  $K$  point can therefore be written as

$$\mathcal{H}(\vec{q}) = v_F\vec{\sigma} \cdot \vec{q}, \quad (2.9)$$

where  $\sigma_i$  are Pauli matrices,  $\vec{q}$  is momentum measured relative to the Dirac point  $K$  and  $v_F = (\sqrt{3}/2)ta \approx 1 \times 10^6\text{m/s}$  is graphene's material specific speed of light. A similar expression can be obtained around the other Dirac point

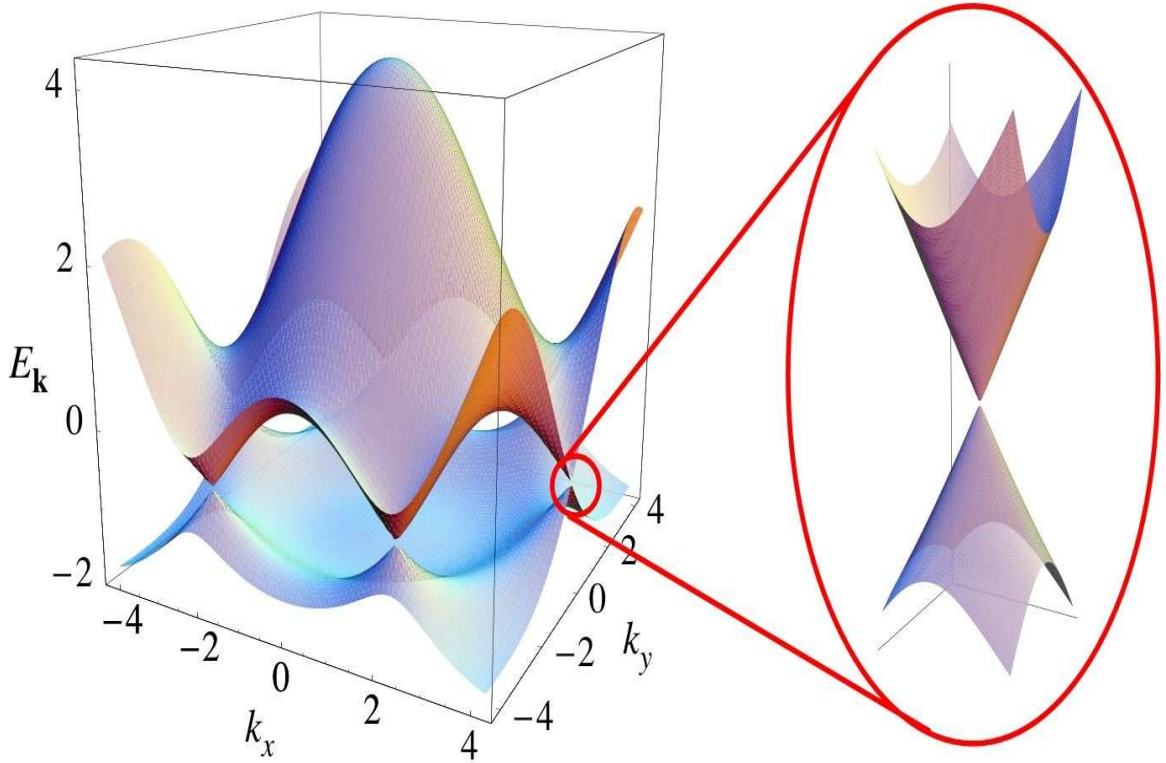


Figure 2.4: (Adapted from [10]) Left: Numerically calculated energy spectrum of graphene (in units of  $t$ ). Right: Magnified linear energy dispersion near the Dirac point.

$K'$ . The energy dispersion near the Dirac points  $K$  and  $K'$ ,  $\epsilon(\vec{q}) = \pm v_F |\vec{q}|$  is linear. It is now clear that the low energy effective theory for graphene can be described by massless Dirac Fermions with a material specific speed of light. Figure 2.4 shows a numerical calculation of graphene's spectrum, the linear dispersion around the Dirac points  $K$  and  $K'$  is apparent [10].

---

<sup>1</sup>With our definition of pseudospin components graphene's low-energy effective hamiltonian is just  $\mathcal{H}(\vec{q}) = \xi v_F \vec{\sigma} \cdot \vec{q}$  in valley  $K'$  ( $\xi = -1$ ).

When the Fermi energy lies at the Dirac points, this system is referred to as neutral graphene, raising the Fermi energy above(below) the Dirac point gives hole(electron) doped graphene. The most striking difference due to graphene's unusual linear band structure is that unlike the energy dispersion of a regular 2DEG  $\epsilon(\vec{q}) = q^2/2m$  graphene's Fermi velocity is not energy or momentum dependent. This has important consequences on the Fermi liquid properties as we see in the upcoming chapters.

For  $J = 1$  chiral systems the eigenstates around valley  $K$  can be easily written from 2.2:

$$|\pm, \vec{q}\rangle_K = \frac{1}{\sqrt{2}} \begin{pmatrix} 1 \\ \pm e^{i\phi_{\vec{q}}} \end{pmatrix} \quad (2.10)$$

where  $\pm$  corresponds to the eigenenergies  $\epsilon_q = \pm v_F q$  which in tight binding language correspond to the  $\pi$  and  $\pi^*$  band respectively. The eigenstates around  $K$  and  $K'$  are related by time reversal symmetry leading to opposite chirality in the two valleys. The eigenstates also exhibit a Berry's phase of  $\pi$  (i.e. the wavefunction changes sign if the phase  $\phi$  is rotated by  $2\pi$ ), with a similar property characteristic of other chiral systems.

For  $J = 1$  chiral systems, chirality can be defined in another way commonly referred to as helicity. Helicity is defined as the projection of the pseudo(spin) operator in the direction of momentum [24]:

$$\hat{h} = \frac{\vec{\sigma} \cdot \vec{q}}{|\vec{q}|}, \quad (2.11)$$

from the definition of the helicity operator it is easy to see that it commutes with the hamiltonian  $\mathcal{H}(\vec{q}) = v_F \vec{\sigma} \cdot \vec{q}$ , and that  $|\pm, \vec{q}\rangle_K$  and  $|\pm, \vec{q}\rangle_{K'}$  are also

eigenstates of the helicity operator. Electrons(holes) have positive(negative) chirality or helicity, stating that only states close to the Dirac point have a well-defined helicity. It is only good a quantum number as long as hamiltonian 2.9 is valid, and therefore holds only as an asymptotic property, well defined close to the Dirac points.

### 2.1.2 Cyclotron Mass and Density of States

An immediate consequence of this massless Dirac-like dispersion is a cyclotron mass that depends on the electronic density as its square root. The cyclotron mass within the semiclassical approximation can be expressed as

$$m^* = \frac{1}{2\pi} \left[ \frac{\partial A(\epsilon)}{\partial \epsilon} \right]_{\epsilon=\epsilon_F}, \quad (2.12)$$

with  $A(\epsilon)$  the area enclosed by an orbit in momentum space given by:

$$A(\epsilon) = \pi q(\epsilon) = \pi \frac{\epsilon^2}{v_F^2}, \quad (2.13)$$

giving us

$$m^* = \frac{k_F}{v_F} = \frac{\sqrt{\pi}}{v_F} \sqrt{n}, \quad (2.14)$$

where the electronic density  $n$  is related to the Fermi momentum  $k_F$  via  $n = k_F^2/\pi$  (here we have already accounted for the valley degeneracy). Fitting the above expression to the experimental data provides an estimate for the Fermi velocity and the hopping parameter ( $v_F \sim 10^6 m/s$  and  $t \sim 2.8eV$  respectively). This experimental observation of the  $\sqrt{n}$  dependence provides evidence for the existence of massless Dirac quasiparticles in graphene [3, 4].

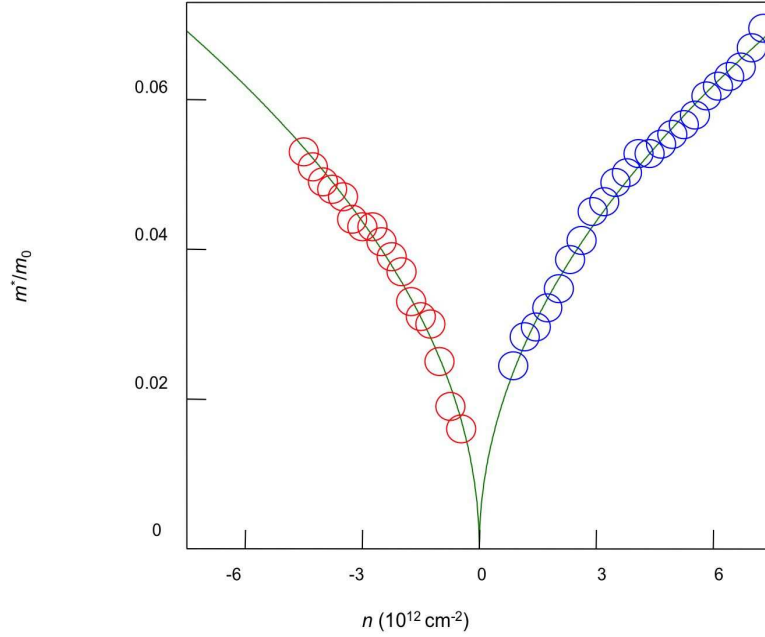


Figure 2.5: (Adapted from [10]) Cyclotron mass of quasiparticles in graphene as a function of their concentration( $n$ ), positive and negative  $n$  correspond to electron and holes respectively. Experimental data extracted from SdH oscillations.

Close to the Dirac point the density of states per unit area of a unit cell for spin polarized Dirac fermions per valley is given by the expression

$$D(\epsilon) = \frac{\epsilon}{2\pi v_F^2} \quad (2.15)$$

from 2.15 we can see that the density of states in graphene vanishes close to the Dirac point. From this density of states we can see that graphene exhibits a semimetallic behavior.

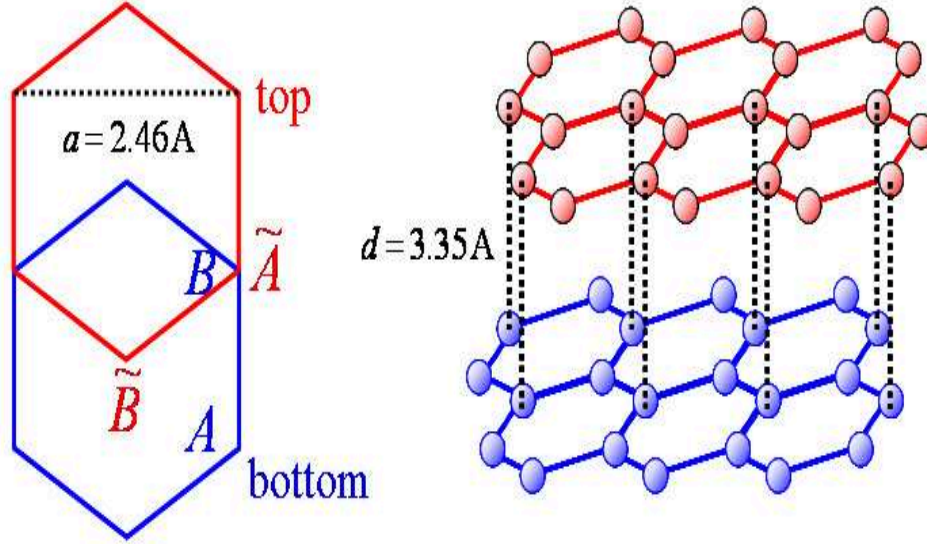


Figure 2.6: Lattice structure of bilayer graphene with a honeycomb lattice constant  $a = 2.46\text{\AA}$  and interlayer separation  $d = 3.35\text{\AA}$ .

## 2.2 Bilayer Graphene

In this section we describe another intriguing chiral system closely related to graphene. Soon after the experimental discovery of graphene it was recognized that a graphite bilayer's low energy effective hamiltonian falls within the family of Chiral hamiltonians discussed in this chapter, with chirality index  $J = 2$  [13]. This has important consequences for Quantum Hall Effect as we see later in this chapter and towards the end of the dissertation. Starting from the continuum low-energy effective theory of graphene, in this section we show that bilayer graphene is a  $J = 2$  chiral system.

A graphite bilayer has two graphene layers with one stacked on top of

the other in a particular arrangement as shown in Fig 2.6. commonly referred to as Bernal stacking. We refer to the two sublattice degree of freedom in bilayer graphene as  $A(\tilde{A})$  and  $B(\tilde{B})$  in the bottom(top) layers respectively. As we have already seen single layer graphene's honeycomb lattice supports a degeneracy point at the two inequivalent corners of a hexagonal Brillouin Zone  $K$  and  $K'$  which coincide with the Fermi point in a neutral structure and determine the centers of the two valleys of a gapless spectrum. The direct interlayer hopping  $\tilde{A}-B$   $\gamma_{\tilde{A}-B} \equiv \gamma_1 \approx 0.4eV$  forms a dimer state from the  $\tilde{A}-B$  orbitals thus leading to the formation of high energy bands. There also exists weak intralayer hopping from  $A$  to  $\tilde{B}$  via the dimer state  $\gamma_{A-\tilde{B}} \equiv \gamma_3 \ll \gamma_1$  leading to trigonal warping of the band structure [13]. We neglect this and other remote weak interlayer hopping processes for the moment.

Starting from the low-energy effective hamiltonian for graphene we can write the hamiltonian for a Bernal-stacked bilayer graphene near valley  $K$ :

$$\mathcal{H} = \begin{pmatrix} 0 & v\pi^\dagger & 0 & 0 \\ v\pi & 0 & \gamma_1 & 0 \\ 0 & \gamma_1 & 0 & v\pi^\dagger \\ 0 & 0 & v\pi & 0 \end{pmatrix}, \quad (2.16)$$

where  $\pi = q_x + iq_y$  and  $v$  in graphene's Fermi velocity. The hamiltonian operates on a four-component wavefunction  $\Phi^\dagger = (\psi^\dagger(A), \psi^\dagger(B), \psi^\dagger(\tilde{A}), \psi^\dagger(\tilde{B}))$  where  $\psi$  denotes the envelop function on the corresponding atomic sites. The energy spectrum  $\epsilon_\alpha^\pm(\vec{q})$  can be parameterized by an integer  $\alpha = 1, 2$ :

$$\epsilon_\alpha^\pm = \gamma_1 \cos\left(\frac{\alpha\pi}{3}\right) \pm \sqrt{v^2|\vec{q}|^2 + \gamma_1^2 \cos^2\left(\frac{\alpha\pi}{3}\right)}. \quad (2.17)$$

Identifying  $m_\alpha v^2 = |\gamma_1 \cos(\frac{\alpha\pi}{3})|$  the above energy resembles the relativistic energy spectrum for a particle with momentum  $\vec{q}$  and mass  $m$ . The low-energy spectrum given by:

$$\epsilon(\vec{q}) = \begin{cases} \frac{q^2}{2m_2} & \alpha = 1 \\ -\frac{q^2}{2m} & \alpha = 2, \end{cases} \quad (2.18)$$

resembles the quadratic dispersion of a massive particle with mass  $m = \gamma_1/2v^2 \approx 0.054m_e$ , not too different from the effective mass in GaAs ( $m^* = 0.064m_e$ ). The range of validity of 2.18 can be determined from 2.17 giving the condition  $|\epsilon| \ll \gamma_1/4$  which can be upto several  $meV$ 's. This low-energy chiral behaviour has already been observed in quantum Hall experiments on bilayer graphene [5]. We leave this discussion for the next section.

The direct interlayer vertical hopping between  $\tilde{A}$  and  $B$  spans the high-energy subspace leaving the low-energy subspace to be spanned by  $A$  and  $\tilde{B}$ . Using degenerate state perturbation theory we can derive the effective hamiltonian acting on the low-energy subspace:

$$\mathcal{H}_{eff} = H_{AB} - H_{AB} \frac{1}{H_{B\tilde{A}}} H_{\tilde{A},\tilde{B}}, \quad (2.19)$$

where  $H_{AB} = 0$  is the hamiltonian projected onto the low-energy states,  $H_{B\tilde{A}}$  is the hamiltonian projected onto the high-energy states,  $H_{AB}$  and  $H_{\tilde{A},\tilde{B}}$  account for the intralayer ( $\gamma_1$ ) hopping process. It can easily be shown that

$$\mathcal{H}_{eff} = -\frac{v^2}{\gamma_1} \begin{pmatrix} 0 & (\pi^\dagger)^2 \\ (\pi)^2 & 0 \end{pmatrix}, \quad (2.20)$$

Identifying  $m = \gamma_1/2v^2$  gives the same quadratic dispersion as before. The quasiparticles describing bilayer graphene exhibit a Berry's phase of  $2\pi$  along

with a parabolic dispersion quite distinct from graphene and normal 2DEGs. This effective hamiltonian also belongs to the class of Chiral hamiltonians with chirality index  $J = 2$ .

Including the remote interlayer hopping  $\gamma_3$  and allowing the possibility of a onsite energy difference between the layers  $\Delta_V$  give additional contributions to the effective hamiltonian [13]  $\mathcal{H}_{eff} \rightarrow \mathcal{H}_{eff} + h_w + h_\Delta$  where:

$$h_w + h_\Delta = v_3 \begin{pmatrix} 0 & \pi \\ \pi^\dagger & 0 \end{pmatrix} + \Delta_V \begin{pmatrix} \frac{1}{2} - \frac{1}{2m\gamma_1}\pi^\dagger\pi & 0 \\ 0 & -\frac{1}{2} + \frac{1}{2m\gamma_1}\pi\pi^\dagger \end{pmatrix} \quad (2.21)$$

The external potential difference  $\Delta_V$  opens a gap in the spectrum modifying the parabolic dispersion to a mexican hat type potential [25] with the gap size increasing with increasing electric potential. The ability to control this gap using gate controlled external potential makes bilayer graphene more interesting for technological applications [26, 27].

The role of electron-electron interactions in bilayer graphene is quite interesting. The Fermi liquid properties of bilayer graphene<sup>2</sup> are still not understood as no sophisticated treatment of electron-electron interactions in bilayer graphene exists in the literature. There are number of interesting properties that have been highlighted by other authors that are of particular interest due to the presence of chiral bands: for examples it has been predicted that bilayer graphene exhibits spontaneous pseudospin polarization [28] (i.e. charge is spontaneously transferred to one layer). It has also been predicted that neutral bilayer graphene is unstable towards Wigner crystallization [29] and also

---

<sup>2</sup>An interesting question yet unanswered is whether bilayer graphene is a Fermi liquid at the neutrality point.

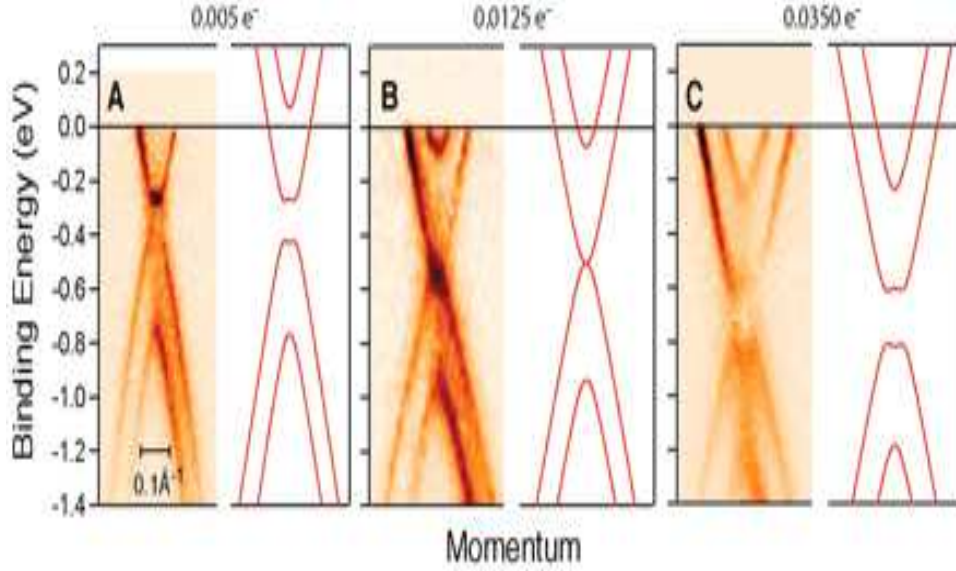


Figure 2.7: (Adapted from [26]) This figure shows the evolution of gap closing and reopening by changing the doping level by potassium adsorption. Experimental and theoretical bands (solid lines) (A) for an as-prepared graphene bilayer and (B and C) with progressive adsorption of potassium are shown. The number of doping electrons per unit cell, estimated from the relative size of the Fermi surface, is indicated at the top of each panel

ferromagnetism [30]. Towards the end of this thesis we focus on yet another interesting question of electron-electron interactions in bilayer graphene in the Quantum Hall regime.

### 2.3 Chiral Fermions in a magnetic field

In the presence of a uniform magnetic field  $\vec{B} = B\hat{z}$  applied in a direction perpendicular to plane of the C2DEG, Hamiltonian 2.2 is modified by  $\vec{p} \rightarrow \vec{\pi} = \vec{p} + (e/c)\vec{A}$  where  $\vec{A}$  is the vector potential with  $\vec{B} = \nabla \times \vec{A}$ .

Defining the usual raising and lowering Landau level operator  $a^\dagger$  and  $a$  with  $a^\dagger = (l_B/\sqrt{2}\hbar)\pi$ , where  $l_B = (\hbar c/eB)^{1/2} = 25.6/\sqrt{B[\text{Tesla}]}\text{nm}$  is the magnetic length, the hamiltonian 2.2 in  $\xi = +1$  becomes :

$$\mathcal{H}_J \propto \left(\frac{\sqrt{2}\hbar}{l_B}\right)^J \begin{pmatrix} 0 & a^J \\ (a^\dagger)^J & 0 \end{pmatrix}. \quad (2.22)$$

One immediate consequence is the appearance of zero-energy eigenstates which can be identified by  $a^J \phi_n = 0$  for 2D orbitals with Landau level index  $n = 0, \dots, J$  (here  $\phi_n$  are the well known Landau level wavefunctions). This yields a  $4J$ -fold degenerate (including valley and spin) zero state, which leads to the presence of anomalous Half-integer Quantum hall effect for  $J$  odd in these chiral systems. The  $4J$ -fold degeneracy is already evident in quantum hall measurements performed on monolayer graphene ( $J = 1$ )[3, 4] and bilayer graphene ( $J = 2$ ) [5] chiral systems, we discuss this in the next section. The zero-energy eigenstates are localized on the  $\uparrow$  ( $\downarrow$ ) pseudospin in the  $K$  ( $K'$ ) valley, which for graphene corresponds to localization on sublattice A(B) and top(bottom) layer in the case of bilayer graphene.

The energy of the other Landau levels is given by:

$$\epsilon_{n,J} \propto \pm \left(\frac{\sqrt{2}\hbar}{l_B}\right)^J \sqrt{n(n-1)\dots(n-J+1)}, \quad (2.23)$$

with chiral eigenstates in a magnetic field associated with the  $s = \pm$  energies:

$$\frac{1}{\sqrt{2}} \begin{pmatrix} s\phi_{n-J+1} \\ \phi_n \end{pmatrix}. \quad (2.24)$$

The energy spectrum of a chiral system in a magnetic field is remarkably different from that of a normal 2DEG, where the Landau levels are equally spaced with the energy between adjacent levels equal to  $\hbar\omega$  ( $\omega = eB/mc$ ) and there are no zero energy eigenstates. In a  $J$  chiral system the energy scales as  $B^{J/2}$  also very different from the standard 2DEG for  $J \neq 2$ .

The existence of the zero-energy  $4J$ -fold degenerate state for sufficiently clean chiral systems is very interesting from the point of view of electron-electron interactions [31–33]. Since the kinetic energy is quenched in a Landau level electron-electron interactions play a dominant role in determining the ground state of the system, leading to broken symmetry states at integer filling factors and also to the possibility of novel exotic strongly correlated states at fractional filling factors. Broken symmetry states were predicted to exist in monolayer graphene [31] have already been seen in experimental studies on monolayer graphene. In the last chapter we investigate yet another and more interesting set of broken symmetry states that we believe should appear in bilayer graphene samples with high mobility at sufficiently strong magnetic fields. In the next section we specifically discuss the presence of anomalous hall effect in monolayer and bilayer graphene.

### 2.3.1 Quantum Hall Effect of Chiral Fermions

Quantum Hall Effect(QHE) is one of the most remarkable phenomenon in condensed matter physics [34–37]. Its discovery in 1980s was one of the watershed moments ranking it among the most important discoveries within

the last three decades. The basic experimental fact characterizing QHE is the vanishing diagonal conductivity  $\sigma_{xx} \rightarrow 0$  and the quantization of the off-diagonal conductivity  $\sigma_{xy} = \nu e^2/h$  where  $\nu$  is an integer for Integer QHE or a fraction for Fractional QHE.

IQHE in normal 2DEGs is different from that of chiral systems, the presence  $4J$ -fold degenerate zero energy state leads to an unusual Half-Integer Quantum Hall Effect for  $J$  odd with the off-diagonal conductivity:

$$\sigma_{xy} = \pm 4 \frac{e^2}{h} \left( n + \frac{J}{2} \right), \quad n = 0, 1, 2, \dots \quad (2.25)$$

To understand this unusual quantization condition let us first review IQHE in normal 2DEGs. The quantization condition for a 2DEG can be understood from the dispersion. The dispersion of a 2DEG is given by  $\epsilon_n = (n + 1/2)\hbar\omega_c$  with the LL equally spaced by the cyclotron energy  $\hbar\omega_c$ . In the presence of disorder LLs get broadened with the current carrying states localized when the chemical potential lies between the LLs. So when the Fermi energy lies in a gap between LLs, electrons can not move to new states and there is no scattering. Thus the transport is dissipationless and the resistance falls to zero. However there is a delocalized state at the position of each LL with the number of current carrying states at each LL given by  $eB/h$ . When  $n$  LLs are filled below the chemical potential there are  $neB/h$  current carrying states giving  $\sigma_{xy} = ne^2/h$ . As the chemical potential crosses a LL there is an extra contribution to the current from the delocalized state at the center of the LL and hence the off-diagonal conductivity jumps by an integer.

The unusual QHE unique to Chiral Fermions and can be understood

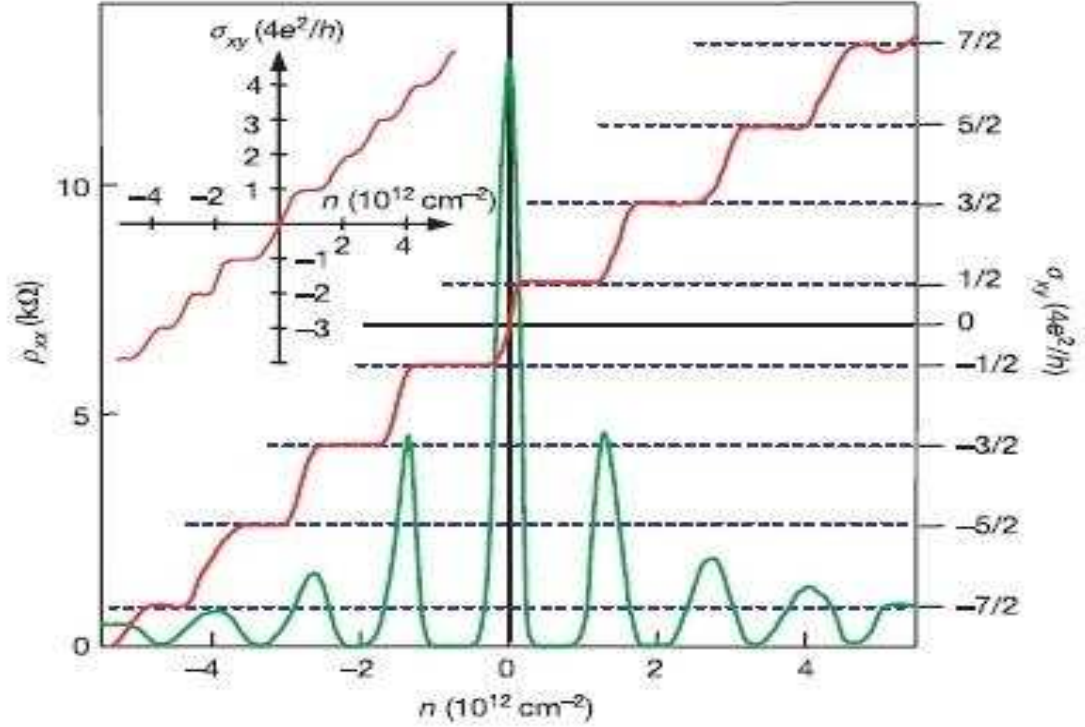


Figure 2.8: (Adapted from [3]) Hall conductivity  $\sigma_{xy}$  and longitudinal  $\rho_{xx}$  of graphene as a function of the concentration at  $B = 14T$ . The inset show bilayer graphene's hall conductivity as a function of concentration.

from the unusual spectrum of Landau levels and the presence of zero-energy eigenstates. We can identify the spectrum for  $J$  Chiral Fermions as electron-like ( $n \geq J$ ) and hole-like ( $n \leq -J$ ) along with the  $4J$ -fold degenerate zero-energy state where electrons and holes are degenerate. Due to the presence valley and spin each LL has a degeneracy 4. With the given spectrum of LLs for Chiral Fermions the Hall conductance  $\sigma_{xy}$  exhibits QH plateau when ( $|n| \geq J$ ) are fully occupied and jumps by an amount  $4e^2/h$  when the chem-

ical potential crosses a ( $|n| \geq J$ ) LL. The unusual half-integer is due to the presence of a zero-energy state, the first plateau for the electrons ( $n \leq J$ ) and holes ( $n \leq -J$ ) are situated at  $\pm 2Je^2/h$ . As the chemical potential crosses the next electron(hole) LL the conductivity increases(decreases) by an amount of  $4e^2/h$  which gives us the quantization condition 2.25.

This unusual Hall Effect has already been measured in Hall conductivity experiments in single layer and bilayer graphene. In fact broken symmetry states have also been measured in graphene, giving rise plateaus at all intermediate integer fillings. The appearance of QH plateaus at these intermediate integers is due to the effect of electron-electron interactions. At present there is no experimental verification of broken symmetry states in bilayer graphene. Furthermore the cyclotron energy in 2DEG is measured to be about 10 K at a magnetic field strength of 10 T, where as in graphene at the same field strength cyclotron gap could in principle be as large as 1300 K. This opens the possibility of observing integer quantum hall effect at room temperature, and recent observation of room temperature Hall effect in graphene has already been reported [38].

## Chapter 3

### Chirality and Correlations in Graphene

The study of electron-electron interactions is an important and fundamental pursuit of condensed matter physics [40]. The study of the effect of interactions is quite complex as it involves understanding the behavior of a microscopic number of variables, and hence physicists have to rely on a number of approximations to study interacting systems.

The simplest approach generally used as a starting point towards a many-body problem is the Hartree-Fock (HF) approximation. The basic idea behind the HF approximation is an attempt to approximate the ground-state of the interacting system by that of an effective hamiltonian which is quadratic in the electron creation and destruction operator thereby resembling the form of a single-particle hamiltonian that can be easily diagonalized. The most common version of this procedure is to approximate the true ground-state by a N-electron single Slater determinant wavefunction in an attempt to figure out the best independent-electron approximation to the interacting system. The HF approximation is quite unreliable as it has a tendency to over estimate the presence of broken symmetry states. This approximation does not include the quantum fluctuations which in some cases tend to restore the full symmetry, therefore HF approximation is only a guide towards broken symmetry states



Figure 3.1: Random-phase-approximation in terms of Feynman diagrams.

and HF results should not be accepted without validation of more accurate studies. The approximate nature of the HF ground-state leads to the concept of correlations. Correlation effects are, by definition, effects that stem from the fact that the true interacting ground state wavefunction is not a single Slater determinant.

The simplest approximation involving correlations is the Random Phase Approximation (RPA). This is generally the most popular and significant attempt to go beyond the HF approximation. RPA accounts for quantum fluctuations of the interaction by including virtual particle-hole pairs. It can be best understood in terms of Feynman diagrams where a subgroup of all possible diagrams can be formally summed up to infinite order. Fig 3 shows RPA summation in terms of Feynman diagrams, the double wavy line represents the renormalized interaction, single wavy line represents the bare interaction, and the bubble are virtual particle-hole pairs. The diagrams can be formally written as a geometric series<sup>1</sup>. The physics captured in this sum-

---

<sup>1</sup>Strictly speaking  $\sum x^n = \frac{1}{1-x}$  requires  $|x| < 1$ , however this approximation yields qualitatively correct results when compared to experiments even outside this range.

mation in the screening of Coulomb potential at large distances. In electron gas RPA is generally a good approximation in the high density limit thereby becoming exact as  $r_s \sim 1/\sqrt{n}$  ( $n$  is the density) becomes small. In this chapter we employ RPA to study thermodynamic properties of doped graphene sheets. However, before we study doped graphene sheets let us understand the effect of electron-electron interactions in neutral or undoped graphene sheets.

Since graphene is truly a two-dimensional system lets us compare it to the more standard 2DEG which has been studied extensively since the development of heterostructures and the discovery of quantum hall effect. At the simplest level metallic systems have two main kinds of excitations: Particle-hole pairs and collective modes (such as plasmons). Particle-hole pairs are incoherent excitations of the Fermi sea and a direct result of Pauli's exclusion principle. An electron inside the Fermi sea at momentum  $\vec{k}$  can only be excited outside the Fermi Sea to a new state with momentum  $\vec{k} + \vec{q}$  leaving behind a hole. The energy associated to such an excitation is simply:  $\omega = \epsilon_{\vec{k}+\vec{q}} - \epsilon_{\vec{k}}$ , and for states close to the Fermi sea scales like  $\omega_q \sim v_F q$ . In 2DEGs the electron hole continuum is made out of intra-band transitions only, and exists even at zero energy since it is always possible to produce electron-hole pairs with arbitrary low-energy close to the Fermi surface. 2DEGs also contain collective excitations such as plasmons with dispersion:  $\omega_{plasmon} \propto \sqrt{q}$  that exist outside the particle-hole continuum at sufficiently long wavelengths.

In undoped graphene where Fermi energy lies at the Dirac point, the Fermi surface shrinks to a point and hence intra-band excitations disappear

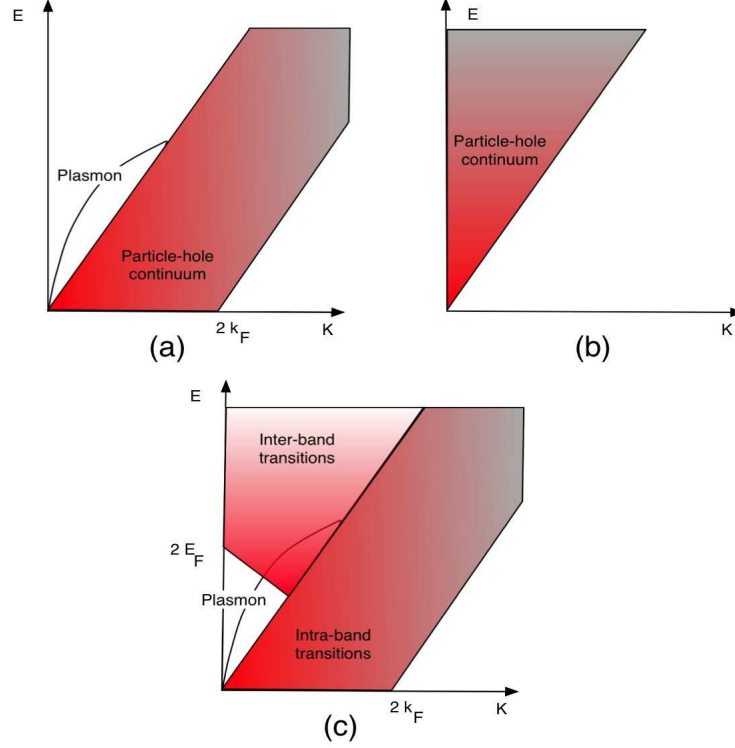


Figure 3.2: (Adapted from [10]) Particle-hole continuum and collective modes of: (a) 2DEG ; (b) neutral graphene; (c) doped graphene

and only inter-band transitions between the lower and upper Dirac cones are allowed. In neutral graphene there are no particle-hole excitations at low-energy and each particle-hole pair costs energy, the particle-hole continuum occupies the upper triangle as shown in Fig 3.2. Plasmons are also suppressed and no coherent collective modes can exist. This can be seen from neutral graphene's Lindhard function calculated in Appendix A:

$$\frac{q^2}{16\sqrt{v^2q^2 - \Omega^2}}, \quad (3.1)$$

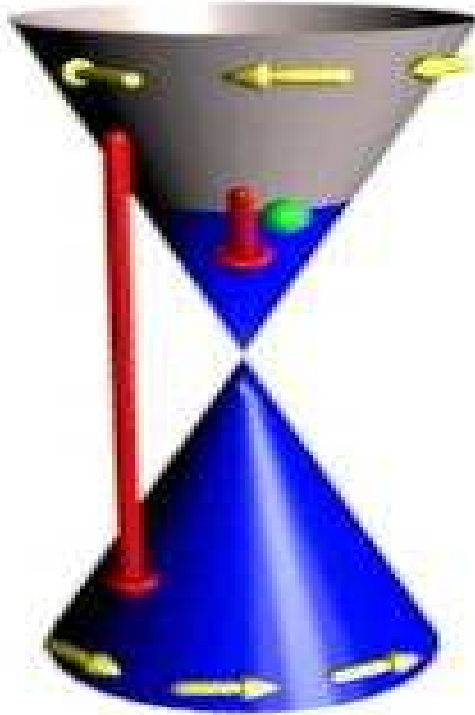


Figure 3.3: Dirac cone for n-doped graphene, the yellow arrows represents the chirality of the bands  $s = +(-)$  for clockwise and anti-clockwise, and the red arrows represent particle-hole transitions.

which is imaginary for  $\Omega > v_F q$  indicating a damping of the particle-hole pairs. The static polarization function ( $\Omega = 0$ ) vanishes linearly with  $q$ , also indicating a lack of screening in neutral graphene.

In doped graphene sheets where Fermi energy is moved away from the Dirac point, the situation becomes a little different, intra-band excitations are restored and inter-band excitations have to account for Pauli blocking effect of the filled Fermi sea in the upper cone as shown in the Fig 3.3. The plasmon

modes are now allowed as can be seen from Fig 3.2, however the situation is still very different from 2DEGs as intra-band transition along with chirality play an important role on the thermodynamic properties of doped graphene sheets as we show in this chapter. Due the presence of intra-band transitions and Pauli blocking effect of the filled Fermi sea in the upper cone these properties have a dependence on the doping: as we shift the Fermi energy inter-band transitions begin to dominate more and more and the system starts to resemble a standard 2DEG.

In particular we show that quasiparticle chirality in weakly doped graphene layers also leads to a peculiar suppression of the charge and spin susceptibilities. We predict that both quantities are suppressed by approximately 15% in current samples and that the suppression will be larger if uniform samples with much lower densities can be realized. At a qualitative level, these effects arise from an interaction energy preference for MDF states with larger chiral polarization. Our conclusions are based on an evaluation of the exchange and RPA correlation energies of uniform spin-polarized MDF systems with Coulomb interactions. We first describe this calculation, paying careful attention to the MDF model's ultraviolet cutoff, present its predictions for the charge and spin susceptibilities of graphene, and finally discuss the origin of this unusual physics.

### 3.1 RPA Theory of Graphene

We study the following MDF model Hamiltonian,

$$\hat{\mathcal{H}} = v \sum_{\mathbf{k}} \hat{\psi}_{\mathbf{k}}^{\dagger} [\sigma^3 \otimes \mathbb{I} \otimes (\vec{\sigma} \cdot \vec{k})] \hat{\psi}_{\mathbf{k}} + \frac{1}{2S} \sum_{\mathbf{q} \neq 0} v_q \hat{n}_{\mathbf{q}} \hat{n}_{-\mathbf{q}}, \quad (3.2)$$

where  $\sigma^3$  acts on the two-degenerate (K and K') valleys,  $\vec{k}$  is two-dimensional vector measured from the K and K' points,  $\sigma^1$  and  $\sigma^2$  are Pauli matrices that act on graphene's pseudospin degrees of freedom,  $\mathbb{I}$  is the  $2 \times 2$  identity matrix that acts on the physical spin,  $S$  is the sample area,  $\hat{n}_{\mathbf{q}} = \sum_{\mathbf{k}} \hat{\psi}_{\mathbf{k}-\mathbf{q}}^{\dagger} \hat{\psi}_{\mathbf{k}}$  is the total density operator, and  $v_q = 2\pi e^2 / (\epsilon q)$  is the 2D Fourier transform of the Coulomb interaction potential  $e^2 / (\epsilon r)$ . In Eq. (3.2) the field operator  $\hat{\psi}_{\mathbf{k}}$  is a eight-component spinor that encompasses valley, spin and pseudospin degrees of freedom <sup>2</sup>. In this chapter chirality ( $s, s' = \pm$ ) is given by the expectation value of  $\vec{\sigma} \cdot \vec{k} / |\mathbf{k}|$ , which is the same as the definition of chirality stated in chapter 1. The model (3.2) requires an ultraviolet cutoff, as we discuss below. To evaluate the interaction energy we follow a familiar strategy [40] by combining a coupling constant integration expression for the interaction energy valid for uniform continuum models,

$$E_{\text{int}} = \frac{N}{2} \int_0^1 d\lambda \int \frac{d^2 \mathbf{q}}{(2\pi)^2} v_q [S^{(\lambda)}(q) - 1], \quad (3.3)$$

with a fluctuation-dissipation-theorem (FDT) expression [40] for the static structure factor,

$$S^{(\lambda)}(q) = -\frac{1}{\pi n} \int_0^{+\infty} d\Omega \chi_{\rho\rho}^{(\lambda)}(\mathbf{q}, i\Omega), \quad (3.4)$$

---

<sup>2</sup>The MDF model can only describe low-energy processes, therefore we neglect inter-valley scatters

where  $n$  is the total electron density. This form of the FDT theorem takes advantage of the smooth behavior of the density-density response function along the imaginary axis  $\chi_{\rho\rho}^{(\lambda)}(\mathbf{q}, i\Omega)$ . The RPA approximation for the interaction energy then follows from the RPA approximation for  $\chi$ :

$$\chi_{\rho\rho}^{(\lambda)}(\mathbf{q}, i\Omega) = \frac{\chi^{(0)}(\mathbf{q}, i\Omega)}{1 - \lambda v_q \chi^{(0)}(\mathbf{q}, i\Omega)} \quad (3.5)$$

where  $\chi^{(0)}(\mathbf{q}, i\Omega)$  is the non-interacting density-density response-function. We [41] have derived the following compact expression for the  $\chi^{(0)}$  contribution for an individual MDF model channel, the details of the calculation are presented in Appendix A.

$$\begin{aligned} \chi^{\text{MDF}}(\mathbf{q}, i\Omega) &= -\frac{q^2}{16\sqrt{\Omega^2 + v^2q^2}} - \frac{\varepsilon_{\text{F}}^{\text{c}}}{2\pi v^2} \\ &+ \frac{q^2}{8\pi\sqrt{\Omega^2 + v^2q^2}} \Re \left[ \sin^{-1} \left( \frac{2\varepsilon_{\text{F}}^{\text{c}} + i\Omega}{vq} \right) + \left( \frac{2\varepsilon_{\text{F}}^{\text{c}} + i\Omega}{vq} \right) \sqrt{1 - \left( \frac{2\varepsilon_{\text{F}}^{\text{c}} + i\Omega}{vq} \right)^2} \right]. \end{aligned} \quad (3.6)$$

In Eq. (3.6)  $\varepsilon_{\text{F}}^{\text{c}} = vk_{\text{F}}^{\text{c}}$  where  $k_{\text{F}}^{\text{c}}$  is the channel Fermi momentum.  $\chi^{(0)}$  in Eq. (4.6) is constructed by summing the channel response function ( $\chi^{\text{MDF}}$ ) over valley and spin with appropriate  $\varepsilon_{\text{F}}^{\text{c}}$  values. For a spin- and valley-unpolarized system  $\chi^{(0)} = g\chi^{\text{MDF}}$  [with  $k_{\text{F}}^{\text{c}} \rightarrow k_{\text{F}} = (4\pi n/g)^{1/2}$ ] where  $g = g_{\text{s}}g_{\text{v}} = 4$  accounts for spin and valley degeneracy.

The energy constructed by combining Eqs. (3.3)-(3.6) is clearly divergent since  $\chi^{(0)}$  increases with  $q$  at large  $q$  and falls only like  $\Omega^{-1}$  at large  $\Omega^3$ . The divergence is expected since the energy calculated in this way includes

---

<sup>3</sup>These asymptotic expressions are calculated in Appendix A

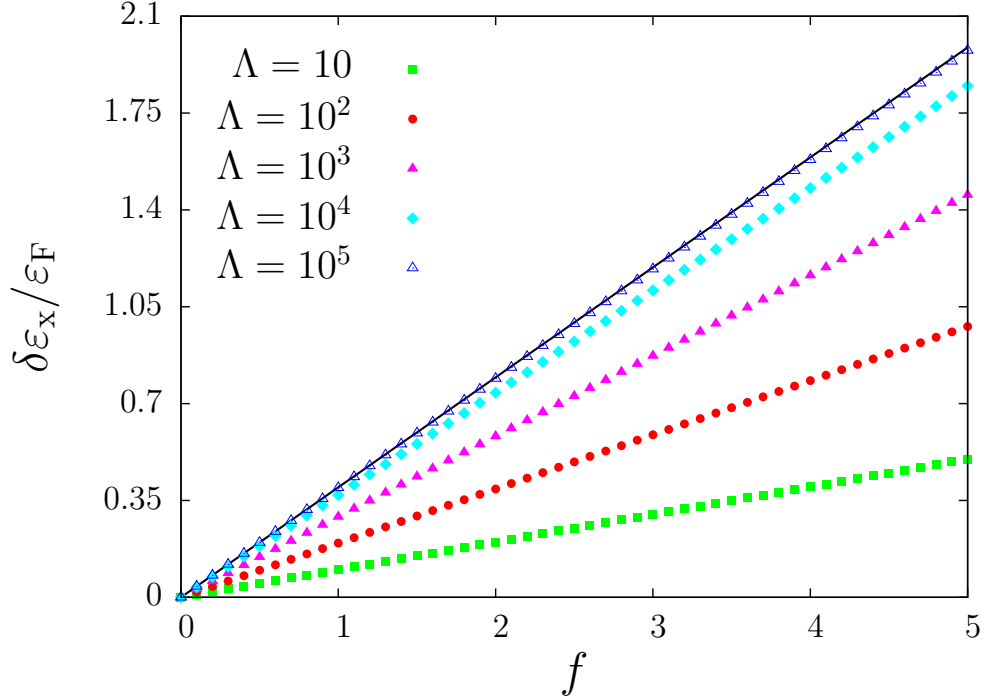


Figure 3.4: (Color online) Cut-off dependence of the regularized exchange energy  $\delta\epsilon_x$  in units of the Fermi energy  $\epsilon_F$ .

the interaction energy of the model's infinite sea of negative energy particles. The MDF model can be expected to describe only changes in energy with density and spin-density at small  $\epsilon_F^c$  values. For definiteness we choose the total energy of undoped graphene ( $\epsilon_F^c = 0$  in all channels) as our zero of energy. For pedagogical and numerical reasons it is also helpful to separate the contribution that is first order in  $e^2$ , the exchange energy, from the higher order contributions conventionally referred to in electron gas theory as the correlation energy. Using Eqs. (3.3)-(3.6) we find that for unpolarized doped

graphene the excess exchange energy per excess electron is

$$\begin{aligned}\delta\varepsilon_x &= -\frac{1}{2\pi n} \int \frac{d^2\mathbf{q}}{(2\pi)^2} v_q \int_0^{+\infty} d\Omega \left[ \chi^{(0)}(\mathbf{q}, i\Omega) - \chi^{(0)}(\mathbf{q}, i\Omega)|_{\varepsilon_F=0} \right] \quad (3.7) \\ &\equiv -\frac{1}{2\pi n} \int \frac{d^2\mathbf{q}}{(2\pi)^2} v_q \int_0^{+\infty} d\Omega \delta\chi^{(0)}(\mathbf{q}, i\Omega),\end{aligned}$$

and that the corresponding correlation energy is

$$\delta\varepsilon_c^{\text{RPA}} = \frac{1}{2\pi n} \int \frac{d^2\mathbf{q}}{(2\pi)^2} \int_0^{+\infty} d\Omega \left\{ v_q \delta\chi^{(0)}(\mathbf{q}, i\Omega) + \ln \left[ \frac{1 - v_q \chi^{(0)}(\mathbf{q}, i\Omega)}{1 - v_q \chi^{(0)}(\mathbf{q}, i\Omega)|_{\varepsilon_F=0}} \right] \right\}. \quad (3.8)$$

With this regularization the  $\Omega$  integrals are finite and the  $q$  integrals have logarithmic ultraviolet divergences. The remaining divergences are physical and follow from the interaction between electrons near the Fermi energy and electrons very far from the Fermi energy as we discuss at length later. The best we can do in using the MDF model to make predictions relevant to graphene sheets is to introduce an ultraviolet cutoff for the wavevector integrals,  $k_c$ .  $k_c$  should be assigned a value corresponding to the wavevector range over which the MDF model describes graphene. Based on this criterion [42] we estimate that  $k_c \sim 1/a$  where  $a \sim 0.246$  nm is graphene's lattice constant. The MDF is useful when  $k_c$  is much larger than  $k_F$  in all channels.

With this regularization the properties of graphene's MDF model depend on the dimensionless coupling constant

$$f \equiv g \frac{e^2}{\epsilon v \hbar} = \frac{g}{\epsilon} \frac{c}{v} \alpha, \quad (3.9)$$

and on  $\Lambda = k_c/k_F$ . In Eq. (4.11),  $c \sim 300v$  is the speed of light,  $\alpha \approx 1/137$  is the fine structure constant, and  $\epsilon$  depends on the dielectric environment of the

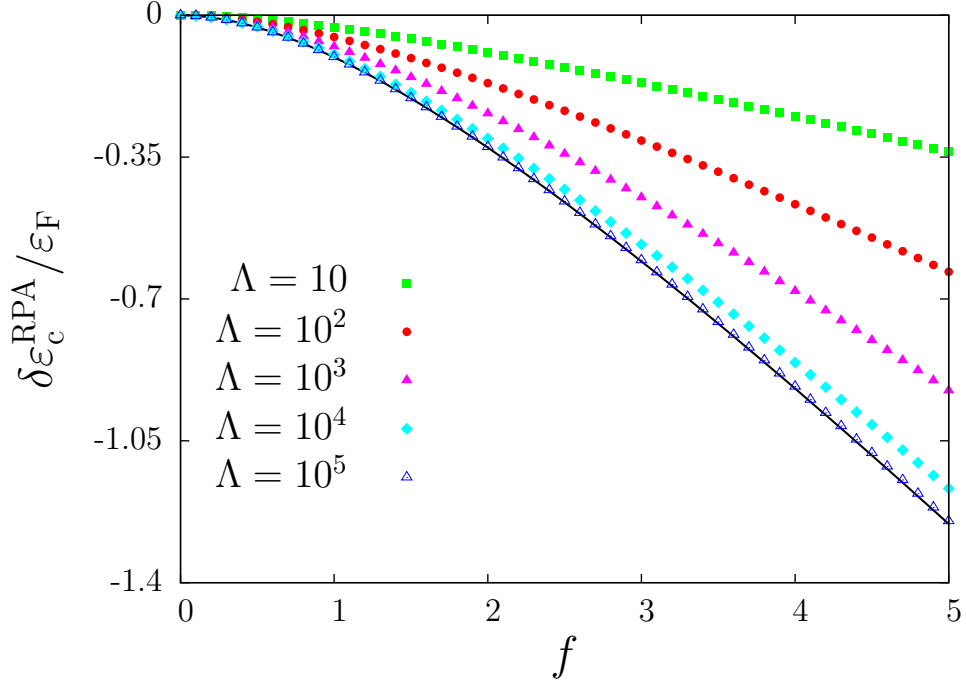


Figure 3.5: (Color online) Cut-off dependence of the regularized correlation energy  $\delta\epsilon_c^{\text{RPA}}$  in units of the Fermi energy  $\epsilon_F$ .

graphene layer. In typical circumstances  $f \sim 2$ .  $\Lambda$  is  $\sim 10$  in the most heavily doped samples studied experimentally and can in principle be arbitrarily large in lightly doped systems. We expect, however, that many of the electronic properties of graphene layers will be dominated by disorder when the doping is extremely light.

In Fig. 3.4 and Fig. 3.5 we plot the exchange and correlation energies of the graphene MDF model as a function of  $f$  for a range of  $\Lambda$  values. Note that both  $\delta\epsilon_x$  and  $\delta\epsilon_c^{\text{RPA}}$  have the same density dependence as  $\epsilon_F \propto n^{1/2}$  apart from the weak dependence on  $\Lambda$ . The exchange energy is positive because our

regularization procedure implicitly selects the chemical potential of undoped graphene as the zero of energy; doping either occupies quasiparticle states with positive energies or empties quasiparticles with negative energies. Note that including the RPA correlation energy weakens the  $\Lambda$  dependence so that the exchange energy per electron scales more accurately with  $\varepsilon_F$ . It is possible to analytically extract the asymptotic behavior of the exchange and correlation energies at large  $\Lambda$  by Laurent expanding the integrands of Eqs. (3.7)-(3.8) in  $q$  and retaining only the  $1/q$  terms:

$$\delta\varepsilon_x = \frac{1}{6g} f \varepsilon_F \ln(\Lambda) + \text{regular terms}, \quad (3.10)$$

and

$$\delta\varepsilon_c^{\text{RPA}} = -\frac{1}{6g} f^2 \xi(f) \varepsilon_F \ln(\Lambda) + \text{regular terms} \quad (3.11)$$

where

$$\xi(f) = 4 \int_0^{+\infty} \frac{dx}{(1+x^2)^2 (8\sqrt{1+x^2} + f\pi)}. \quad (3.12)$$

[Note that  $\xi(f=0) = 1/3$  so that the exchange and correlation energies are comparable in size for typical  $f$  values.]

## 3.2 Charge and Spin Susceptibilities

In an electron gas, the physical observables most directly related to the energy are the  $\Omega \rightarrow 0, q \rightarrow 0$  charge and spin-susceptibilities, normally discussed in terms of dimensionless ratios between non-interacting and interacting system values. The charge susceptibility is the inverse of the thermodynamic

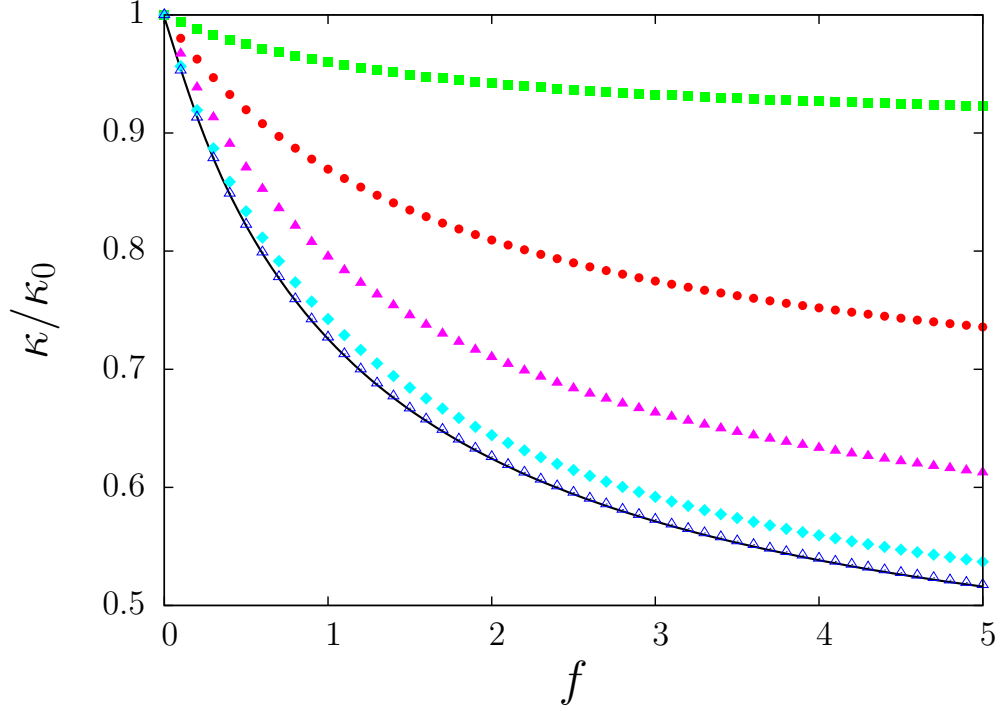


Figure 3.6: (Color online) Cut off  $\Lambda$  and coupling constant  $f$  dependence of  $\kappa/\kappa_0$ . The color coding is as in Figs. 3.4-3.5.

compressibility  $\kappa$  of the system up to a factor of  $n^2$ . For the MDF model of doped graphene

$$\frac{\kappa_0}{\kappa} = \frac{2n}{\varepsilon_F} \frac{\partial^2(n\delta\varepsilon_{\text{tot}})}{\partial n^2}, \quad (3.13)$$

and

$$\frac{\chi_0}{\chi_S} = \frac{2}{\varepsilon_F} \frac{\partial^2[\delta\varepsilon_{\text{tot}}(\zeta)]}{\partial \zeta^2} \Big|_{\zeta=0}, \quad (3.14)$$

where  $\delta\varepsilon_{\text{tot}}$  includes band, exchange, and correlation contributions. In Eq. (3.14)  $\zeta \equiv (n_\uparrow - n_\downarrow)/(n_\uparrow + n_\downarrow)$ ,  $\chi_S^{-1}$  measuring the stiffness of the system against changes in the density of electrons with spin  $\uparrow$  and spin  $\downarrow$ . In a 2D elec-

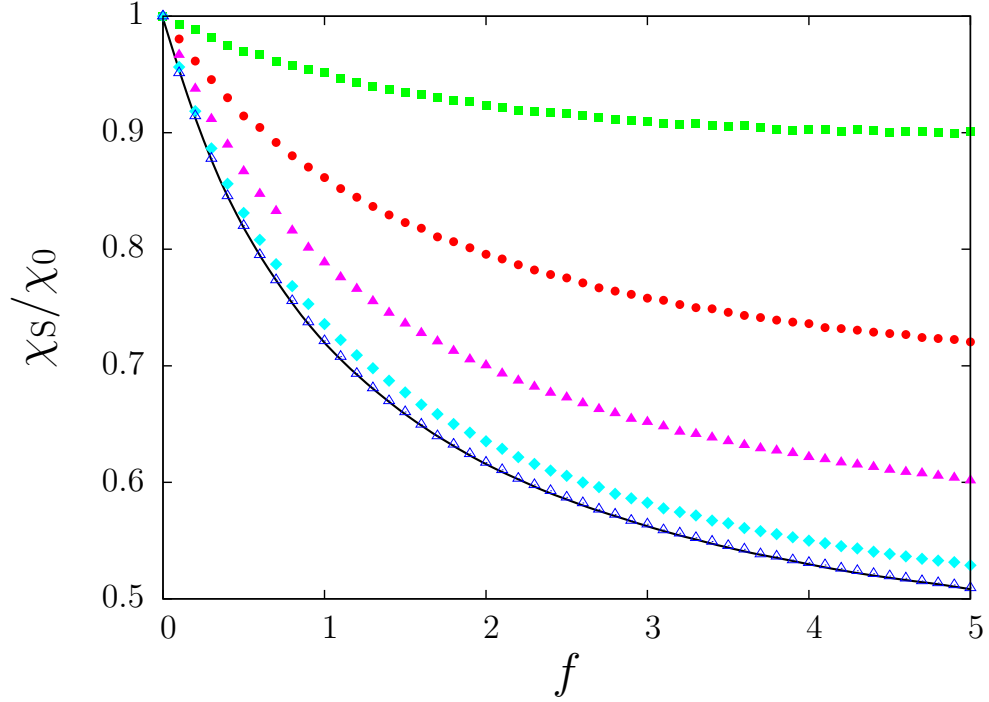


Figure 3.7: (Color online) Cut-off  $\Lambda$  and coupling constant  $f$  dependence of the spin susceptibility  $\chi_s$ . The color coding is as in Figs. 3.4-3.5.

tron systems the compressibility can be measured [43] capacitively. We note that this type of measurement is less difficult when  $\partial\mu/\partial n$  is large as it is in weakly-doped graphene. In bulk electronic systems, the spin-susceptibility can usually be extracted successfully from total magnetic susceptibility measurements, but these are likely to be challenging in the case of single-layer graphene. In two-dimensional electron systems, however, information about the spin-susceptibility can often [44] be extracted from weak-field magneto-transport experiments using a tilted magnetic field to distinguish spin and

orbital response.

Our results for the charge and spin-susceptibilities are summarized in Fig. 3.6 and Fig. 3.7. For experiments performed over the density range over which properties appear to be intrinsic in current samples ( $\Lambda$  between  $\sim 10$  and  $\sim 40$ ), these results predict compressibility and susceptibility suppression (apparent quasiparticle velocity enhancement) by approximately 15%. Both the sign of the interaction effect and the similarity of  $\kappa$  and  $\chi$  are in remarkable contrast with familiar electron gas behavior. In 3D and 2D non-relativistic electron gases both are [40, 45] strongly enhanced by interactions, with the charge response diverging at intermediate coupling and the spin response diverging at very strong coupling.

### 3.3 Discussion

The qualitative physics of ferromagnetism in metals is most transparent at the Hartree-Fock (HF) level. Similarly, the mechanism responsible for the unusual interaction physics of weakly doped graphene becomes clear when the exchange energy is expressed in terms of HF theory quasiparticle self-energies. Correlations do however play an essential quantitative role. For doped graphene the contribution of an individual channel to the HF theory interaction energy is

$$\begin{aligned} \delta\varepsilon_x &= -\frac{1}{2nS^2} \sum_{s,s'} \sum_{\mathbf{k},\mathbf{k}'} V_{s,s'}(\mathbf{k},\mathbf{k}') \delta n_{\mathbf{k}s} \delta n_{\mathbf{k}'s'} \\ &+ \frac{1}{nS} \sum_{\mathbf{k},s} \Sigma_{\mathbf{k},s}^{(0)} \delta n_{\mathbf{k}s} \end{aligned} \quad (3.15)$$

where  $s, s' = \pm$  are the chirality indices of the MDF bands (*i.e.* the eigenvalues of the chirality operator defined above),

$$\Sigma_{\mathbf{k},s}^{(0)} = -\frac{1}{S} \sum_{\mathbf{k}',s'} V_{ss'}(\mathbf{k}, \mathbf{k}') n_{s'}^{(0)}(\mathbf{k}') \quad (3.16)$$

is the HF self-energy of the *undoped* MDF model,

$$V_{s,s'}(\mathbf{k}, \mathbf{k}') = \frac{2\pi e^2}{|\mathbf{k} - \mathbf{k}'|} \left[ \frac{1 + ss' \cos(\theta_{\mathbf{k},\mathbf{k}'})}{2} \right] \quad (3.17)$$

is the exchange matrix elements between band states  $s', \mathbf{k}'$  and  $s, \mathbf{k}$ , and  $\cos(\theta_{\mathbf{k},\mathbf{k}'})$  is the angle between  $\mathbf{k}$  and  $\mathbf{k}'$ . For Coulomb interactions, the factor in square brackets on the right hand side of Eq. (3.17) tends to be larger between states in the same band, *i.e.* states with the same chirality.

The first term on the right-hand side of Eq. (3.15) is similar to the exchange energy of an ordinary two-dimensional electron system. Because it is negative and increases with density, its contribution to the exchange energy is lowered when spins are unequally populated. If this was the only exchange energy contribution, the spin-susceptibility and inverse compressibility would be enhanced by interactions as usual. The unusual behavior comes from the second term. For weakly doped graphene it is sufficient to expand  $\Sigma_{\mathbf{k},s}^{(0)}$  to first order in  $k$ ;  $\Sigma_{\mathbf{k}=0,s}^{(0)}$  is a physically irrelevant constant that is included in the chemical potential chosen as the zero of energy by our renormalization procedure. Expanding to first order in  $k$  gives the leading interaction contribution to the velocity renormalization [7, 8] of undoped graphene. In agreement with previous work we find that for large  $\Lambda$

$$v \rightarrow v \left[ 1 + \frac{f}{4g} \ln(\Lambda) \right]. \quad (3.18)$$

The physical origin of the velocity increase is the loss in exchange energy on crossing the Dirac point from states that have the same chirality as the occupied negative energy sea to states that have the opposite chirality. It is easy to verify that this velocity renormalization is responsible for the leading  $\ln(\Lambda)$  terms in the exchange energy and in the exchange contributions to  $\kappa^{-1}$  and  $\chi_S^{-1}$ . The conventional exchange energy contributes negatively to  $\kappa^{-1}$  and  $\chi_S^{-1}$  and competes with the Dirac point velocity renormalization.

When correlations are included, the leading  $\ln(\Lambda)$  contributions to the interaction energy and to  $\kappa^{-1}$  and  $\chi_S^{-1}$ , still follow from the (now altered) undoped system quasiparticle velocity renormalization. The enhanced quasiparticle velocity is tied to the Dirac point, *i.e.* to the switch in chirality, and results in an interaction energy that tends to be lower when the chemical potential is close to the Dirac point in all channels. Fig. 3.6 and Fig. 3.7 illustrate RPA theory predictions for experimentally observable consequences of the competition between this interband effect and conventional intraband correlations.

## Chapter 4

### Graphene: A Pseudochiral Fermi Liquid

Fermi liquid theory has been one of the seminal concepts in condensed matter physics. It not only describes the low-energy behavior of interacting electrons in most metals but also the low-energy behavior of Fermi systems such as  $^3\text{He}$  and nuclear matter irrespective of the complex details of these systems. Since the very first studies of the physical properties of metals it has been apparent that in spite of their mutual attraction, electrons in a metal behave as noninteracting independent particles. This is not easily justified as in most metals the Coulomb interaction energy for typical values of density can be close to the Fermi energy, which at first glance invalidates the use of standard perturbation theory. This issue was resolved by Landau who provided a theoretical framework for understanding the low-energy properties of interacting Fermi systems. Before we talk about graphene let us review some of the basic tenets of Landau's Fermi liquid theory.

Landau's basic idea is that the low-energy excitations of a system of interacting fermions with repulsive interaction can be constructed from the low-energy excitations of a non-interacting system by adiabatically switching on the interaction between the particles. This establishes a one-to-one correspondence between the eigenstates of an ideal system and a set of approximate eigen-

states of the interacting system. Since the eigenstates of the noninteracting system are specified by a set of occupations numbers, say  $\{\mathcal{N}_{\vec{k},\sigma}\}$  of single particle eigenstates, the low-energy excitation of the interacting systems can be studied by the same set of eigenstates. Landau argued that for excitations close to the Fermi surface these occupation numbers change very very slowly even for strong interactions thereby retaining their identity as approximate quantum numbers. The low-energy properties can be described by an addition or removal of quasiparticles from a filled Fermi sea with momentum  $k_F$ : for example the ideal state of a particle with momentum  $k > k_F$  outside the Fermi sea evolves into an excited state of the interacting system containing one quasiparticle with the same momentum outside a slightly modified Fermi sea.

The physical basis of Landau's Fermi liquid is in the ineffectiveness of the interaction's influence on the momentum distribution of the particles. It can be shown that in the limit of  $k \rightarrow k_F$  the quasiparticle lifetime  $\tau_{\vec{k}}$  approaches infinity. Thus on a time scale short compared to  $\tau_{\vec{k}}$  the occupation quantum number  $\{\mathcal{N}_{\vec{k},\sigma}\}$  can be regarded as a good quantum number.

The main properties of a quasiparticle excitation are included in the *effective mass*  $m^*$  and the *Landau interaction function*  $f_{\vec{k}'\sigma,\vec{k}\sigma'}$ . The effective mass modifies the bare mass  $m$  due to interactions and determines the energy of the quasiparticles  $\vec{\epsilon}_{\vec{k}} = k^2/2m^*$ . The Landau interaction function introduces an effective interaction between the quasiparticles. The beauty Landau's Fermi liquid theory is that the low-energy behavior of Fermi systems

can be described in terms of a few *Landau parameters* which can be simply related to  $f_{\vec{k}'\sigma, \vec{k}'\sigma'}$ . A more rigorous derivation of the concepts discussed above is provided by Shankar [1], in the Renormalization Group(RG) sense  $m^*$  and  $f_{\vec{k}'\sigma, \vec{k}'\sigma'}$  are fixed-points describing Landau's Fermi liquid theory and the excitations about this fixed points are the Landau quasiparticles.

As mentioned in the last chapter neutral graphene is a semi-metal with a point for a Fermi surface. It is prudent to ask if a Fermi liquid description survives for neutral graphene. The interaction hamiltonian for graphene involves a relativistic kinetic term and a non-relativistic interaction term:

$$\mathcal{H} = v_F \int d^2\vec{r} \psi^\dagger \vec{\sigma} \cdot i\nabla \psi + \frac{e^2}{2\epsilon} \int d^2\vec{r} d^2\vec{r}' \frac{1}{|\vec{r} - \vec{r}'|} \rho(\vec{r}) \rho(\vec{r}'). \quad (4.1)$$

The parameters in the theory  $v_F$  and  $e^2/\epsilon$  remain invariant under the dimensional scaling  $\vec{r} \rightarrow \lambda\vec{r}, \psi \rightarrow \lambda^{-1}\psi$ . As the strength of the Coulomb interaction does not change relative to the change in the kinetic terms, in the RG sense the Coulomb interaction is considered marginal. As shown towards the end of the last chapter the self energy in the Hartree-Fock approximation for doped graphene (similar calculation can be performed for neutral graphene) has a logarithmic renormalization:

$$\Sigma_{HF}(\vec{k}) = \frac{f}{4} k \log \left( \frac{\Lambda}{k} \right), \quad (4.2)$$

where  $\Lambda$  is a high-energy momentum cutoff. This logarithmic behavior survives for higher orders in perturbation theory as obtained in the random phase approximation [8] and also in the large N approximation [7]. This implies that the Fermi velocity is renormalized to higher and higher values and the

Coulomb interaction is renormalized towards lower values.

This can also be seen from the RG point of view: we can evaluate the effect of reducing the cut-off  $\Lambda$  on the coupling constant  $f$ . From 4.2 it can be shown that within the Hartree-Fock approximation the coupling constant  $f$  obeys the equation:

$$\Lambda \frac{\partial f}{\partial \Lambda} = -\frac{f}{4} \quad (4.3)$$

implying that Coulomb interaction become marginally irrelevant. Due to this renormalization of the Fermi velocity to higher values and Coulomb interaction to lower values neutral graphene is commonly referred to as a *marginal Fermi liquid*.

When Coulombic electron-electron interactions are included, doped graphene represents a new type of many-electron problem, distinct from both an ordinary 2DES and from quantum electrodynamics. The Hamiltonian in Eq. (3.2) differs from a Schrödinger equation in two crucial respects: i) its spectrum is not bounded from below and ii) its eigenstates have definite projection of pseudospin along the direction of momentum, *i.e.* definite pseudochirality, rather than definite pseudospin. We refer to the graphene 2DES as the chiral 2DES (C2DES). In this chapter we explain why the C2DES and the ordinary 2DES have distinctly different Fermi liquid properties. In the absence of a field, ordinary 2DESs are normal Fermi liquids [1, 46] in which interactions alter the Fermi velocity  $v \rightarrow v^*$ , introduce marginally irrelevant effective interactions between quasiparticles on the circular Fermi surface, and diminish the fraction  $Z$  of the spectral weight in the one-particle Green's function as-

sociated with its quasiparticle peak. The Fermi liquid phenomenologies of a C2DES and an ordinary 2DES have the same structure, since both systems are isotropic and have a single circular Fermi surface as illustrated in Fig. 2. The strength of interaction effects in an ordinary 2DES increases with decreasing carrier density. At low densities, the quasiparticle weight  $Z$  is small, the velocity is suppressed, the charge compressibility changes sign from positive to negative, and the spin-susceptibility is strongly enhanced. These effects, described with reasonable consistency [47–51] by theory and experiment, emerge from an interplay between exchange interactions and quantum fluctuations of charge and spin in the 2DES. In the C2DES we find that interaction effects also strengthen with decreasing density, although more slowly, that the quasiparticle weight  $Z$  tends to larger values, that the velocity is enhanced rather than suppressed, and that the influence of interactions on the compressibility and the spin-susceptibility changes sign. These qualitative differences are due to exchange interactions between electrons near the Fermi surface and electrons in the negative energy sea, to quasiparticle chirality, and to interband contributions to C2DES charge and spin fluctuations. The interband excitations are closely analogous to virtual particle-antiparticle excitations of a truly relativistic electron gas.

## 4.1 Random Phase Approximation of Self-energy

The technical calculation [52] on which our conclusions are based is an evaluation of the electron self-energy  $\Sigma$  of the C2DES near the quasiparticle-

pole.  $\Sigma$  describes the interaction of a single electron near the 2DES Fermi surface with all states inside the Fermi sea, and with virtual particle-hole and collective excitations of the entire Fermi sea, as illustrated in Fig. 2. As we discuss more explicitly below, a direct expansion of electron self-energy in powers of the Coulomb interaction is never possible in a 2DES because of the long-range of the Coulomb interaction. Our results for the C2DES are based on the random phase approximation (RPA) in which the self-energy is expanded to first order in the dynamically screened Coulomb interaction  $W$  (setting  $\hbar = 1$ ):

$$\Sigma_s(\mathbf{k}, i\omega_n) = -\frac{1}{\beta} \sum_{s'} \int \frac{d^2\mathbf{q}}{(2\pi)^2} \sum_{m=-\infty}^{+\infty} W(\mathbf{q}, i\Omega_m) \left[ \frac{1 + ss' \cos(\theta_{\mathbf{k}, \mathbf{k}+\mathbf{q}})}{2} \right] G_{s'}^{(0)}(\mathbf{k}+\mathbf{q}, i\omega_n + i\Omega_m), \quad (4.4)$$

where  $s = +$  for electron-doped systems and  $s = -$  for hole-doped systems,  $\beta = 1/(k_B T)$ ,

$$W(\mathbf{q}, i\Omega) = v_q + v_q^2 \chi_{\rho\rho}(\mathbf{q}, i\Omega), \quad (4.5)$$

$$\chi_{\rho\rho}(\mathbf{q}, i\Omega) = \frac{\chi^{(0)}(\mathbf{q}, i\Omega)}{1 - v_q \chi^{(0)}(\mathbf{q}, i\Omega)} \equiv \frac{\chi^{(0)}(\mathbf{q}, i\Omega)}{\varepsilon(\mathbf{q}, i\Omega)} \quad (4.6)$$

is the RPA density-density response function,  $\chi^{(0)}$  is its non-interacting limit [6, 41], and  $\varepsilon(\mathbf{q}, i\Omega)$  is the RPA dielectric function. For definiteness, we limit our discussion to an electron-doped system with positive chemical potential  $\mu$ : the Fermi liquid properties at negative doping are identical because of the C2DES model's particle-hole symmetry (see also Fig. 2).

In Eq. (??)  $\omega_n = (2n + 1)\pi/\beta$  is a fermionic Matsubara frequency, the sum runs over all the bosonic Matsubara frequencies  $\Omega_m = 2m\pi/\beta$  while in

Eqs. (4.5) and (4.6),  $v_q$  is the bare unscreened Coulomb interaction in 2D,  $v_q = 2\pi e^2/(\epsilon q)$  where  $\epsilon$  is an effective dielectric constant. The first and second terms in Eq. (4.5) are responsible respectively for the exchange interaction with the occupied Fermi sea (including the negative energy component), and for the interaction with particle-hole and collective virtual fluctuations. The factor in square brackets in Eq. (4.4), which depends on the angle  $\theta_{\mathbf{k},\mathbf{k}+\mathbf{q}}$  between  $\mathbf{k}$  and  $\mathbf{k} + \mathbf{q}$ , captures the dependence of Coulomb scattering on the relative chirality  $ss'$  of the interacting electrons. The Green's function  $G_s^{(0)}(\mathbf{k}, i\omega) = 1/[i\omega - \xi_s(\mathbf{k})]$  describes the free propagation of states with wavevector  $\mathbf{k}$ , Dirac energy  $\xi_s(\mathbf{k}) = svk - \mu$  (relative to the chemical potential) and chirality  $s = \pm$ . After continuation from imaginary to real frequencies,  $i\omega \rightarrow \omega + i\eta$ , the quasi-particle weight factor  $Z$  and the renormalized Fermi velocity can be expressed [52] in terms of the wavevector and frequency derivatives of the retarded self-energy  $\Sigma_+^{\text{ret}}(\mathbf{k}, \omega)$  evaluated at the Fermi surface ( $k = k_F$ ) and at the quasiparticle pole  $\omega = \xi_+(\mathbf{k})$ :

$$Z = \frac{1}{1 - \partial_\omega \Re \Sigma_+^{\text{ret}}(\mathbf{k}, \omega)|_{k=k_F, \omega=0}}, \quad (4.7)$$

and

$$\frac{v^*}{v} = \frac{1 + (v)^{-1} \partial_k \Re \Sigma_+^{\text{ret}}(\mathbf{k}, \omega)|_{k=k_F, \omega=0}}{1 - \partial_\omega \Re \Sigma_+^{\text{ret}}(\mathbf{k}, \omega)|_{k=k_F, \omega=0}}. \quad (4.8)$$

Following some standard manipulations [52] the self-energy can be expressed in a form convenient for numerical evaluation, as the sum of a contribution from the interaction of quasiparticles at the Fermi energy, the *residue* contribution  $\Sigma^{\text{res}}$ , and a contribution from interactions with quasiparticles far from the Fermi energy and via both exchange and virtual fluctuations, the *line*

contribution  $\Sigma^{\text{line}}$ . In the zero-temperature limit

$$\begin{aligned} \Sigma_+^{\text{res}}(\mathbf{k}, \omega) &= \sum_{s'} \int \frac{d^2\mathbf{q}}{(2\pi)^2} \frac{v_q}{\varepsilon(\mathbf{q}, \omega - \xi_{s'}(\mathbf{k} + \mathbf{q}))} \left[ \frac{1 + s' \cos(\theta_{\mathbf{k}, \mathbf{k} + \mathbf{q}})}{2} \right] \\ &\times [\Theta(\omega - \xi_{s'}(\mathbf{k} + \mathbf{q})) - \Theta(-\xi_{s'}(\mathbf{k} + \mathbf{q}))] \end{aligned} \quad (4.9)$$

and

$$\Sigma_+^{\text{line}}(\mathbf{k}, \omega) = - \sum_{s'} \int \frac{d^2\mathbf{q}}{(2\pi)^2} v_q \left[ \frac{1 + s' \cos(\theta_{\mathbf{k}, \mathbf{k} + \mathbf{q}})}{2} \right] \int_{-\infty}^{+\infty} \frac{d\Omega}{2\pi} \frac{1}{\varepsilon(\mathbf{q}, i\Omega)} \frac{\omega - \xi_{s'}(\mathbf{k} + \mathbf{q})}{[\omega - \xi_{s'}(\mathbf{k} + \mathbf{q})]^2 + \Omega^2}. \quad (4.10)$$

Note that at the Fermi energy  $\partial_k \Sigma_+^{\text{res}}(\mathbf{k}, \omega)$  vanishes, and  $\partial_\omega \Sigma_+^{\text{res}}(\mathbf{k}, \omega)$  involves an integral over interactions on the Fermi surface that are statically screened. These expressions differ from the corresponding 2DES expressions because of the relative chirality dependence of the Coulomb matrix elements, because of the linear dispersion of the bare quasiparticle energies, and most importantly because of the fast short-wavelength density fluctuations produced by the interband contribution to  $\chi^{(0)}(\mathbf{q}, i\Omega)$  illustrated in Fig. 3.

## 4.2 Results

Our results for  $Z$  and  $v^*/v$  are summarized in Fig. 4 as a function of the C2DES dimensionless coupling constant (restoring  $\hbar$ )

$$f \equiv \nu \frac{2\pi e^2}{\epsilon k_F} = g \frac{e^2}{\epsilon v \hbar}. \quad (4.11)$$

The appropriate value of  $f$  for a particular graphene sheet is dependent on its dielectric environment; for graphene on  $\text{SiO}_2$   $f \sim 2$ . As we discuss at greater length below, graphene's Fermi liquid properties depend only weakly on the

carrier density which is expressed in these figures in terms of the cut-off parameter  $\Lambda$ . The trends exhibited in Fig. 4 can be understood by considering the limits of small  $f$  and the limit of large  $q$  at all values of  $f$ . In the former limit screening is weak except at extremely small  $q$ . In  $\partial_\omega \Sigma_+^{\text{res}}(\mathbf{k}, \omega)$ , for example, the integral over  $q$  diverges logarithmically at small  $q$  when  $\varepsilon(\mathbf{q}, \omega = 0)$  is set equal to one, *i.e.* when screening is neglected. Screening cuts off this logarithmic divergence at a wavevector proportional to  $f$  so that  $\partial_\omega \Sigma_+^{\text{res}}(\mathbf{k}, \omega)$  has a contribution proportional to  $f \ln(f)$  at small  $f$ . Because  $\varepsilon(\mathbf{q}, \omega = 0)$  happens to be independent of  $q$  for transitions between Fermi surface points, it is possible to evaluate  $\partial_\omega \Sigma_+^{\text{res}}(\mathbf{k}, \omega)$  analytically. We find that

$$\frac{\partial}{\partial \omega} \Re \Sigma_+^{\text{res}}(\mathbf{k}, \omega) \Big|_{k=k_F, \omega=0} = \frac{f}{2\pi g} \left[ \sqrt{4-f^2} \ln \left( \frac{2 + \sqrt{4-f^2}}{f} \right) - \frac{1}{2}(4-f^2) \right] \quad (2)$$

Similar small  $q f \ln(f)$  contributions appear in the other elements which contribute to  $Z$  and  $v^*$ . All this behavior is very familiar from the case of the normal 2DES; the new differences present in the chiral C2DEG are ones of detail. At large  $q$ , on the other hand, interband charge fluctuations dominate  $\varepsilon(\mathbf{q}, \omega) - 1$ , which approaches its simple undoped system form. It becomes especially clear when  $\omega$  is expressed in units of  $vq$  that the typical value of  $\varepsilon(\mathbf{q}, \omega)$  at large  $q$  is  $\sim 1$  with a non-trivial dependence on  $f$ . The  $q$  integrals all vary as  $q^{-1}$ , requiring that the C2DES model be accompanied by an ultra-violet cut-off which for the case of graphene should be [6]  $q_c \sim 1/a$  where  $a$  is the graphene lattice constant. Since the crossover between intraband and interband screening occurs for  $q \sim k_F$ , it follows that both  $\partial_k \Sigma^{\text{line}}$  and  $\partial_\omega \Sigma^{\text{line}}$

have contributions that are analytic in  $f$  and vary as  $\ln(\Lambda)$  where  $\Lambda = q_c/k_F$  when  $\Lambda$  is large. To leading order in  $\ln(\Lambda)$  we find that

$$Z^{-1} - 1 = \frac{f\lambda(f)}{6g} \ln(\Lambda) \quad (4.13)$$

and that<sup>1</sup>

$$\frac{v^*}{v} - 1 = \frac{f[1 - f\xi(f)]}{4g} \ln(\Lambda) \quad (4.14)$$

where

$$\lambda(f) = \frac{48}{\pi} \int_0^{+\infty} dx \frac{1}{8\sqrt{1+x^2} + f\pi} \frac{x^2 - 1}{(1+x^2)^{3/2}} \quad (4.15)$$

and

$$\xi(f) = 4 \int_0^{+\infty} dx \frac{1}{8\sqrt{1+x^2} + f\pi} \frac{1}{(1+x^2)^2}. \quad (4.16)$$

Note that  $\lambda(f) = f/4 - 3\pi^2 f^2/256 + \dots$  and  $\xi(f) = 1/3 - 3\pi^2 f/256 + \dots$  are analytic functions of  $f$  because interband polarization screening does not essentially alter the Coulomb interaction at large  $q$ .

### 4.3 Discussions

The asymptotic expressions (4.13) and (4.14) approximately capture the contribution to the corresponding Fermi liquid parameters from interactions over the wavevector range from  $\sim k_F$  to  $\sim q_c$ . As the density decreases and  $k_F \rightarrow 0$  this contribution dominates. The Fermi wavelength then acts like a cut-off on the renormalization group flows which appear in the theory [53] of interaction effects in undoped graphene. The fact that the velocity increases

---

<sup>1</sup>Eq 4.14 is obtained after performing a weak-coupling expansion on Eq 4.8

in this regime can be understood qualitatively using Hartree-Fock theory [6], which is accurate at small  $f$  when  $\Lambda$  is large. In Hartree-Fock theory the enhanced velocity is due to the reduced exchange energy in a right-handed band when the negative energy sea is left-handed. In Fig. 4 we have also shown cut-off and coupling constant dependence of the antisymmetric Landau parameter  $F_0^a$ , which is defined in terms for the antisymmetric Landau interaction function  $f_a(\cos(\varphi))$  as [52]

$$F_\ell^a = \nu^* \int_0^{2\pi} \frac{d\varphi}{2\pi} f_a(\cos(\varphi)) \cos(\ell\varphi), \quad (4.17)$$

where  $\nu^* = gk_F/(2\pi v^*)$  is the density-of-states of the interacting system at the Fermi surface [ $f_a(\cos(\varphi))$  is obtained from the Fermi surface dependence of the self-energy [54]]. Physically,  $F_0^a$  determines the spin susceptibility  $\chi_S = (v/v^*)/(1 + F_0^a)$ . From our results in panels (b) and (c) of Fig. 4 we predict a rather large suppression of the spin susceptibility which could be measured in weak-field Shubnikov-de Haas magnetotransport experiments using a tilted magnetic field to distinguish spin and orbital response [48].

Our findings have important implications for density-functional-theory (DFT) and tight-binding modeling of ribbons [55, 56], quantum dots [57, 58], and other nanostructures made from graphene. Because of the pseudo-chiral properties of bulk quasiparticles, states tend to have a lower energy when they have the majority chirality. This interaction effect depends specifically on intersite coherence and is completely missing in the local-density-approximation and in other approximations for exchange and correlation potentials commonly

used in DFT. The accuracy of graphene nanostructure electronic structure calculations would be improved if they used exchange-correlation potentials based on the properties of the C2DES rather than on the properties of the ordinary 2DES.

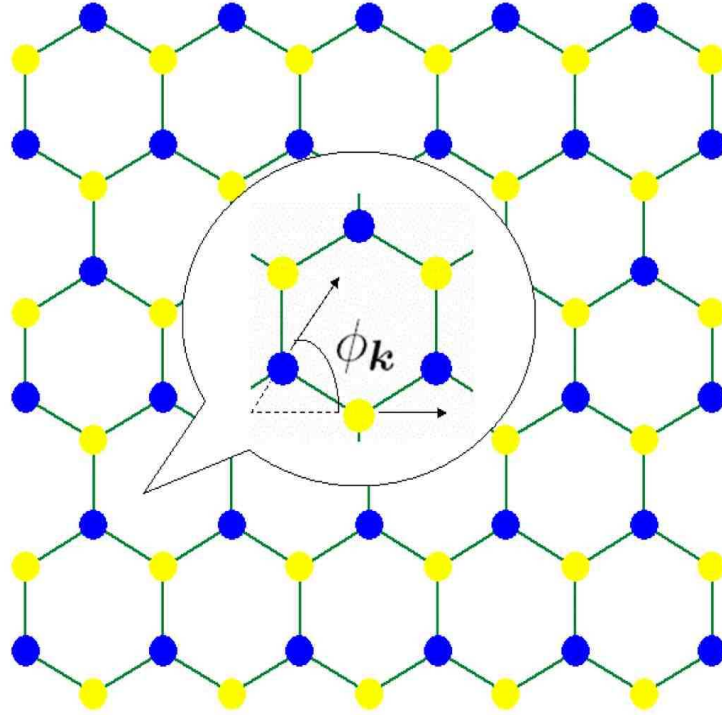


Figure 4.1: Honeycomb lattice of a single layer graphite flake with one sublattice in yellow and the other sublattice in blue. In the continuum limit the sublattice degree of freedom may be regarded as a pseudospin. When momentum  $\mathbf{k}$  is measured away from the Dirac points at the  $K$  and  $K'$  Brillouin zone corners, band eigenstates have definite projection of pseudospin in the  $\mathbf{k}$  direction, *i.e.* definite pseudochirality. The angle  $\phi_{\mathbf{k}}$  above denotes the momentum-dependent phase difference between wavefunction amplitudes on the two sublattices. For spin-1/2 quantum particles this angle is the azimuthal orientation of a pseudospin coherent state in the equatorial plane.

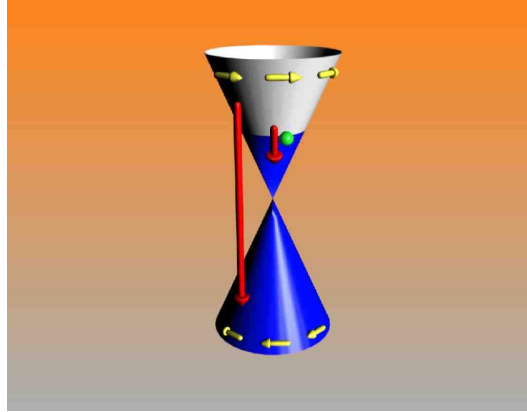


Figure 4.2: In a weakly doped material, graphene's energy bands can be described by a massless Dirac equation in which the role of spin is played by pseudospin. Like an ordinary 2DES, doped graphene has a circular Fermi surface. The Fermi liquid properties of graphene are a consequence of both exchange interactions between quasiparticles near the Fermi surface and states in the positive and negative energy Fermi seas and of interactions with both intra-band (short red vertical arrow) and inter-band (long red vertical arrow) virtual fluctuations of the electronic system. The yellow arrows in this figure indicate the pseudospin chirality of band eigenstates. Because of the difference in chirality between positive and negative energy bands, the velocity of graphene quasiparticles is enhanced by inter-band exchange interactions, tending to protect the system from magnetic and other instabilities, and reducing both charge and spin response functions.

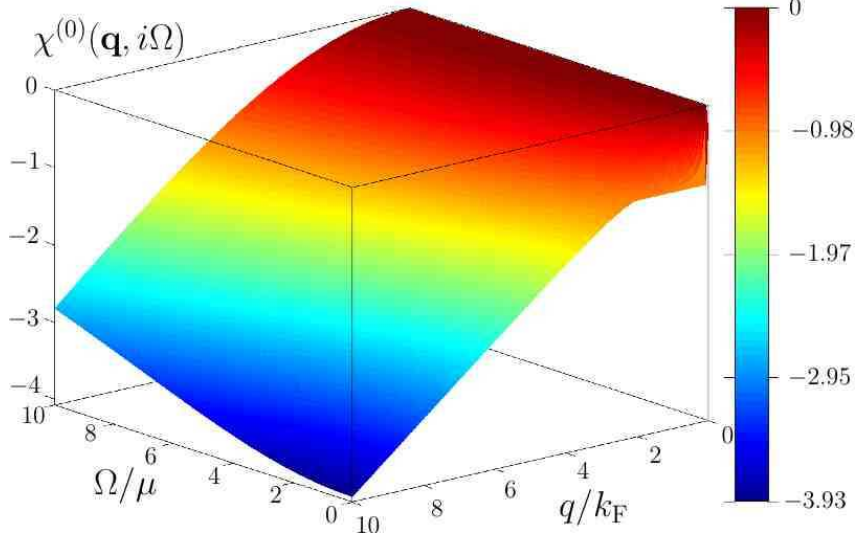


Figure 4.3: “Lindhard” function  $\chi^{(0)}(\mathbf{q}, i\Omega)$  of a C2DES, in units of the non-interacting density-of-states at the Fermi surface  $\nu = gk_F/(2\pi v)$ , as a function of  $q/k_F$  and  $\Omega/\mu$  on the imaginary frequency axis.  $k_F = (4\pi n/g)^{1/2}$  is the Fermi wavenumber,  $\mu = vk_F$  the Fermi energy,  $n$  the electron density and the flavor multiplicity  $g = g_s g_v = 4$  for graphene because of its two-fold valley degeneracy. Because of interband fluctuations  $\chi^{(0)}$  diverges linearly with  $q$  for  $q \rightarrow \infty$  and decays only like  $\Omega^{-1}$  for  $\Omega \rightarrow \infty$  in the C2DES, in contrast to the  $q^{-2}$  and  $\Omega^{-2}$  behaviors of the ordinary 2DES. In the static  $\Omega = 0$  limit  $\chi^{(0)}(\mathbf{q}, 0) = -\nu$  for all  $q \leq 2k_F$  for both chiral and ordinary 2DESs.

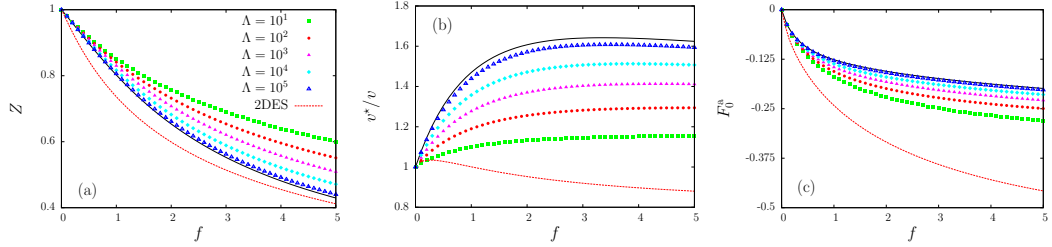


Figure 4.4: Density and coupling constant  $f$  dependence of some C2DES Fermi-liquid parameters. The density is specified by  $\Lambda \equiv q_c/k_F$ . The density range studied most extensively in experiment,  $n \sim 10^{11} \text{ cm}^{-2}$  to  $n \sim 10^{13} \text{ cm}^{-2}$ , corresponds to  $\Lambda = 100$  to  $\Lambda = 10$ . In all panels the black solid line corresponds to the highest value of the cut-off parameter we have considered,  $\Lambda = 2.7 \times 10^5$ . The red dashed line illustrates the RPA Fermi-liquid parameters of an ordinary non-chiral 2DES with parabolic bands. In this case the  $f = \sqrt{2} r_s$  [see Eq. (4.11)], where  $r_s = (\pi n a_B^2)^{-1/2}$  is the usual Wigner-Seitz density parameter and  $a_B = \epsilon \hbar^2 / (m_b e^2)$  the effective Bohr radius. From the left the three panels show: (a) the quasiparticle renormalization factor  $Z$  evaluated from Eq. (4.7); (b) the velocity renormalization factor evaluated from Eq. (4.8); and (c) the  $\ell = 0$  dimensionless Landau parameter  $F_0^a$  which characterizes spin-dependent quasiparticle interactions. The color coding for  $\Lambda$  is the same in all panels.

## Chapter 5

# Plasmons and The Spectral Function of Graphene

### 5.1 Introduction

The single-particle spectral function [40]  $\mathcal{A}(\mathbf{k}, \omega)$  captures the influence of Coulomb and phonon-mediated interactions on the energy band properties of crystals. In this chapter we report on a random-phase-approximation (RPA) theory of  $\mathcal{A}(\mathbf{k}, \omega)$  in two-dimensional (2D) honeycomb-lattice carbon crystals described by their Dirac equation continuum model [14]. Graphene sheets have attracted [9, 59, 60] attention recently because of unusual properties that follow from chiral band states, notably unusual quantum Hall effects [3, 4], and because of their potential for technological applications. We find that states near the Dirac point ( $\mathbf{k} = 0$ ) of a graphene sheet interact strongly with plasmons with a characteristic frequency  $\omega_{\text{pl}}^*$  that scales with the sheet's Fermi energy and depends on its interaction coupling constant  $\alpha_{\text{gr}}$ , producing plasmonic spectral function satellites. The resulting spectral functions, illustrated in Fig. 5.1, have a broad energy spread near the Dirac point and a gap between the extrapolations of right-handed and left-handed bands to  $\mathbf{k} = 0$ . We explain below why the Dirac point is special, even when it is not at the Fermi energy.

Angle-resolved photoemission spectroscopy (ARPES) is a powerful probe of  $\mathcal{A}(\mathbf{k}, \omega)$  in 2D crystals because it achieves momentum  $\mathbf{k}$  resolution [61]. Two recent experiments [62, 63] have reported ARPES spectra for single-layer graphene samples prepared by graphitizing the surface of Silicon Carbide (SiC) [64]. Although the data in Refs. [62, 63] are similar, the physical interpretations of the experimental findings are very different. Ref. [62] discusses the ARPES spectra in terms of electron-phonon [65] and electron-plasmon interactions, while Ref. [63] focuses mainly on the apparent band-gap opening at the Dirac point. A gap at the Dirac point can be explained without electron-electron interactions by assuming strong inversion symmetry breaking in the graphene layer due to coupling with the SiC substrate. Our theoretical results appear to allow an intrinsic interpretation for this feature, although it is clear that present experimental data is still partially obscured by incompletely controlled interactions with the substrate and by sample inhomogeneity which produces momentum space broadening.

The self-energy in a system of fermions can be separated into an exchange contribution due to interactions with occupied states in the static Fermi sea, and a correlation contribution due to the sea's quantum fluctuations [40]. Graphene differs [21] from the widely studied 2D systems in semiconductor quantum wells because its quasiparticles are chiral and because it is gapless and therefore has interband quantum fluctuations on the Fermi energy scale. In graphene, band eigenstate chirality endows exchange interactions with a new source of momentum dependence which renormalizes the quasiparticle

velocity and strongly influences the compressibility and the spin susceptibility [6, 66, 67].

## 5.2 Doped Dirac Sea Charge Fluctuations

The massless Dirac band Hamiltonian of graphene can be written as [9] ( $\hbar = 1$ )  $\mathcal{H} = v\tau(\sigma_1 p_1 + \sigma_2 p_2)$ , where  $\tau = \pm 1$  for the inequivalent  $K$  and  $K'$  valleys at which  $\pi$  and  $\pi^*$  bands touch,  $p_i$  is an envelope function momentum operator, and  $\sigma_i$  is a Pauli matrix which acts on the sublattice pseudospin degree-of-freedom. The low-energy valence band states have pseudospin aligned with momentum, while the high energy conduction band states, split by  $2v|\mathbf{p}|$ , are anti-aligned. In Fig. 5.2 we compare the particle-hole excitation spectra of non-interacting and interacting 2D doped Dirac systems. The noninteracting particle-hole continuum is represented here by the imaginary part of graphene's Lindhard function [6, 41],  $\Im m[\chi^{(0)}(\mathbf{q}, \omega)]$ , which weighs transitions by the strength of the density fluctuation to which they give rise. Transitions between states with opposite pseudospin orientation therefore have zero weight. More generally the band-chirality related density-fluctuation weighting factor (called the chirality factor below), which plays a key role in the physics of the spectral function, is  $[1 \pm \cos(\theta_{\mathbf{k}, \mathbf{k}+\mathbf{q}})]/2$  with the plus sign applying for intraband transitions and the minus sign applying for interband transitions, and  $\theta_{\mathbf{k}, \mathbf{k}+\mathbf{q}}$  equal to the angle between the initial state ( $\mathbf{k}$ ) and final state ( $\mathbf{k} + \mathbf{q}$ ) momenta. The weight is therefore high for intraband (interband) transitions when  $\mathbf{k}$  and  $\mathbf{k} + \mathbf{q}$  are in the same (opposite) direction. The

most important features in Fig. 4.2 are (i) the  $1/\sqrt{vq - \omega}$  divergence which occurs near the upper limit of the  $q < k_F$  intraband particle-hole continuum and (ii) the relatively weak weight at the lower limit of the  $q < k_F$  inter-band particle-hole continuum. The divergence at the intraband particle-hole spectrum contrasts with the singular but finite  $\sqrt{\omega_{\max} - \omega}$  behavior at the upper end of the particle-hole continuum in an ordinary electron gas. The difference follows from the linear quasiparticle dispersion which places the maximum intraband particle-hole excitation energy at  $vq$  for all  $k$  in the Dirac-model case.

In the RPA, quasiparticles interact with Coulomb-coupled particle-hole excitations. Because the bare particle-hole excitations are more sharply bunched in energy, Coulomb coupling leads to plasmon excitations that are sharply defined out to larger wavevectors than in the ordinary electron gas and steal more spectral weight from the particle-hole continuum. As seen in Fig. 5.2, the plasmon excitation  $\omega_{\text{pl}}(q)$  of the Dirac sea remains remarkably well defined even when it enters the interband particle-hole continuum. The persistence occurs because transitions near the bottom of the interband particle-hole continuum have nearly parallel  $\mathbf{k}$  and  $\mathbf{k} + \mathbf{q}$  and therefore little charge-fluctuation weight. *Interactions between quasiparticles and plasmons are stronger in the 2D massless Dirac system than in an ordinary parabolic-band 2D system.*

### 5.3 Dirac Quasiparticle Decay

In Fig. 4.3 we plot the imaginary part of the RPA theory [40] self-energy:

$$\Im m[\Sigma_s(\mathbf{k}, \omega)] = \sum_{s'} \int \frac{d^2\mathbf{q}}{(2\pi)^2} v_q \Im m[\varepsilon^{-1}(\mathbf{q}, \omega - \xi_{s'}(\mathbf{k} + \mathbf{q})) \left[ \frac{1 + ss' \cos(\theta_{\mathbf{k}, \mathbf{k} + \mathbf{q}})}{2} \right] \Theta(\omega - \xi_{s'}(\mathbf{k} + \mathbf{q})) - \Theta(-\xi_{s'}(\mathbf{k} + \mathbf{q}))]$$

where  $s, s' = \pm 1$  are band (chiral) indices,  $v_q = 2\pi e^2/(\epsilon q)$  is the 2D Coulomb interaction,  $\varepsilon(\mathbf{q}, \omega) = 1 - v_q \chi^{(0)}(\mathbf{q}, \omega)$  is the RPA dielectric function, and  $\Theta(x)$  is the Heaviside step function.  $\Im m[\Sigma]$  measures the band-quasiparticle decay rate. The two factors in square brackets on the right-hand-side of Eq. (5.1) express respectively the influence of chirality and Fermi statistics on the decay process. Note that  $\Sigma_s$  depends on the band-index  $s$  only through the chirality factor. For  $\omega > 0$  and fixed  $\mathbf{q}$ , the RPA decay process represents scattering of an electron from momentum  $\mathbf{k}$  and energy  $\omega$  to  $\mathbf{k} + \mathbf{q}$  and  $\xi_{s'}(\mathbf{k} + \mathbf{q})$ , with all energies in Eq. (5.1) measured from the Fermi energy. Since the Pauli exclusion principle requires that the final state is unoccupied, it must lie in the conduction band, *i.e.*  $s' = +1$ . Furthermore since the Fermi sea is initially in its ground state, the quasiparticle must lower its energy, *i.e.*  $\xi_{s'} < \omega$  – electrons decay by going down in energy. Because interaction and band energies in graphene's Dirac model both scale inversely with length,  $\Im m[\Sigma_s(\mathbf{k}, \omega)] = vk_F F(\omega/vk_F, k/k_F)$ . For large  $|x|$ ,

$F(x, y) \rightarrow -\pi\alpha_{\text{gr}}^2\ell(\alpha_{\text{gr}})|x|/(64g)$ , where  $\ell(0) = 4/3$  and  $\ell(2) \simeq 0.655124^1$ . This implies that for  $|\omega| \gg vk_{\text{F}}$ , the decay rate in a doped system ( $\Im m[\Sigma_s(\mathbf{k}, \omega)]$ ) approaches that of an undoped system. As we will see, however, doped system properties are quite different from those of an undoped system up to energies several times larger than the Fermi energy, particularly so near the Dirac ( $\mathbf{k} = 0$ ) point. The Fermi energy  $\varepsilon_{\text{F}} = vk_{\text{F}}$  is used as the energy unit and  $k_{\text{F}}$  as the unit of wavevector in all plots and in the remaining sections of this chapter.

In explaining the spectra plotted in Fig. 5.3 we start with the Dirac-point case for which the self-energy is band independent. For  $\mathbf{k} = 0$ , the final state energy  $\xi_{s'}(\mathbf{q}) = s'q - 1$  is independent of the direction of  $\mathbf{q}$ . Because most charge fluctuation spectral weight is transferred from the particle-hole continua to plasmonic excitations of the Dirac sea,  $\Im m[\Sigma_s(0, \omega)]$  tends to be dominated by plasmon emission contributions. For  $\omega > 0$  the final state must be unoccupied so that  $s' = +1$ ;  $q$  is restricted to those values larger than 1 for which the Dirac sea excitation energy  $\Omega(q) = \omega + 1 - q$  is positive. Comparing with Fig. 4.2 we see that  $\Im m[\Sigma_+(0, \omega)]$  vanishes like  $\omega^2$  for  $\omega \rightarrow 0$ , a universal property of normal Fermi liquids [46]. The sharp increase in  $\Im m[\Sigma_+(0, \omega)]$  which occurs at  $\omega \sim 1.2$  reflects the onset of plasmon emission. For  $\omega < 0$  both conduction and valence band final states occur and transitions are allowed if the transition energy  $\Omega(q) = |\omega| - 1 + s'q$  is positive

---

<sup>1</sup> $l(\alpha_{\text{gr}})$  has an analytical expression that is rather cumbersome and will be presented elsewhere

and the final hole state is occupied. Given  $\omega$ , plasmon emission contributions occur when  $\Omega(q) = \omega_{\text{pl}}(q)$  and are proportional to the plasmon spectral weight and to the density-of-states factor  $|s' - d\omega_{\text{pl}}/dq|^{-1}$ . The density-of-states factor is large for  $s' = +$  and diverges when  $\Omega(q)$  is tangent to  $\omega_{\text{pl}}(q)$ . The plasmon emission features in  $\Im m[\Sigma_+(0, \omega)]$  are more prominent for holes than for electrons because this factor cannot diverge in the latter case. We find that  $\Im m[\Sigma_s(0, \omega)] = -C \Theta(\omega + 1 + \omega_{\text{pl}}^*) \omega_{\text{pl}}^{*3/2} / \sqrt{\omega + 1 + \omega_{\text{pl}}^*}$  (with  $C \sim 0.8$ ) near the decay peak. If we approximate this peak by a  $\delta$ -function, setting  $\Im m[\Sigma_s(0, \omega)] \sim -\pi\Gamma^{*2} \delta(\omega + 1 + \omega_{\text{pl}}^*)$  and choosing the electron-plasmon coupling constant  $\Gamma^{*2}$  to reproduce the integrated strength of the feature over a  $\omega_{\text{pl}}^*$  energy interval, we obtain a simple model in which a single band state hole with energy  $-1$  interacts with a plasmon with energy  $\omega_{\text{pl}}^*$ . Because  $\Gamma^*$  is comparable to  $\omega_{\text{pl}}^*$  for all values of  $\alpha_{\text{gr}}$  (see top left panel in Fig. 5.3) a significant part of the Dirac point spectral weight is always transferred to a plasmaron [68] satellite separated from the Dirac point band energy by  $\sqrt{\omega_{\text{pl}}^{*2} + 4\Gamma^{*2}}$ . This plasmaron satellite could be responsible for the broad photoemission spectrum [62, 63] at the Dirac point in epitaxial graphene samples if the sharper features present in Fig. 5.1 are obscured in current data by disorder-induced momentum space broadening. Away from the Dirac point, the conduction and valence band  $\Im m[\Sigma_s(\mathbf{k}, \omega)]$  peaks broaden because of the dependence on scattering angle of  $\xi_{s'}(\mathbf{k} + \mathbf{q})$ , weakening any satellite features and the plasmaron satellite fades. The  $s = +$  and  $s = -$  peaks in  $\Im m[\Sigma_s]$  in Fig. 5.2 separate at finite  $k$  because of chirality factors which emphasize  $\mathbf{k}$  and  $\mathbf{q}$  in nearly parallel directions for

conduction band states and  $\mathbf{k}$  and  $\mathbf{q}$  in nearly opposite directions for valence band states. The conduction band plasmon emission peak moves up in energy approximately as  $vk$  and the valence band peak moves down as seen in the bottom panels of Fig. 5.3.

## 5.4 Spectral function

ARPES measures the wavevector dependent quasiparticle spectral function [40]. Near the Fermi energy the spectral function consists of a narrow Lorentzian centered at the energy  $E$  which solves the Dyson equation for the  $s = +$  quasiparticle energy,  $E = \xi_+(\mathbf{k}) + \Re[\Sigma_+(\mathbf{k}, E)]$ . Near the Dirac point, the  $s = +$  band spectrum separates into a quasiparticle peak shifted to lower energies as explained above. In Fig. 5.4 we see explicitly that for  $k = 0.25$  there are already two solutions to the Dyson equation, although the largest part of the spectral weight still belongs to the quasiparticle peak. We also note in Fig. 5.4 that  $\Re[\Sigma_s]$  has a negative contribution which is present at the Fermi energy and persists over a wide regime of energy. This contribution is due to exchange and correlation interactions of quasiparticles near the Fermi energy with the negative energy sea. As explained <sup>2</sup> [6, 21] previously,

---

<sup>2</sup> $\Re[\Sigma_s]$  is weakly dependent on the massless Dirac model's ultraviolet cutoff  $\Lambda$  [6, 21]. For this reason the spectral function  $\mathcal{A}_s(\mathbf{k}, \omega)$  is not exactly a function of only  $k/k_F$  and  $\omega/\varepsilon_F$ . This caveat is of little practical significance however since deviations are very small over the two to three orders of magnitude of graphene sheet charge density which lies the window between the low density cutoff  $\sim 10^{11}\text{cm}^{-2}$  below which disorder plays a strong role and the high density cutoff  $\sim 10^{14}\text{cm}^{-2}$  imposed by fundamental gating and doping limitations. The numerical results shown in this work have been calculated with  $\Lambda = 10^2$ .

this effect produces a nearly rigid shift in the band energies which is increasingly negative further below the Fermi energy, increasing the band dispersion and the quasiparticle velocity. Fig. 5.1 was constructed by combining results for  $\mathcal{A}_s(\mathbf{k}, \omega)$  at twenty different values of  $|\mathbf{k}|$  ( $\mathcal{A} = \sum_s \mathcal{A}_s$ ). The plasmaron satellite in the  $s = +$  band spectral function emerges gradually as  $|\mathbf{k}| \rightarrow 0$ . The  $s = -$  band spectral function is identical to the  $s = +$  band function at  $|\mathbf{k}| = 0$ , but is substantially broader at larger  $|\mathbf{k}|$  because of the large phase space for decay via particle-hole excitation further below the Fermi energy. The plasmaron satellite and the quasiparticle peak in the  $s = -$  band tend to merge into one broad peak as  $|\mathbf{k}|$  increases. The wavevector-dependent exchange and correlation energy shifts discussed above also influence how the spectral function broadens at the lowest energies. It is abundantly clear the spectral function of a doped system is similar to that of an undoped graphene system only for  $k \gg k_F$ .

Graphene ARPES spectra are influenced by disorder, coupling to the substrate, and by electron-phonon interactions, in addition to the electron-electron interaction effects considered here. Because interactions effects scale with  $vk_F$  energy scale, while phonon effects are fixed at optical phonon energy scales, these two contributions can be separated experimentally by varying carrier density. Our RPA theory demonstrates that broad quasiparticle peaks and apparent energy gaps near the Dirac point are expected even without substrate coupling. We expect that the present RPA theory results, combined with progress in the preparation of samples suitable for ARPES or for 2D to

2D tunneling spectroscopy [69], will enable further progress.

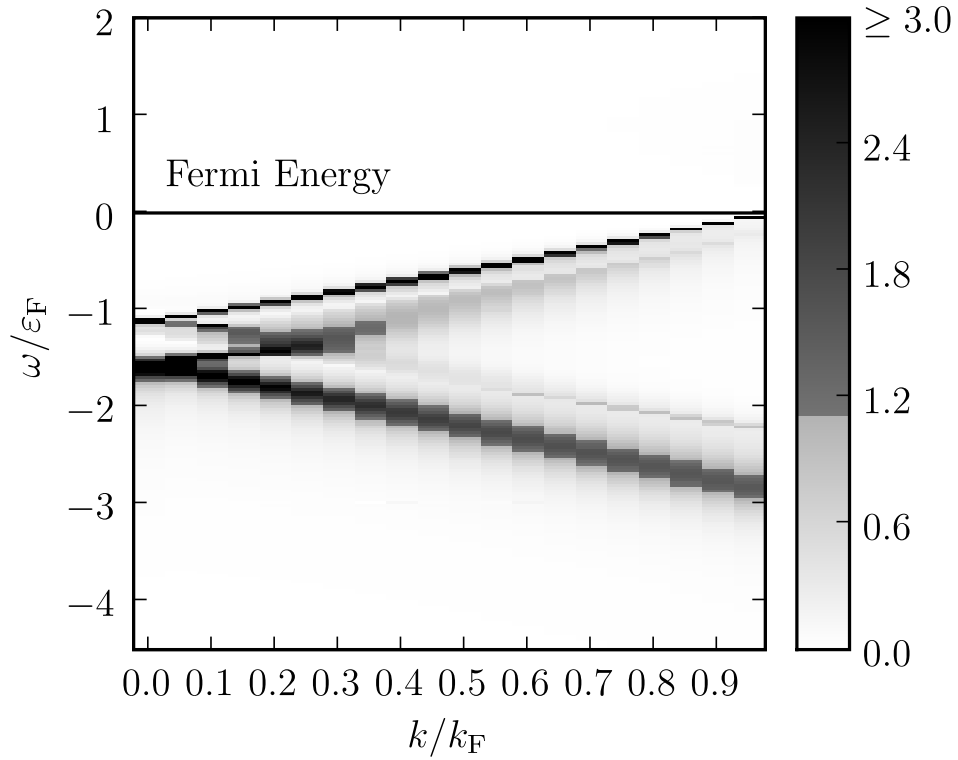


Figure 5.1: Spectral function  $\mathcal{A}(\mathbf{k}, \omega)$  of an n-doped graphene sheet as a function of  $k$  (in units of Fermi wavevector  $k_F$ ) and  $\omega$  (in units of and measured from the Fermi energy  $\hbar v k_F$  where  $v$  is the Fermi velocity). These results are for coupling constant  $\alpha_{\text{gr}} = ge^2/(\epsilon \hbar v) = 2$  (here  $g = 4$  is a spin-valley degeneracy factor and the dielectric constant  $\epsilon$  depends on the material which surrounds the graphene layer). For each  $k$  ARPES detects the portion of the spectral function with  $\omega < 0$ . The  $k$ -dependence is represented in this figure by results for twenty discrete  $k \in [0.0, 0.95]$ .

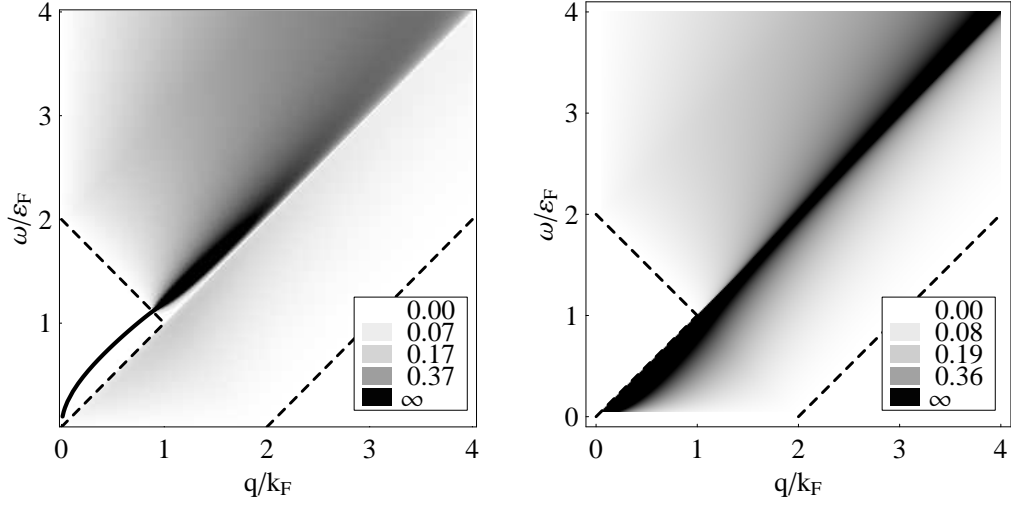


Figure 5.2: Left panel:  $-\Im m[\varepsilon^{-1}(\mathbf{q}, \omega)]$  as a function of  $q/k_F$  and  $\omega/\varepsilon_F$  for  $\alpha_{\text{gr}} = 2$ . The solid line is the RPA plasmon dispersion relation. The dashed lines are the boundaries of the electron-hole continuum. Right panel:  $-v_q \Im m[\chi^{(0)}(\mathbf{q}, \omega)]$  as a function of  $q/k_F$  and  $\omega/\varepsilon_F$ . The left and right panels become identical in the non-interacting  $\alpha_{\text{gr}} \rightarrow 0$  limit.

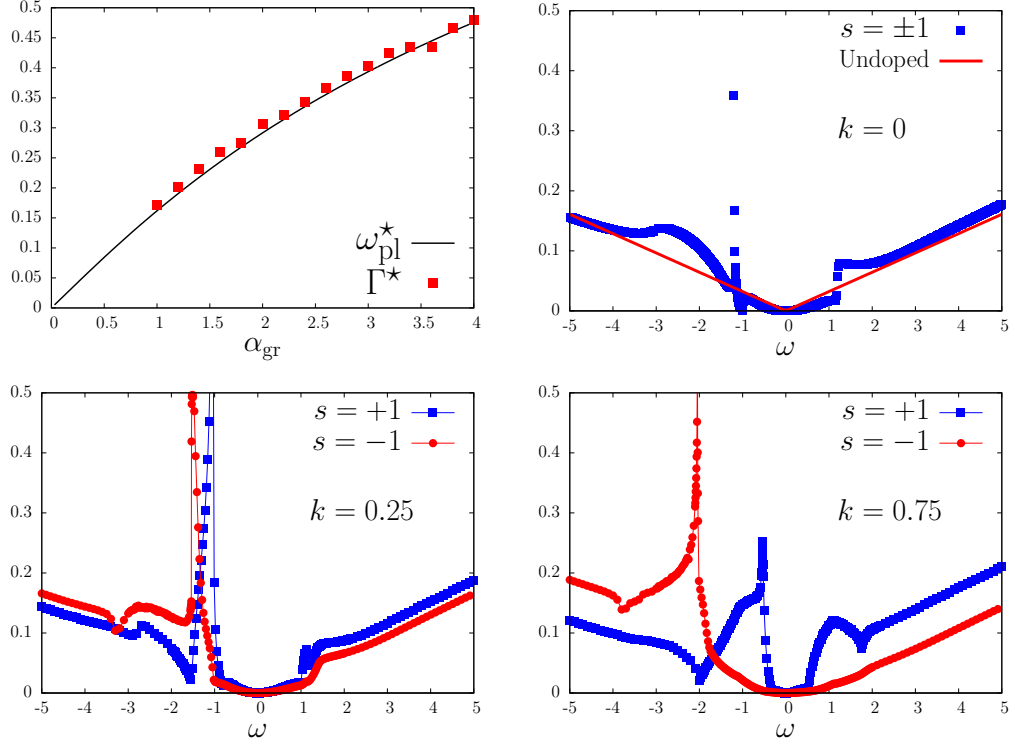


Figure 5.3: (Color online) Top left panel:  $\omega_{\text{pl}}^*$  (solid line) and  $\Gamma^*$  (filled squares) as functions of  $\alpha_{\text{gr}}$ . Other panels: The absolute value  $|\Im[\Sigma_s(\mathbf{k}, \omega)]|$  of the imaginary part of the RPA quasiparticle self-energy (in units of  $\varepsilon_{\text{F}}$ ) of an n-doped system as a function of energy  $\omega$  for  $k = 0, 0.25$ , and  $0.75$  and  $\alpha_{\text{gr}} = 2$ .

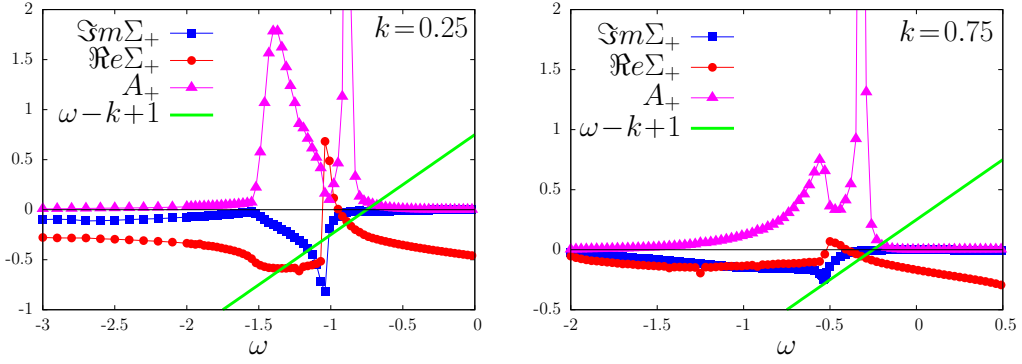


Figure 5.4: (Color online)  $\Re[\Sigma_+(\mathbf{k}, \omega)]$ ,  $\Im m[\Sigma_+(\mathbf{k}, \omega)]$ , and spectral function  $\mathcal{A}_+(\mathbf{k}, \omega)$  for  $k = 0.25$  and  $k = 0.75$ . The band energy and  $\Re[\Sigma_+]$  are measured from the band  $\varepsilon_F$  and interaction  $[\Sigma_+(k_F, \omega = 0)]$  contributions to the chemical potential.

## Chapter 6

# Quantum Hall Ferromagnets

2DEGs have been a long been a fertile source of surprising new physics for more than four decades, most notably in the presence of a strong magnetic field when they exhibit the integer and fractional quantum Hall effects. As we have seen in chapter 2 due to the unusual properties of chiral fermions in a magnetic field, systems like graphene and bilayer graphene have opened a new arena in quantum hall physics. A particularly interesting aspect involves the possibility of novel and exotic strongly correlated states that can appear due to the  $4J$ -fold degeneracy of the lowest Landau level. Even though research in graphene is still in its infancy, an optimistic extrapolation of the trend towards improved mobility [10] in current samples indicates that experimental investigation of strongly correlated quantum hall physics in chiral systems is not too far in the future. This might lead to interesting new surprises that add to the richness of quantum hall physics. In the next chapter we perform a theoretical study of Quantum Hall Ferromagnetism in bilayer graphene's chiral system at a strong magnetic field. Before we do this let us we review salient features of the rich phenomenology associated with quantum hall physics in 2DEGs with a special focus on Quantum Hall Ferromagnetism.

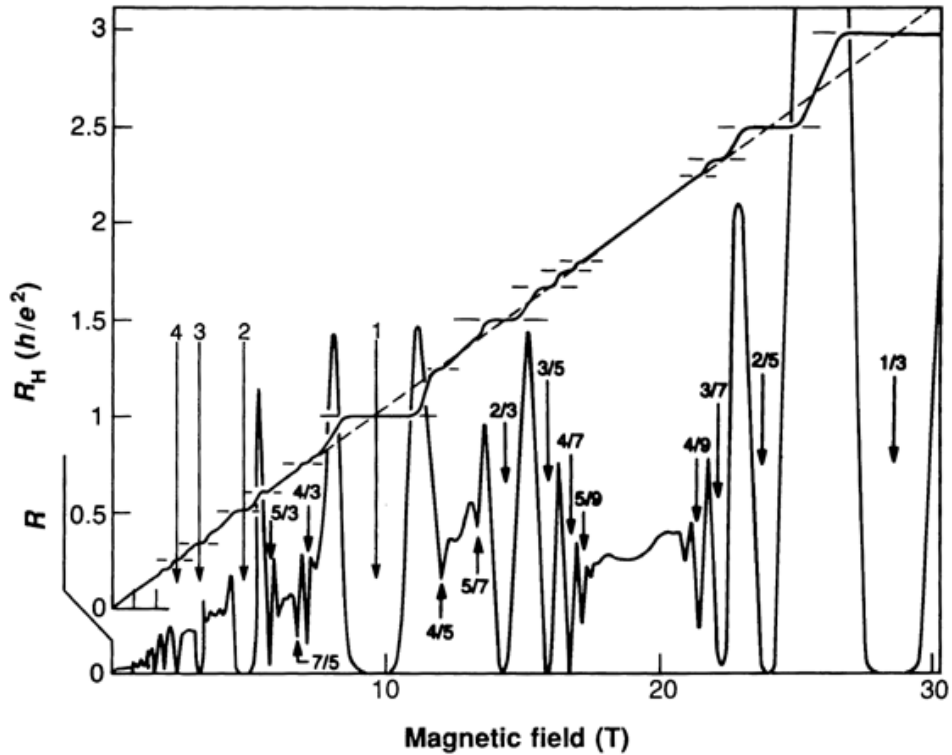


Figure 6.1: This figure shows hall plateaus at integer and fractional filling as a function of the magnetic field strength  $B$ .

## 6.1 Review of Quantum Hall Effect

Integer and Fractional quantum hall effect was discovered almost unexpectedly in the early 1980s [34–37]. Since then the physics community has witnessed tremendous progress in this area [70]. It is now understood that a 2DEG in the presence of a magnetic field is incompressible at certain Landau level filling factors [70, 71]:

$$\frac{1}{\kappa} \sim \frac{d\mu}{dn} \rightarrow \infty; \quad (6.1)$$

the discontinuity of the chemical potential as a function of the density indicates that it costs a finite amount of energy to introduce a single charge in the system. Whenever there is an incompressibility the energy to add or remove a particle differ in the thermodynamic limit, it follows that it costs finite energy to create a particle-hole pair that are not bound to each other and can carry a current, this is referred to as 'charge gap'. This incompressibility or equivalently charge gap is responsible for the plateaus in the off-diagonal Hall resistance  $\rho_{xy}$  and the vanishing longitudinal resistance  $\rho_{xx}$  at low temperatures. It can also be shown that it is this incompressibility that leads to the quantization of Hall conductance.

The origin of this incompressibility is different for the integer and fractional quantum hall effects. In the integer Hall effect the charge gap arises due to the quantization of the energy spectrum into Landau levels or due to the Zeeman gap between spin states, this is essentially a single particle effect and fairly easy to understand. In contrast Fractional hall effect requires partial filling of a Landau level, and the charge gap arises due to electron-electron interactions. The Coulomb interaction energy scale is approximately  $e^2/\epsilon l_B$  (which scales like  $\sqrt{B}$ ) much lower than the Landau level gap (which scales like  $B$ ) in a high magnetic field. It is then useful to think of electrons confined to the lowest Landau level where the kinetic energy is a constant and can be absorbed in the zero of energy. Interactions then dominate the physics leading to many body states that are highly correlated incompressible quantum fluids.

Soon after the experimental discovery of Fractional Hall Effect [36]

Laughlin wrote a variational wavefunction to describe the incompressible quantum hall fluid at filling factor  $\nu = 1/m$  (where  $m$  is odd) [37]:

$$\Psi_m(z_1, \dots, z_N) = \prod_{i < j} (z_i - z_j)^m e^{-\frac{1}{4} \sum_i |z_i|^2}, \quad (6.2)$$

which is totally antisymmetric for odd values of  $m$ , cannot be expressed as a Slater determinant of single particle wavefunctions and shows stronger correlations than those of a Fermi liquid. Using analogy with one-component plasma [37] Laughlin also showed that 6.2 describes a uniform quantum liquid exhibiting fractionally charged excitations. Laughlin's wavefunction minimizes the interaction energy by capturing even units of magnetic flux quanta. Laughlin's wavefunction has all the vortices attached to the position of the particles, the probability of any two electrons approaching each other is therefore strongly suppressed, in fact the electrons stay as far away from each other as possible thereby lowering the Coulomb energy.

Laughlin wavefunction only describes the fractions of the form  $\nu = \frac{1}{m}$  whereas rational fractions of the form  $\nu = p/q$  with  $q$  odd have also been observed experimentally, and can be described by subsequent hierarchy schemes developed by Haldane [72] and Halperin [73]. Jain [74] described an alternate view of other filling factors by proposing that electrons capture magnetic flux quanta thereby transforming to composite fermions; Fractional QHE for electrons can then be mapped to Integer QHE of composite fermions. There has been extensive work done in fractional Hall physics and still remains a topic of interest for theorist [75] and experimentalist alike, interested reader can look

at a number of excellent reviews on this subject [70, 75, 76].

## 6.2 Quantum Hall Ferromagnets

In the previous section we have assumed that the electrons in the lowest Landau levels are spin polarized due to the presence of an external magnetic field. This can be justified, as discussed earlier, by arguing that the interaction energy scales like  $\sqrt{B}$  whereas Zeeman energy is proportional to  $B$ . However due to the low effective mass and spin-orbit coupling the Zeeman gap is only 1/60 of the Landau level gap in GaAs comparable to the interaction energy at experimentally attainable magnetic fields. It is therefore important to consider the spin of the electron. Another interesting class of systems are double layer quantum hall systems where two layers of 2DEGs are brought in close proximity to each other, such that they are coupled by interlayer Coulomb interaction and interlayer tunnelling along with intralayer Coulomb interaction. In such systems the *which layer* degree of freedom introduces a new (pseudo)spin along with the physical spin already present in these systems.

Any two level system can be viewed as a '(pseudo)spin' system, i.e. the hamiltonian and all other operators can be expressed in terms of Pauli matrices. This mapping allows us to relate to the more familiar problem of spin systems. Although the physical origin for the two systems could in principle be quite different, the mathematical description and physical consequences are identical to real spin systems. We can define the pseudospin on a Bloch sphere

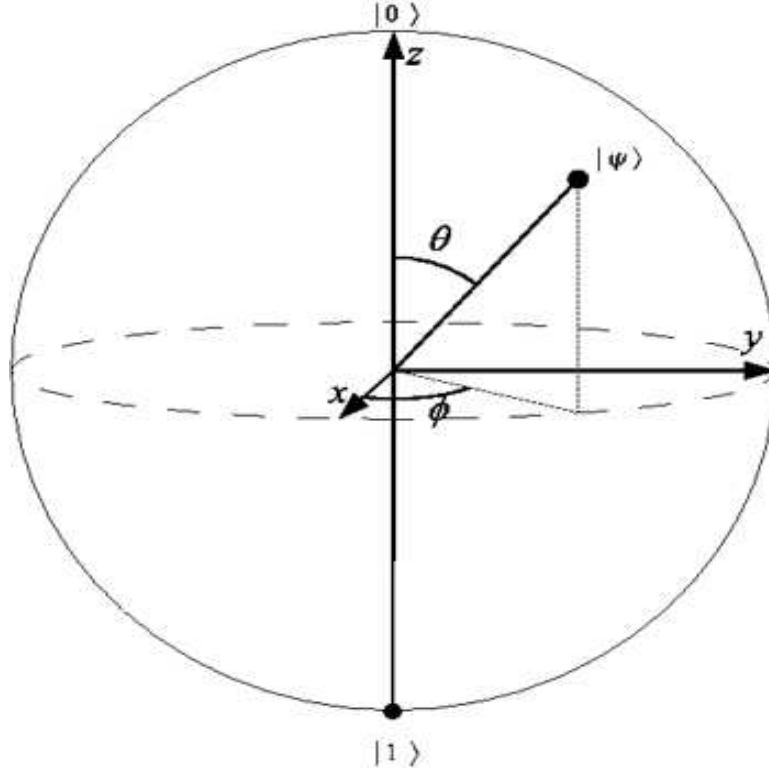


Figure 6.2: The direction of the local magnetization is  $\vec{m} = (\sin \theta \cos \phi, \sin \theta \sin \phi, \cos \theta)$

parameterizing the direction of spin by Euler angles  $\theta$  and  $\phi$ ,

$$\begin{pmatrix} \cos(\frac{\theta}{2}) \\ \sin(\frac{\theta}{2})e^{i\phi} \end{pmatrix}. \quad (6.3)$$

In the layer language  $\theta \neq 0$  would then correspond to the electron being a linear combination of up and down layer i.e. *the electron is in both layers*.

In single layer quantum hall system the kinetic energy is quenched by the external magnetic field and there is good exchange energy between the spins, i.e. the spins in the systems choose to spontaneously polarize even in

the limit of vanishing Zeeman energy. This happens for integer and fractional filling even though the orbital wavefunction is different at all filling factors. In the presence of Coulomb interaction Hund's rule suggests that the system lower its interaction energy by maximizing its total spin, since states with maximum total spin are symmetric and the orbital wavefunction 6.2 is anti-symmetric with respect to particle interchange, this gives a total antisymmetric wavefunction. This represents 100% spin polarization and is a perfect itinerant ferromagnet as there is no competition with kinetic energy.

In the limit of zero Zeeman energy single layer quantum hall ferromagnets have SU(2) invariance in the spin degree of freedom which is spontaneously broken when the system exhibits maximum spin polarization. This simply resembles a Heisenberg ferromagnet with low energy spin wave excitations  $\omega_q \sim q^2$  in the long wavelength limit. The low energy effective hamiltonian has the familiar NL $\sigma$ M form [84]:

$$\frac{1}{2}\rho_s \int d^2\vec{r}(\nabla m^\mu) \cdot (\nabla m^\mu), \quad (6.4)$$

here the order parameter  $\vec{m}$  represents the direction of the local magnetization, and  $\rho_s$  is the spin stiffness to spatial variations of  $\vec{m}$ . The spin stiffness depends on the nature of Coulomb interactions and the underlying orbital ground state wavefunction. There is a charge gap in this system as the addition or removal of an electron would cause a loss in the good exchange energy. The charge gap here is purely associated to Coulomb interactions. Similar to Heisenberg ferromagnets single layer quantum hall ferromagnets also exhibit spin textures called 'skyrmions'. In the case of quantum hall ferromagnets

these topological excitations carry charge and are the lowest charged excitations of this system [77, 84].

This is very different from the quantum hall effect in double layer systems<sup>1</sup>, for the rest of the discussion we neglect real spin in these systems. Unlike the single layer system the Coulomb interaction in a double layer system is layer(pseudospin) dependent. In the absence of tunneling between the layers the double layer system can be viewed as an *easy-plane quantum itinerant ferromagnet* [84] with pseudospin polarized in the XY plane with a spontaneously broken  $U(1)$  symmetry<sup>2</sup>. This corresponds to an electron being in a coherent superposition of both layers. Neglecting layer thickness the Coulomb potential is pseudospin dependent: electrons in the same layer interact via intralayer Coulomb potential  $v_S(q) = 2\pi e^2/q$  whereas electrons in different layers interact via the interlayer Coulomb potential  $v_D(q) = v_S(q)e^{-qd}$  where  $d$  is the distance between the layers. The hamiltonian can be separated into a pseudospin independent and pseudospin dependent part. It is the pseudospin dependent part that reduces the symmetry of the hamiltonian from  $SU(2)$  to  $U(1)$ .

The hamiltonian for a double layer system can be written as  $\mathcal{H} = \mathcal{H}_+ + \mathcal{H}_-$

$$\mathcal{H} = \frac{1}{2} \int \frac{d^2q}{(2\pi)^2} v_+(\vec{q}) \hat{\rho}(-\vec{q}) \hat{\rho}(\vec{q}) + 2 \int \frac{d^2q}{(2\pi)^2} v_-(\vec{q}) \hat{S}^z(-\vec{q}) \hat{S}^z(\vec{q}) \quad (6.5)$$

---

<sup>1</sup>Double layer systems exhibit a wide variety of nontrivial collective states at different filling factors. Here we only focus on total filling factor  $\nu = 1$  (i.e. 1/2 in each layer).

<sup>2</sup>Tunneling introduces pseudospin anisotropy in the XY plane, forcing the pseudospin to point along the x-axis.

where  $\hat{\rho}(\vec{q})$  is the fourier transform of the electronic spin density summed over layers,  $\hat{\mathcal{S}}_\alpha^z = \frac{1}{2}(\hat{\rho}_\alpha^t - \hat{\rho}_\alpha^b)$  is the z-component pseudospin density operator, and  $v_\pm$  are the symmetric and antisymmetric combinations of interaction potentials for electrons in the same(different) layer. Since  $v_S > v_D$ ,  $v_-$  is positive and produces an easy plane, as opposed to Ising, pseudospin anisotropy. This term prefers that the pseudospin lie in the  $XY$  plane: as when the pseudospin orientation moves out of the  $XY$  plane ( $\langle \mathcal{S}^z \rangle \neq 0$ ) and the energy increases. The physical origin of this energy cost is the charging energy of the capacitor due to unbalanced densities in the two layers, since  $\mathcal{S}^z$  measures the charge difference between the two layers, the pseudospin lies in the  $XY$  plane.

This term also increases the effect of quantum fluctuations since it does not commute with the order parameter [78]:

$$[\mathcal{H}_-, \mathcal{S}^\mu] \neq 0, \quad (6.6)$$

where  $\mu = x, y$ . The total spin is no longer a sharp quantum number. The effect of quantum fluctuations become important for large layer separation and produce a phase transition to two uncoupled layers. When the layers are widely separated there will be no correlations between the two layers and no appearance of a quantum hall plateau since each layer has  $\nu = 1/2$  [79]. The resulting phase diagram shown in Fig 6.3 has been verified experimentally.

To address the issue of collective modes of a double layer quantum hall system it is convenient to assume the pseudospin is polarized in the  $\hat{x}$ -direction. The energy change associated with small oscillation of the spins

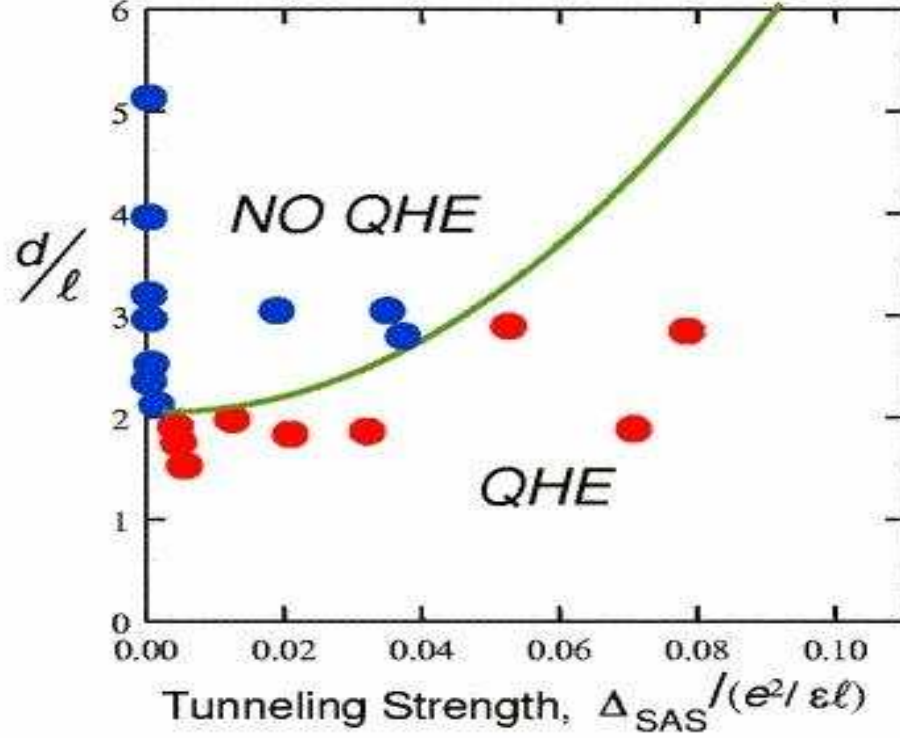


Figure 6.3: Phase diagram of a double layer quantum hall system. The phase boundary indicates the collapse of hall plateau as a function of layer separation and tunnelling.

from the  $\hat{x}$ -direction, in the long wavelength limit can be written as [84]:

$$E[\vec{m}] \approx \int d^2q \beta (m^z)^2 + \frac{\rho_A}{2} q^2 |m^z|^2 + \frac{\rho_E}{2} q^2 (|m^x|^2 + |m^y|^2). \quad (6.7)$$

We can see from the above expression that rotations out of the  $xy$  plane are costly due to the local mass term associated with  $m^z$ . This is exactly due to the capacitive energy as interaction favor equal population of densities in both layers. The collective mode dispersion is gapless and is the Goldstone mode associated with the broken  $U(1)$  symmetry. The collective mode dispersion in

the long wavelength limits is given by  $\omega_q \approx |q|$ , linear rather than quadratic due to the presence of the massive field  $m^z$ .

The linear gapless dispersion discussed above and the absence of gapless charged excitations suggests that double layer quantum hall systems exhibit superfluid behavior. This has interesting consequences on transport experiments in these systems [80]. These systems also exhibit four flavors of topologically charged excitations called 'merons' which are essentially half skyrmions [84]. The unbinding of these topological defects also leads to the Kosterlitz-Thouless phase transition even at zero temperature, due to the quantum fluctuations, if the layer separation exceeds some critical value [81].

In the next chapter we study Quantum Hall Ferromagnetism in bilayer graphene which shares some characteristics with double layer quantum hall systems. This system is interesting due to the presence of a 8-fold degeneracy in neutral bilayer graphene in a magnetic field. This adds an additional orbital pseudospin degree of freedom and new physics to the already rich structure discussed in this chapter.

## Chapter 7

# Octet Quantum Hall Ferromagnets in Bilayer Graphene

Because the Zeeman spin-splitting in most two-dimensional electron systems (2DES's) is much smaller than the Landau level separation, the magnetic band spectrum usually consists of narrowly-spaced doublets. When one of these doublets is half-filled and disorder is weak, Coulomb interaction physics leads to ferromagnetism *i.e.* to spontaneous spin polarization in the absence of a Zeeman field [82–84]. In some circumstances [85] other approximate Landau level degeneracies occur, often associated with layer degrees of freedom. These can also lead to broken symmetries which induce quasiparticle gaps and hence interaction driven integer quantum Hall effects. The case of bilayer 2DES's is particularly interesting because the *which layer* degree of freedom doubles Landau level degeneracies and leads to exciton condensation [86, 87] at odd filling factors and to canted anti-ferromagnetic states [88] at even filling factors. In this Chapter, we address the still richer case of graphene bilayer 2DES's in which chiral bands lead to an additional degeneracy doubling [13] at the Fermi energy of a neutral system. Bilayer graphene's Landau level octet is already apparent in present experiments [5] through the  $8 \times (e^2/h)$  Hall conductivity jump between well formed plateaus at Landau

level filling factors  $\nu = -4$  and  $\nu = +4$ . We anticipate that when external magnetic fields are strong enough or disorder is weak enough [89], interactions will drive quantum Hall effects at the octet's seven intermediate integer filling factors. We predict that these quantum Hall ferromagnets (QHF's) will exhibit unusual intra-Landau-level cyclotron modes at odd filling factors, and that the collective mode excitations at these filling factors are nearly gapless even when there is no continuous symmetry breaking. Because the conductivity has Drude weight centered near zero-energy, we speculate that localization physics and quantum-Hall related transport phenomena will also be anomalous.

## 7.1 Graphene Bilayer Landau Levels

When trigonal warping [90] and Zeeman coupling are neglected, the low energy properties of Bernal stacked unbalanced bilayer graphene are determined by electron-electron interactions and by a band Hamiltonian [13]  $\mathcal{H} = \mathcal{H}_0 + \mathcal{H}_{ext}$  where

$$\mathcal{H}_0 = \frac{1}{2m} \begin{pmatrix} 0 & \pi^{\dagger 2} \\ \pi^2 & 0 \end{pmatrix}, \quad (7.1)$$

and the influence of an external potential difference  $\Delta_V$  between the layers is captured by

$$\mathcal{H}_{ext} = \xi \Delta_V \left[ \frac{1}{2} \begin{pmatrix} 1 & 0 \\ 0 & -1 \end{pmatrix} - \frac{v^2}{\gamma_1^2} \begin{pmatrix} \pi^\dagger \pi & 0 \\ 0 & -\pi \pi^\dagger \end{pmatrix} \right]. \quad (7.2)$$

In Eqs. (7.1)-(7.2),  $\vec{\pi} = \vec{p} + (e/c)\vec{A}$  is the 2D kinetic momentum,  $\pi = \pi_x + i\pi_y$ , the  $2 \times 2$  matrices act on the pseudospin degree of freedom associated with

the two low energy sites [13] (the top and bottom layer sites without a near-neighbor in the opposite layer),  $v$  is the single-layer Dirac velocity,  $\gamma_1 \sim 0.4\text{eV}$  is the inter-layer hopping amplitude, and the effective mass  $m = \gamma_1/2v^2 \approx 0.054m_e$ .  $\mathcal{H}$  describes both K ( $\xi = 1$ ) and K' ( $\xi = -1$ ) valleys provided that we choose the pseudospin representation  $(A, \tilde{B})$  for K and  $(\tilde{B}, A)$  for K'.

Defining the usual raising and lowering Landau level ladder operators  $a^\dagger, a$  with  $a^\dagger = (l_B/\sqrt{2\hbar})\pi$ , where  $l_B = (\hbar c/eB)^{1/2} = 25.6/\sqrt{B[\text{Tesla}]} \text{nm}$  is the magnetic length, zero-energy eigenstates of  $\mathcal{H}_0$  can be identified using the property that  $a^2\phi_n = 0$  for 2D orbitals with Landau level index  $n = 0, 1$ . *In bilayer graphene the  $n = 0$  and  $n = 1$  orbital Landau levels are members of the same octet.* This peculiarity is behind most of the physics explored in this chapter. Neutral bilayer graphene's Landau-level octet is the direct product of three  $S = 1/2$  doublets: real spin and which-layer [91] pseudospins (as in a normal bilayer), and the Landau-level pseudospin  $n = 0, 1$  degree of freedom which is responsible for new physics. Zeeman coupling produces real spin-splitting  $\Delta_Z$  while  $\Delta_V$  gives rise to layer-splitting as in normal bilayers, but also to a small splitting of the Landau-level pseudospin which plays a central role in the physics:  $\Delta_{LL} = \Delta_V \hbar\omega/\gamma_1 \equiv \hbar\omega_{LL}$  where  $\hbar\omega = 2\hbar^2v^2/l_B^2\gamma_1 = 2.14 B[\text{Tesla}] \text{meV}$ .

The interaction contribution to the graphene bilayer Hamiltonian is layer-dependent:

$$\mathcal{H}_{int} = \sum_{\alpha\beta} \frac{1}{2} \int \frac{d^2q}{(2\pi)^2} v_+(\vec{q}) \hat{\rho}_\alpha(-\vec{q}) \hat{\rho}_\beta(\vec{q}) + 2 \int \frac{d^2q}{(2\pi)^2} v_-(\vec{q}) \hat{S}_\alpha^z(-\vec{q}) \hat{S}_\beta^z(\vec{q}) \quad (7.3)$$

In Eq. (7.3),  $\hat{\rho}_\alpha(\vec{q})$  is the  $\alpha$ -component of the electronic spin density summed over layers,  $\hat{S}_\alpha^z = \frac{1}{2}(\hat{\rho}_\alpha^t - \hat{\rho}_\alpha^b)$  is the z-component of the corresponding pseudospin density operator, and  $v_\pm$  are the symmetric and antisymmetric combinations of interaction potentials for electrons in the same(different) layer  $v_s = 2\pi e^2/\varepsilon q$  ( $v_d = v_s e^{-qd}$ ). In graphene bilayers, the layer separation  $d = 0.334\text{nm}$  so that, in contrast to what is typical in the semiconductor bilayer case,  $d/l_B \ll 1$  and hence  $v_-$  is weak.

Because of the incompressible nature of quantum Hall states, we expect that the graphene bilayer octet is well described at integer filling factors by Hartree-Fock (HF) mean-field theory. The importance of quantum fluctuation corrections to the ground state can be assessed using a weak-coupling theory of the octet's elementary excitations.

## 7.2 Octet Hunds Rules

The octet HF Hamiltonian [92] contains single-particle pseudospin splitting fields and direct and exchange interaction contributions:

$$\begin{aligned} \langle n\tau\alpha | \mathcal{H}_{HF} | n'\sigma\beta \rangle &= E_H(\rho_\tau - \rho_\beta) - \sum_{n_1 n_2} (X_{n_2 n' n n_1}^+ + \xi_\tau \xi_\sigma X_{n_2 n' n n_1}^-) \rho_{\tau\sigma\alpha\beta}^{n_1 n_2} \\ &+ (\xi_\tau \Delta_{LL} \delta_{n,1} \delta_{n',1} - \frac{\Delta_Z}{2} \xi_\alpha \delta_{nn'} - \frac{\Delta_V}{2} \xi_\tau \delta_{nn'}) \delta_{\alpha\beta} \delta_{\tau\sigma}, \end{aligned} \quad (7.4)$$

where  $n = 0, 1$  are LL indices,  $\tau, \sigma = t(b)$  are valley indices,  $\alpha, \beta = \uparrow (\downarrow)$  are spin-indices, and  $\xi_{\tau(\alpha)} = 1(-1)$  for t(b) layer and  $\uparrow (\downarrow)$  spins respectively. In Eq. (7.4)  $\rho_\tau = \sum_{n\alpha} \rho_{\tau\tau\alpha}^{nn}$  is the total electron density in layer  $\tau$ . The density-matrix  $\rho_{\tau\sigma\alpha\beta}^{n_1 n_2} = \langle c_{n_2\sigma\beta}^\dagger c_{n_1\tau\alpha} \rangle$  must be determined self consistently by occupying

the lowest energy eigenvectors of  $\mathcal{H}_{HF}$ . The Hartree-field  $E_H$  captures the electrostatic contribution to the bilayer capacitance,  $E_H = (e^2/\epsilon l_B)(d/2l_B)$ , and the exchange fields capture fermion quantum-statistics:

$$X_{n_2 n' n n_1}^\xi = \int \frac{d^2 \mathbf{p}}{(2\pi)^2} v_\xi(\mathbf{p}) F_{n_2 n'}(\mathbf{p}) F_{n n_1}(-\mathbf{p}). \quad (7.5)$$

In Eq.( 7.5)  $v_\pm$  are the symmetric and antisymmetric combinations of same (s) and different (d) layer electron-electron interactions ( $v_s = 2\pi e^2/\epsilon q$   $v_d = v_s e^{-qd}$ ), and the form factors ( $F_{00}(\mathbf{q}) = e^{-(ql_B)^2/4}$ ,  $F_{10}(\mathbf{q}) = (iq_x + q_y)l_B e^{-(ql_B)^2/4}/\sqrt{2} = [F_{01}(-\mathbf{q})]^*$  and  $F_{11}(\mathbf{q}) = (1 - (ql_B)^2/2)e^{-(ql_B)^2/4}$ ) reflect the character of the two different quantum cyclotron orbits.

The solution of the Hartree-Fock equations for balanced bilayers ( $\Delta_V = 0$ ) is summarized in Fig.[ 7.1] using a Zeeman field strength corresponding to  $B = 20\text{T}$ . The large gaps ( $\sim (\pi/8)^{1/2}$  in  $e^2/\epsilon l_B$  units) separating occupied and empty states at the odd integer filling factors of primary interest justify our weak-coupling theory. The octet filling, proceeding in integer increments starting from filling factor  $\nu = -4$ , follows a Hunds rule behavior: first maximize spin-polarization, then maximize layer-polarization to the greatest extent possible, then maximize Landau-level polarization to the extent allowed by the first two rules. For balanced bilayers the layer symmetric states (S) are filled before the layer antisymmetric states (AS). The first four states to be filled are (S, $n = 0, \uparrow$ ), (S, $n = 1, \uparrow$ ), (AS, $n = 0, \uparrow$ ) and (AS, $n = 1, \uparrow$ ) in this order. This sequence is then repeated for the next four states with down ( $\downarrow$ ) spin. The Hunds rules imply that the Landau-level pseudospin is polarized at all odd

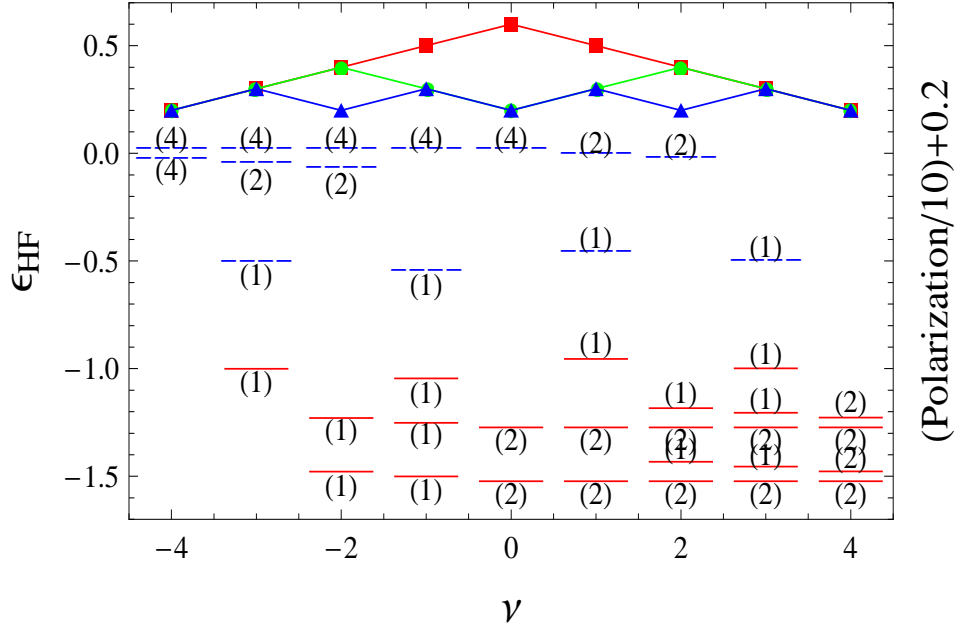


Figure 7.1: (Color online) Filling factor dependence of the integer filling factor HF theory occupied state ( spectrum of the bilayer graphene octet at  $\Delta_V = 0$ ). Energies of occupied (red - solid lines) and unoccupied (blue - dashed lines) are in units of  $(\pi/2)^{1/2}e^2/\epsilon l_B$ . The Zeeman field  $\Delta_Z$  value in these units is 0.023 at a magnetic field of 20T. Octet space fractional pseudospin polarizations offset for clarity: spin(red boxes), valley(green circles) and LL pseudospin(blue triangles).

integer filling factors between  $\nu = -4$  and  $\nu = 4$ . The physics of this new type of pseudospin polarization is the main focus of this chapter. An important distinction between layer and Landau-level polarization is that the former is associated with spontaneous inter-layer phase coherence whenever a Landau level occupies both layers simultaneously, whereas the latter polarization is driven by the Landau-level dependence of the microscopic Hamiltonian.

Octet quantum Hall ferromagnets have an interesting and intricate dependence on the external potential  $\Delta_V$ . Because the two-layers are close together, a small value of  $\Delta_V$  is sufficient to change the character of the layer polarization from the  $XY$  spontaneous-coherence form, to an Ising polarization form in which one layer is occupied before the other. We find that for  $\Delta_V$  larger than a critical value  $\Delta_V^*$ , the layer filling proceeds by filling the top layer first. (For  $\nu = -3$ ,  $\Delta_V^* = 0.1023(0.40)$  meV at  $B = 20(50)$  Tesla.) As we explain later, this filling sequence has qualitative consequences for the odd-integer filling factor LL pseudospin polarized states.

### 7.3 Landau-Level Pseudospin Dipoles

We now focus on the LL pseudospin fluctuations of a state with odd-integer filling factor, freezing spin and layer degrees of freedom. The collective excitation spectrum of graphene bilayer octets as a function of  $\nu$  and  $\Delta_V$  will be described in full detail elsewhere [93]. Fluctuating LL spinors are linear combinations of  $n = 0$  orbitals (even with respect to their cyclotron orbit center) and  $n = 1$  orbitals (odd with respect to orbit center), and therefore carry an electric dipole proportional to the in-plane component of their pseudospin. Because dipole-dipole interactions are long-range, they play a dominant role in the QHF long-wavelength effective action[84]. We find that

$$S[\vec{m}] = \int dt \left[ \int d^2q \vec{A} \cdot \partial_t \vec{m} - E[\vec{m}] \right], \quad (7.6)$$

where the first term is the Berry-phase contribution[84, 94] and for small fluctuations away from  $m_z = 1$  (full  $n = 0$  polarization)

$$E[\vec{m}] = \frac{e^2}{\epsilon l_B} \int d^2q \left[ \frac{1}{2|q|} (\vec{q} \cdot \vec{m})^2 + \frac{\tilde{\Delta}_{LL}}{2} (m_x^2 + m_y^2) \right]. \quad (7.7)$$

where  $\tilde{\Delta}_{LL} = \Delta_{LL}/(e^2/\epsilon l_B)$ . The mass terms in Eq.( 7.7) are due to the single-particle splitting between  $n = 0$  and  $n = 1$  levels and the interaction term is due to electric-dipole interactions. The absence of interaction contributions to the mass terms is a surprise, since the interaction is Landau-level pseudospin dependent. We address this point below. Because of the in-plane electric dipoles associated with LL pseudospinors, the long-wavelength pseudo-spinwave collective mode dispersion is not analytic:  $\hbar\omega \rightarrow (\Delta_{LL}^2 + \Delta_{LL}e^2q/\epsilon)^{1/2}$ , and for  $\Delta_{LL} \rightarrow 0$  is proportional to  $q^{3/2}$  when exchange interactions are included in the energy functional. The in-plane dipoles are also responsible for the intra-Landau-level cyclotron resonance discussed below.

To explain the absence of interaction contributions to the mass terms and address shorter-wavelength fluctuations it is necessary to derive the action microscopically. It is convenient to temporarily restrict fluctuations to one space direction by considering Landau-gauge states in which the LL pseudospins at different guiding centers  $X$  fluctuate independently:

$$|\psi[z]\rangle = \prod_X (z_{0X}c_{0X}^\dagger + z_{1X}c_{1X}^\dagger)|0\rangle, \quad (7.8)$$

where the spinor components  $z_{nX}$  satisfy the normalization constraint  $|z_{0X}|^2 +$

$|z_{1X}|^2 = 1$ . The corresponding imaginary-time action is

$$\begin{aligned} \mathfrak{S}[\bar{z}, z] = \mathfrak{S}_B + \mathcal{E} &= \int_0^\beta d\tau \sum_{Xn} \bar{z}_{nX} \partial_\tau z_{nX} + \sum_{XX'} \left( \frac{1}{2} \sum_{n_i} [H(X - X') \right. \\ &\quad \left. - F(X - X')] \bar{z}_{n_1X} z_{n_3X} \bar{z}_{n_2X'} z_{n_4X'} + \xi \Delta_{LL} \bar{z}_{1X} z_{1X'} \right), \end{aligned} \quad (7.9)$$

where  $\mathfrak{S}_B$  is the Berry's phase term and  $\mathcal{E} = \langle \psi[z] | (\mathcal{H} + \mathcal{H}_{int}) | \psi[z] \rangle$  is the energy functional. In Eq. (7.9) the direct( $H$ ) and exchange( $F$ ) energy contributions depend on the LL pseudospin labels,

$$\begin{aligned} H_{n_3, n_4}^{n_1, n_2}(X) &= \frac{1}{L_y} \int \frac{dq}{2\pi} v_q F_{n_1 n_4}(q) F_{n_2 n_3}(-q) e^{-iq_x X}, \\ F_{n_3, n_4}^{n_1, n_2}(X) &= \frac{1}{L^2} \sum_{\mathbf{q}} v_{\mathbf{q}} \delta_{q_y, X} F_{n_1 n_3}(\mathbf{q}) F_{n_2 n_4}(-\mathbf{q}). \end{aligned} \quad (7.10)$$

This action can be identified as the Schwinger boson[94] coherent state path integral representation of a model with pseudospins at each guiding center. We can introduce a bosonic creation operator  $a_{nX}^\dagger$  corresponding to  $\bar{z}_{nX}$  and let  $\mathcal{E}[\bar{z}, z] \rightarrow \mathcal{H}[a^\dagger, a]$ .

To analyze fluctuations around the HF mean field state, we use the linear spin wave approximation

$$a_{0X} \rightarrow 1 - \frac{1}{2} a_X^\dagger a_X \quad a_{1,X} \rightarrow a_X. \quad (7.11)$$

Taking the continuum limit  $1/L_y \sum_X = \int dX / (2\pi l_B)$ , the action describing harmonic fluctuations can be written in Fourier space as  $S = S_0 + \delta S$  where

$$\delta S = \frac{e^2}{\varepsilon l_B} \int_0^\beta d\tau \sum_{\mathbf{q}} \left[ \left( \frac{1}{2} \sqrt{\frac{\pi}{2}} + \xi_q \right) a_q^\dagger a_q + \frac{\lambda_q}{2} (a_q a_{-q} + a_q^\dagger a_{-q}^\dagger) \right], \quad (7.12)$$

with

$$\begin{aligned}\xi_q &= \frac{|ql_B|}{2} e^{-\frac{(ql_B)^2}{2}} - \int dp \left(1 - \frac{p^2}{2}\right) J_0(ql_B p) e^{-\frac{p^2}{2}} + \xi \tilde{\Delta}_{LL}, \\ \lambda_q &= \frac{|ql_B|}{2} e^{-\frac{(ql_B)^2}{2}} - \int dp \frac{p^2}{2} J_2(ql_B p) e^{-\frac{p^2}{2}},\end{aligned}\quad (7.13)$$

In Eq.( 7.12) we have restored [95] two-dimensional wavevectors to recognize the system's spatial anisotropy. The first and second terms in the above expressions capture the direct( $H$ ) and exchange( $F$ ) contributions respectively and  $J_0$  and  $J_2$  are the zeroth and second order Bessel functions. It can be verified that Eq.( 7.12) reduces to Eq.( 7.9) for  $q \rightarrow 0$ . The quadratic action in Eq. (7.12) has the familiar Bogoliubov form and the energy dispersion of the collective mode is given by:

$$\omega(q) = \frac{e^2}{\varepsilon l_B} \left( \left( \frac{1}{2} \sqrt{\frac{\pi}{2}} + \xi_q \right)^2 - |\lambda_q|^2 \right)^{1/2}. \quad (7.14)$$

As shown in Fig.[ 7.2], this collective mode has a roton minimum at  $ql_B \sim 2.3$  and approaches the Hartree-Fock theory band splitting for  $q \rightarrow \infty$  as expected.[82] The surprising absence of interaction contributions to the gap at  $q = 0$  can be understood by examining the dependence of the uniform state interaction energy on global rotations in LL pseudospin space:

$$\frac{2\mathcal{E}[z]}{N_\phi} = -\frac{e^2}{\varepsilon l_B} \sqrt{\frac{\pi}{2}} \left[ |z_0|^4 + \frac{3}{4} |z_1|^4 + 2|z_0|^2 |z_1|^2 \right], \quad (7.15)$$

The factor in square brackets above is  $1 - |z_1|^4/4$ , independent of  $z_1$  to quadratic order. Notice that because  $\Delta_{LL} < 0$  for  $\nu = -1, 3$  the absence of interaction

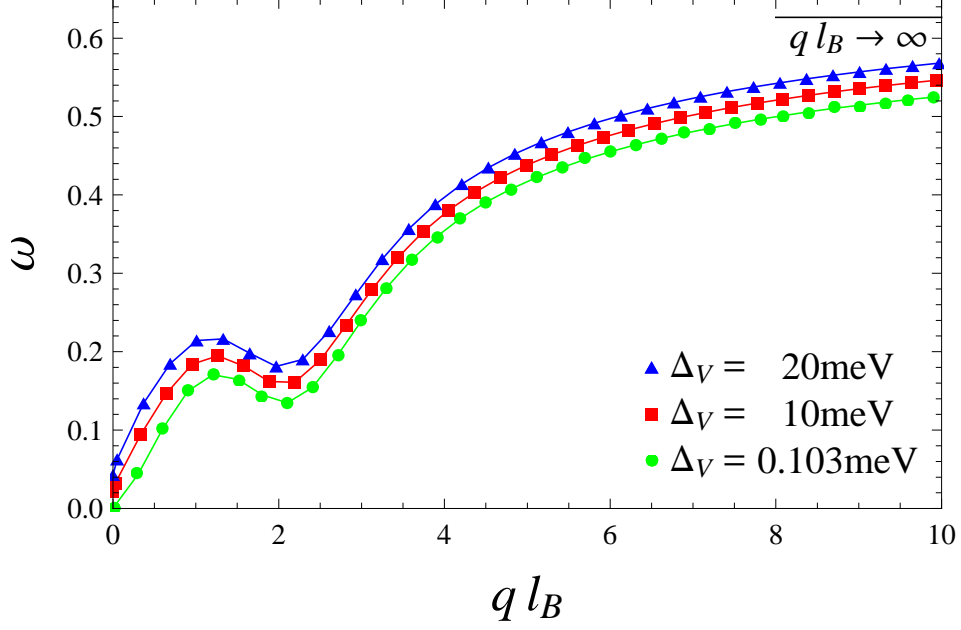


Figure 7.2: Collective mode  $\omega_q$  of the Landau-level pseudospin polarized state in units of interaction strength  $e^2/\epsilon l_B = 11.2\sqrt{B[\text{Tesla}]}$  meV as a function of  $ql_B$  at different values of the external potential difference  $\Delta_V$  at a magnetic field of 20 T. The black(solid) line indicates the  $ql_B \rightarrow \infty$  asymptote for  $\Delta_B = 0$ .

contributions to the gap implies that the fully spin-polarized state is unstable. The ground state at these filling factors is instead[93] an  $XY$  state with spontaneous phase order.

## 7.4 Intra-Landau-Level Cyclotron Resonance

Finally we show that the octet QHF will exhibit unusual intra-LL cyclotron modes at odd filling factors, focusing on the fully polarized  $\nu = -3, 1$

cases. The dynamical conductivity  $\sigma_{\pm} = \sigma_{xx} \pm i\sigma_{xy}$  can be evaluated using linear response theory. The projection of the current operator,  $j_i = d\mathcal{H}/d\pi_i$ , onto the octet space can be expressed in terms of LL pseudospins:

$$j_i = \frac{\xi\Delta_B}{m\gamma_1} \left( \frac{\hbar}{\sqrt{2}l_B} m_i + \frac{e}{c} \mathcal{A}_i^{ext}(t) \right), \quad (7.16)$$

where the *ac* electric field  $E_i = (1/c)d\mathcal{A}_i^{ext}/dt$ . The *ac* conductivity ( $\xi = 1$ ) is most simply evaluated by solving the LL pseudospin equation of motion with the  $j \cdot \mathcal{A}^{ext}$  coupling included in the energy functional. We find that

$$\sigma_{\pm}(\omega) = \frac{N_{\phi}e\Delta_B}{m\gamma_1} \frac{1}{i(\omega \pm \omega_{LL})} \quad (7.17)$$

In the absence of interactions the conductivity has intra-octet peaks at the LL band-splitting frequency  $\omega_{LL}$ , in addition to inter-Landau-level peaks which do not appear in the projected theory. The low-frequency absorption peaks should be visible in microwave absorption experiments. The appearance of tunable low-frequency peaks in  $\sigma(\omega)$  is a surprise that might be quite interesting from the point of view of the quantum Hall localization physics, even in systems for which disorder dominates interactions. In normal quantum Hall systems, peaks in  $\sigma_{\pm}$  appear near the characteristic inter-Landau-level energy  $\omega_c$  and the strong localization physics which leads to flat broad quantum Hall plateaus occurs only in systems with  $\omega_c\tau > 1$ . We conjecture that one requirement for odd-integer filling factor plateaus within the graphene bilayer octet is that  $\omega_{LL}\tau > 1$ . Since  $\omega_{LL}$  is proportional to  $\Delta_V$ , the strength of the quantum Hall effect can be tuned by a gate voltage which doesn't influence either the system's disorder or its total carrier density.

As noted in [13] trigonal warping can be neglected in broad range of magnetic fields given by  $\hbar l_B^{-1} > v_3 m$ . However it is reasonable to ask the effect of trigonal warping on the intra-LL cyclotron gap. To address this issue we performed numerical calculations on the four-band model, we find that at a magnetic field strength of  $10T$  and  $\Delta_V \approx 10meV$  the gap is reduced by  $< 2\%$ . Therefore we anticipate that the intra-LL cyclotron resonance signal to be experimentally measurable above  $10T$ .

# Chapter 8

## Conclusion

The primary focus of this thesis has been the study of electron-electron interactions in Chiral 2DEGs. There has been recent interest in these system due to the experimental observation of single layer and bilayer graphene [3, 4]. Due to the high mobility inherent of graphitic nanostructures there is tremendous promise for potential device applications [4]. These systems have unique electron-electron interactions due to the presence of chiral band eigenstates. Chiral Fermions also respond in a different way when compared to normal 2DEG electron in a magnetic field, the presence of additional degeneracies associated to the chiral band structure especially make this a unique system in terms of strongly correlated Quantum Hall Physics [33].

Quasiparticles in graphene sheets behave like massless Dirac Fermions mathematically similar QED<sub>3</sub>, interacting via non-relativistic long-range Coulomb interactions. We have developed a theory of electron-electron interactions in graphene sheets based on the random-phase-approximation. In particular we have shown that the tendency of Coulomb interactions in graphene to favor states with larger net chirality leads to suppressed spin and charge susceptibilities. This suppression is a consequence of the quasiparticle chirality switch which enhances quasiparticle velocities near the Dirac point. The renormal-

ized velocity and quasiparticle spectral weight have a weak dependence on the doping. This has important implications on density-functional applications to graphene nanostructures.

Recent ARPES [62, 63] experiments have reported a band gap in graphene which was interpreted as influence of electron-phonon [65] and electron-plasmon interactions, or as the apparent band-gap opening at the Dirac point due to substrate effects [63]. Graphene ARPES spectra are influenced by disorder, coupling to the substrate, and by electron-phonon interactions, in addition to the electron-electron interaction effects considered in this thesis. Because interactions effects scale with  $vk_F$  energy scale, while phonon effects are fixed at optical phonon energy scales, these two contributions can be separated experimentally by varying carrier density. Our RPA theory demonstrates that broad quasiparticle peaks and apparent energy gaps near the Dirac point are expected even without substrate coupling. We expect that the present RPA theory results, combined with progress in the preparation of samples suitable for ARPES or for 2D to 2D tunneling spectroscopy [69], will enable further progress.

In graphene bilayer 2DES's chiral bands lead to an additional degeneracy doubling [13] at the Fermi energy of a neutral system. This additional degeneracy leads to formation of LL dipoles, because dipole-dipole interactions are long-range, they play a dominant role in the Quantum Hall Ferromagnet long-wavelength effective action. In particular leading to nearly gapless collective modes with an approximate  $q^{3/2}$  dispersion. These systems exhibit a

very rich phase diagram with new types of topologically charged excitations currently under investigation [93]. Even more interesting is the possibility of strongly correlated states in bilayer graphene, in particular there is evidence to suggest that bilayer graphene might support novel nonabelian quantum hall states [75]. It is safe to assume that Quantum Hall Physics in bilayer graphene has more surprises in store for us to discover.

## Appendices

## Appendix A

### Graphene's Lindhard Function

The Dirac Hamiltonian for graphene in momentum space can be written as

$$H_k = v\vec{\sigma} \cdot \vec{k} \quad (\text{A.1})$$

here the fermi velocity  $v = \frac{3}{2}ta$  where  $t$  is the tight binding parameter and  $a$  is the nearest neighbor spacing in graphene's honeycomb lattice. We can define a set of gamma matrices  $\gamma_0 = i\sigma_3, \gamma_1 = -i\sigma_3\sigma_1, \gamma_2 = -i\sigma_3\sigma_2$  which defines a Clifford algebra  $\{\gamma^\mu, \gamma^\nu\} = 2g^{\mu\nu}$  (here  $g_{00} = -1, g_{0i} = g_{i0} = 0$  and  $g_{ij} = \delta_{ij}$ ). In this basis the low energy effective interacting hamiltonian for a graphene sheet is

$$H = v \sum_{\vec{k}} \bar{\psi}_{\vec{k}} i\vec{\gamma} \cdot \vec{k} \psi_{\vec{k}} + \frac{1}{2S} \sum_{\vec{q} \neq 0} \sum_{\vec{k}_1, \vec{k}_2} v(q) (\bar{\psi}_{\vec{k}_1 + \vec{q}} i\gamma_0 \psi_{\vec{k}_1} \bar{\psi}_{\vec{k}_2 - \vec{q}} i\gamma_0 \psi_{\vec{k}_2} - \hat{N}) \quad (\text{A.2})$$

where  $S$  is the sample area,  $\hat{N}$  is the total number operator,  $v(q)$  is the 2D fourier transform of the interaction potential. The one-body noninteracting Green's function defined as  $G^0(\vec{k}, \omega) = -i\langle T(\psi\bar{\psi}) \rangle$  is given by

$$\begin{aligned} G^0(\vec{k}, \omega, \mu \neq 0) &= i \frac{-\omega\gamma_0 + v\vec{\gamma} \cdot \vec{k}}{-\omega^2 + v^2k^2 - i\epsilon} - \pi \frac{-\omega\gamma_0 + v\vec{\gamma} \cdot \vec{k}}{v|\vec{k}|} \delta(\omega - v|\vec{k}|) \theta(\mu - v|\vec{k}|), \\ G^0(\vec{k}, \omega, \mu = 0) &= G^0(\vec{k}, \omega, 0) + \delta G^0(\vec{k}, \omega). \end{aligned} \quad (\text{A.3})$$

where  $\mu$  is the Fermi energy of a doped graphene sheet. The dynamical polarizability (Graphene's Lindhard function) is:

$$\begin{aligned}\chi_{\mu\nu}(|q|, \Omega, \mu \neq 0) &= -i \int \frac{d^2k}{(2\pi)^2} \frac{d\omega}{2\pi} \text{Tr}[ie\gamma_\mu G^0(\vec{k} + \vec{q}, \omega + \Omega, \mu \neq 0)ie\gamma_\nu G^0(\vec{k}, \omega, \mu \neq 0)], \\ \chi_{\mu\nu}(|q|, \Omega, \mu \neq 0) &= \chi_{\mu,\nu}^0(|q|, \Omega, 0) + \delta\chi_{\mu\nu}(|q|, \Omega)\end{aligned}\quad (\text{A.4})$$

Here  $\chi_{\mu,\nu}^0$  is the polarizability for a neutral graphene sheet with Fermi energy at coincident with the Dirac point and  $\delta\chi_{\mu,\nu}$  incorporates Pauli blocking effects due to doping. In the following we calculate the dynamical polarizability by evaluating the half-filled ( $\mu = 0$ ) case first corresponding to  $\chi_{\mu,\nu}^0$ , and then the  $\delta\chi_{\mu,\nu}$  contribution.

## A.1 Half-Filling

The free fermion propagator at half-filling with momentum  $\vec{k}$  and energy  $\omega$  is given by

$$G^0(\vec{k}, \omega, 0) = i \frac{-\omega\gamma_0 + v_F\vec{\gamma} \cdot \vec{k}}{-\omega^2 + v^2k^2 - i\epsilon}. \quad (\text{A.5})$$

The dynamical polarizability  $\chi_{\mu\nu}^0(|q|, \Omega)$  for neutral graphene is:

$$\chi_{\mu\nu}^0(|q|, \Omega) = -i \int \frac{d^2k}{(2\pi)^2} \frac{d\omega}{2\pi} \text{Tr}[ie\gamma_\mu G^0(\vec{k} + \vec{q}, \omega + \Omega, 0)ie\gamma_\nu G^0(\vec{k}, \omega, 0)]. \quad (\text{A.6})$$

We can separate the trace over the gamma matrices and define the three-dimensional vector  $k_\mu = (-\omega, v\vec{k})$  this gives the generalized three-dimensional length  $k^2 = -\omega^2 + v^2k^2$

$$\chi_{\mu\nu}^0(|q|, \Omega) = -\frac{ie^2}{v^2} \text{Tr}[\gamma^\mu \gamma^\rho \gamma^\nu \gamma^\sigma] \int \frac{d^3k}{(2\pi)^3} \frac{(k+q)_\rho k_\sigma}{(k+q)^2 k^2} \quad (\text{A.7})$$

The trace over the gamma matrices can be easily calculated using

$$\text{Tr}[\gamma^\mu \gamma^\rho \gamma^\nu \gamma^\sigma] = 2(g^{\mu\rho} g^{\nu\sigma} - g^{\mu\nu} g^{\rho\sigma} + g^{\mu\sigma} g^{\nu\rho}) \quad (\text{A.8})$$

This integral can be calculated by the well known methods commonly employed in Quantum Electrodynamics. At first glance the above integral is plagued with ultra-violet divergences, however as this is a low-energy effective theory there is a natural ultraviolet cutoff scale. We will use dimensional regularization to deal with the ultraviolet divergences thereby getting a cutoff independent expression for the dynamic polarizability. Using Feynman parameters this integral can be written as

$$\chi_{\mu\nu}(|q|, \Omega) = -\frac{ie^2}{v^2} \int \frac{d^3k}{(2\pi)^3} \int_0^1 dx \frac{2[(k+q)_\mu k_\nu + (k+q)_\nu k_\mu - g_{\mu\nu}(k+q) \cdot k]}{[(k+q)^2 x + (1-x)k^2]^2}. \quad (\text{A.9})$$

We can complete the square and write the denominator as

$$x(k+q)^2 + (1-x)k^2 = (k+xq)^2 + q^2 x(1-x), \quad (\text{A.10})$$

defining a new momentum  $l \equiv k+xq$ , we can see that the denominator just depends on  $l^2$ . Integrating over  $d^3k = d^3l$  is becomes easier as the integrand is spherically symmetric with respect to  $l$ . Performing this shift  $k \rightarrow l-xq$ , the integral becomes

$$\chi_{\mu\nu} = -\frac{ie^2}{v^2} \int \frac{d^3l}{(2\pi)^3} \int_0^1 dx \frac{2l_\mu l_\nu - 2q_\mu q_\nu x(1-x) - g_{\mu\nu}(l^2 + q^2 x(1-x))}{[l_E^2 + \Delta]^2} \quad (\text{A.11})$$

where  $\Delta \equiv q^2 x(1-x)$ . Employing symmetry considerations gives that terms in the numerator containing odd powers in  $l$  vanishes, the rest can be evaluated

from the general formula. I will also perform this integral in Euclidean space  $d^3l \rightarrow id^3l_E$

$$\chi_{\mu\nu}(|\vec{q}|, \Omega) = \frac{2e^2}{v^2} \int_0^1 dx \int \frac{d^3l_E}{(2\pi)^3} \frac{-1/3g_{\mu\nu}l_E^2 + (q^2g_{\mu\nu} - 2q_\mu q_\nu)x(1-x)}{[l_E^2 + \Delta]^2} \quad (\text{A.12})$$

Using

$$\int \frac{d^d l_E}{(2\pi)^d} \frac{1}{[l_E^2 + \Delta]^n} = \frac{(-1)^n}{(4\pi)^{d/2}} \frac{\Gamma(n - \frac{d}{2})}{\Gamma(n)} \left(\frac{1}{\Delta}\right)^{n - \frac{d}{2}} \quad (\text{A.13})$$

$$\int \frac{d^d l_E}{(2\pi)^d} \frac{l_E^2}{[l_E^2 + \Delta]^n} = \frac{(-1)^n}{(4\pi)^{d/2}} \frac{d}{2} \frac{\Gamma(n - \frac{d}{2} - 1)}{\Gamma(n)} \left(\frac{1}{\Delta}\right)^{n - \frac{d}{2} - 1} \quad (\text{A.14})$$

which gives

$$\chi_{\mu\nu}(|\vec{q}|, \Omega) = -\frac{|q|}{2\pi v^2} \left(g_{\mu\nu} - \frac{q_\mu q_\nu}{q^2}\right) \int_0^1 dx \sqrt{x(1-x)} \quad (\text{A.15})$$

Restricting ourselves to the special case of Coulomb interaction  $\mu = \nu = 0$

$$\chi_{00}(|\vec{q}|, \Omega) = \frac{\vec{q}^2}{16\sqrt{v^2q^2 - \Omega^2}} \Theta(v^2q^2 - \Omega^2) + i \frac{\vec{q}^2}{16\sqrt{\Omega^2 - v^2q^2}} \Theta(\Omega^2 - v^2q^2) \quad (\text{A.16})$$

and analytically continuing  $\Omega \rightarrow i\Omega$  just gives

$$\chi_{00}(|\vec{q}|, i\Omega) = \frac{\vec{q}^2}{16\sqrt{v^2q^2 + \Omega^2}} \quad (\text{A.17})$$

This gives the Lindhard function for neutral graphene.

## A.2 Pauli-blocking effects

To calculate the  $\mu \neq 0$  contribution to the dynamical polarizability we specifically restrict to Coulomb interaction, the numerator in the second term

of A.4 is:

$$Tr[\gamma^0(-\omega\gamma_0 + v\vec{\gamma} \cdot \vec{k})\gamma^0(-(\omega + \Omega\gamma_0 + v\vec{\gamma} \cdot \vec{k} + q)] \quad (\text{A.18})$$

This trace can be easily calculated with the help of the definition of the Clifford algebra which gives

$$Tr[\gamma^0\gamma^0\gamma^0\gamma^0] = 2 \quad Tr[\gamma^0\gamma^i\gamma^0\gamma^0] = Tr[\gamma^0\gamma^0\gamma^0\gamma^j] = 0 \quad Tr[\gamma^0\gamma^i\gamma^0\gamma^j] = 2\delta_{ij} \quad (\text{A.19})$$

giving us

$$Tr[\gamma^0(-\omega\gamma_0 + v\vec{\gamma} \cdot \vec{k})\gamma^0(-(\omega + \Omega\gamma_0 + v\vec{\gamma} \cdot \vec{k} + q)] = 2[\omega(\omega + \Omega) + v^2\vec{k} \cdot \vec{k} + q] \quad (\text{A.20})$$

The crossterm (the imaginary times the real part of the greens function) call this term  $\delta\chi_{oo}$

$$\begin{aligned} \delta\chi_{oo}(|\vec{q}|, \Omega) &= ie^2 \int \frac{d^2k}{(2\pi)^2} \int \frac{d\omega}{2\pi} - i\pi \left[ \frac{2[\omega(\omega + \Omega) + v^2\vec{k} \cdot \vec{k} + \vec{q}]\delta(\omega - v|\vec{k}|)\theta(\mu - v|\vec{k}|)}{[-(\omega + \Omega)^2 + v^2|\vec{k} + \vec{q}|^2 - i\epsilon]v|\vec{k}|} \right. \\ &\quad \left. + \frac{2[\omega(\omega + \Omega) + v^2\vec{k} \cdot \vec{k} + \vec{q}]\delta(\omega + \Omega - v|\vec{k} + \vec{q}|)\theta(\mu - v|\vec{k} + \vec{q}|)}{[-\omega^2 + v^2|\vec{k}|^2 - i\epsilon]v|\vec{k} + \vec{q}|} \right] \quad (\text{A.21}) \end{aligned}$$

Using the delta function to perform the frequency integral and shifting the momentum  $\vec{k} \rightarrow -\vec{k} + \vec{q}$  in the second term of the ?? and analytically continuing  $\Omega \rightarrow i\Omega$

$$\delta\chi_{oo} = \frac{e^2}{v} \int_0^{\mu/v} \frac{dk}{2\pi} \int_0^{2\pi} \frac{d\theta}{2\pi} \left[ \frac{2k^2 + qk \cos \theta + i\tilde{\Omega}|\vec{k}|}{2qk \cos \theta + (\tilde{\Omega}^2 + q^2) - 2i\tilde{\Omega}|\vec{k}|} + \frac{2k^2 + qk \cos \theta - i\tilde{\Omega}|\vec{k}|}{2qk \cos \theta + (\tilde{\Omega}^2 + q^2) + 2i\tilde{\Omega}|\vec{k}|} \right] \quad (\text{A.22})$$

in the above we scale the frequency by defining  $\tilde{\Omega} = \Omega/v$ , and align  $k_x$  in the direction of  $\vec{q}$ . We perform the above angular integral by substituting  $z = e^{i\theta}$

and  $\cos\theta = \frac{z+z^{-1}}{2}$  and using the identities

$$\int_0^{2\pi} \frac{d\theta}{a \cos \theta + b} = \frac{2\pi \operatorname{sgn}(|z_-| - |z_+|)}{\sqrt{b^2 - a^2}} \quad (\text{A.23})$$

$$\int_0^{2\pi} \frac{\cos \theta d\theta}{a \cos \theta + b} = \frac{2\pi}{a} - \frac{2\pi b \operatorname{sgn}(|z_-| - |z_+|)}{a\sqrt{b^2 - a^2}} \quad (\text{A.24})$$

where  $|z_{\pm}| = \frac{1}{a}(-b \pm \sqrt{b^2 - a^2})$ .  $\delta\chi_{oo}$  then becomes

$$\delta\chi_{oo} = \frac{e^2\mu}{2\pi v^2} + \frac{e^2}{v\sqrt{\tilde{\Omega}^2 + q^2}} \int_0^{\mu/v} \frac{dk}{2\pi} \left[ \frac{2k^2 - (\tilde{\Omega}^2 + q^2)/2 + 2i\tilde{\Omega}k}{\sqrt{(\tilde{\Omega}^2 + q^2 - 4k^2) - 4i\tilde{\Omega}k}} + \frac{2k^2 - (\tilde{\Omega}^2 + q^2)/2 - 2i\tilde{\Omega}k}{\sqrt{(\tilde{\Omega}^2 + q^2 - 4k^2) + 4i\tilde{\Omega}k}} \right] \quad (\text{A.25})$$

The two integrands above are complex conjugates which implies that  $\delta\chi_{oo}$  purely real. This integral can be written in a compact analytical form as

$$\delta\chi_{oo} = \frac{e^2\mu}{2\pi v^2} - \frac{e^2\bar{q}^2}{16\pi\sqrt{\Omega^2 + v^2q^2}} \operatorname{Re} \left[ \sin^{-1} \left( \frac{2\mu + i\Omega}{v|q|} \right) + \left( \frac{2\mu + i\Omega}{v|q|} \right) \sqrt{1 - \left( \frac{2\mu + i\Omega}{v|q|} \right)^2} \right] \quad (\text{A.26})$$

So the full  $\chi_{00} = \chi_{00}^0(\mu = 0) + \delta\chi_{oo}(\mu \neq 0)$  is given by

$$\begin{aligned} \chi_{00}(|\vec{q}|, i\Omega, \mu \neq 0) &= \frac{e^2q^2}{16\sqrt{\Omega^2 + v^2q^2}} + \frac{e^2\mu}{2\pi v^2} \quad (\text{A.27}) \\ &- \frac{e^2\bar{q}^2}{8\pi\sqrt{\Omega^2 + v^2q^2}} \operatorname{Re} \left[ \sin^{-1} \left( \frac{2\mu + i\Omega}{v|q|} \right) + \left( \frac{2\mu + i\Omega}{v|q|} \right) \sqrt{1 - \left( \frac{2\mu + i\Omega}{v|q|} \right)^2} \right] \end{aligned}$$

In the static limit ( $\Omega = 0$ ,  $q \rightarrow 0$ ) the above expression correctly reduces to the noninteracting density of states per valley per spin at the Fermi energy  $D(\epsilon) = \mu/2\pi v^2$ . Two limiting cases for A.27 are of particular interest

$$\lim_{\Omega \rightarrow \infty} \chi_{00}(|\vec{q}|, i\Omega, \mu \neq 0) = \frac{q^2}{16\Omega} + \mathcal{O}\left(\frac{1}{\Omega^2}\right) \quad (\text{A.28})$$

$$\lim_{q \rightarrow \infty} \chi_{00}(|\vec{q}|, i\Omega, \mu \neq 0) = \frac{q}{16v} \quad (\text{A.29})$$

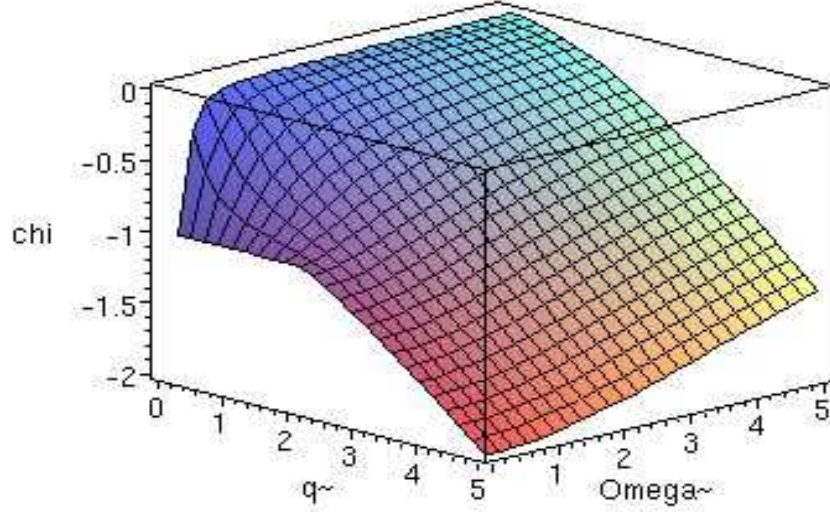


Figure A.1: The surface plot shows graphene's Lindhard function for  $\tilde{\Omega} = \Omega/\mu$  and  $\tilde{q} = q/v$

The above expression indicate the divergences that need to be regularized in the calculation for the energy and other observables. The low energy theory of graphene described by massless Dirac Fermions has a natural ultraviolet divergence that needs to be regularized by a momentum scale cutoff  $\Lambda$  at large  $q$ . Graphene's Lindhard function for  $q$  and  $\Omega$  is plotted in the figure

## Appendix B

### Correlation Self-energy of a quasiparticle in graphene

The random phase approximation(RPA) self-energy of an electron in a graphene layer can be written as

$$\Sigma_s^{RPA}(k, ik_n) = \sum_{s'=\pm} \frac{i}{A} \sum_{\vec{q}} v_q \frac{1}{\beta} \sum_{i\Omega_n} \frac{\mathcal{G}_{s'}^0(\vec{k} + \vec{q}, ik_n + i\Omega_n)}{\epsilon_{RPA}(q, i\Omega_n)} \left( \frac{1 + ss' \cos(\theta)}{2} \right) \quad (\text{B.1})$$

$\epsilon_{RPA}(q, i\Omega_n) = 1 - v_q \Pi(q, i\Omega_n)$  where  $\Pi(q, i\Omega_n)$  is the polarization bubble calculated earlier,  $s, s'$  denote the band indices and  $\theta$  is the angle between  $\vec{k}$  and  $\vec{k} + \vec{q}$ . Here  $\mathcal{G}_{s'}^0(\vec{k} + \vec{q}, ik_n + i\Omega_n)$  is the finite temperature greens function for the quasiparticle.  $\Sigma_s^{RPA}$  can be separated into  $\Sigma_s^{RPA} = \Sigma_s^{HF} + \Sigma_s^{corr}$  as

$$\Sigma_s^{RPA}(k, ik_n) = \sum_{s'=\pm} \frac{i}{A} \sum_{\vec{q}} \frac{1}{\beta} \sum_{i\Omega_n} \mathcal{G}_{s'}^0(\vec{k} + \vec{q}, ik_n + i\Omega_n) \left( \frac{1 + ss' \cos(\theta)}{2} \right) \left[ \frac{v_q}{1 - v_q \Pi(q, i\Omega_n)} + v_q - v_q \right] \quad (\text{B.2})$$

where  $\Sigma_s^{corr}$  is given as

$$\Sigma_s^{corr}(k, ik_n) = \sum_{s'=\pm} \frac{i}{A} \sum_{\vec{q}} \frac{1}{\beta} \sum_{i\Omega_n} \mathcal{G}_{s'}^0(\vec{k} + \vec{q}, ik_n + i\Omega_n) \left( \frac{1 + ss' \cos(\theta)}{2} \right) \left[ \frac{v_q^2 \Pi(q, i\Omega_n)}{1 - v_q \Pi(q, i\Omega_n)} \right] \quad (\text{B.3})$$

The greens function is given by

$$\mathcal{G}_{s'}^0(\vec{k} + \vec{q}, ik_n + i\Omega_n) = \frac{i}{ik_n + i\Omega_n - \xi_{\vec{k} + \vec{q}, s'}} \quad (\text{B.4})$$

where  $\xi_{\vec{k},s'} = s'|\vec{k}| - \mu$  is the energy measured from the fermi energy  $\mu$ .

$$\Sigma_s^{corr}(k, ik_n) = - \sum_{s'=\pm} \frac{1}{A} \sum_{\vec{q}} v_q^2 \left( \frac{1 + ss' \cos(\theta)}{2} \right) \frac{1}{\beta} \sum_{i\Omega_n} \frac{1}{ik_n + i\Omega_n - \xi_{\vec{k}+\vec{q},s'}} \frac{\Pi(q, i\Omega_n)}{1 - v_q \Pi(q, i\Omega_n)} \quad (\text{B.5})$$

Here we are interested in evaluating retarded self-energy of the quasiparticle obtained by setting  $ik_n \rightarrow \xi_{\vec{k},s} + i\eta$  as step towards evaluating the self-energy at the fermi surface. Unfortunately the processes of summation over Matsubara frequencies and analytic continuation do not commute. We can however express the final retarded function as two terms:

$$\Sigma_s^{corr}(k, \xi_{\vec{k},s}) = \Sigma_s^{line}(k, \xi_{\vec{k},s}) + \Sigma_s^{res}(k, \xi_{\vec{k},s}) \quad (\text{B.6})$$

$\Sigma_s^{line}$  is the term that is obtained if we were allowed to interchange the two steps of analytical continuation and contour intergration

$$\Sigma_s^{line}(k, \xi_{\vec{k},s}) = - \sum_{s'=\pm} \int \frac{d^2q}{(2\pi)^2} v_q^2 \left( \frac{1 + ss' \cos(\theta)}{2} \right) \int \frac{d\Omega}{2\pi} \frac{1}{i\Omega + \xi_{\vec{k},s} - \xi_{\vec{k}+\vec{q},s'}} \frac{\Pi(q, i\Omega)}{1 - v_q \Pi(q, i\Omega)} \quad (\text{B.7})$$

then  $\Sigma_s^{res}$  is just the contribution one gets by interchanging the orders of the two steps of analytical continuation and frequency summation, below I show that  $\Sigma_s^{res}$  evaluated at the fermi energy is zero. Let us examine the frequency integral

$$\begin{aligned} I_{ss',k}(ik_n) &= \int_{-\infty}^{+\infty} \frac{d\Omega}{2\pi} f(i\Omega) \left( \frac{1}{i\Omega + \xi_{\vec{k},s} - \xi_{\vec{k}+\vec{q},s'}} - \frac{1}{ik_n + i\Omega - \xi_{\vec{k}+\vec{q},s'}} \right) \\ f(i\Omega) &= \frac{\Pi(q, i\Omega)}{1 - v_q \Pi(q, i\Omega)} \end{aligned} \quad (\text{B.8})$$

where

$$\Sigma_s^{res}(k, ik_n) = - \sum_{s=\pm} \int \frac{d^2q}{(2\pi)^2} v_q^2 \left( \frac{1 + ss' \cos(\theta)}{2} \right) I_{ss',k}(ik_n) \quad (\text{B.9})$$

Similar to the electron gas situation the poles of  $f(i\Omega)$  and its branch cuts give no contribution to  $I_{s,k}(ik_n)$ . For example that  $f(i\Omega)$  has a simple pole at  $\Omega = \Omega_j$  with residue  $A_j$  then

$$I_{ss',k}(ik_n) = \int_{-\infty}^{+\infty} \frac{d\omega}{2\pi i} \frac{A_j}{\Omega - \Omega_j} \left( \frac{1}{\Omega - i(\xi_{\vec{k},s} - \xi_{\vec{k}+\vec{q},s'})} - \frac{1}{\Omega + k_n + i\xi_{\vec{k}+\vec{q},s'}} \right) \quad (\text{B.10})$$

The  $d\Omega$  integral can be done by taking a semi-circular contour in the upper half plane (note that this choice is arbitrary and closing the contour in the lower half plane does not change our conclusions)

$$\begin{aligned} I_{ss',k}(ik_n) &= A_j \left[ \frac{1}{\Omega_j - i(\xi_{\vec{k},s} - \xi_{\vec{k}+\vec{q},s'})} + \frac{1}{\Omega_j + k_n + i\xi_{\vec{k}+\vec{q},s'}} \right] \quad (\text{B.11}) \\ &+ \frac{\Theta(\xi_{\vec{k},s} - \xi_{\vec{k}+\vec{q},s'}) A_j}{i(\xi_{\vec{k},s} - \xi_{\vec{k}+\vec{q},s'}) - \Omega_j} - \frac{\Theta(-\xi_{\vec{k}+\vec{q},s'}) A_j}{-k_n - i\xi_{\vec{k}+\vec{q},s'} - \Omega_j} \end{aligned}$$

Analytic continuation  $ik_n \rightarrow \xi_{\vec{k},s} + i\eta$  then just gives

$$I_{ss',k}(\xi_{\vec{k},s}) = A_j \left[ \frac{\Theta(\xi_{\vec{k},s} - \xi_{\vec{k}+\vec{q},s'})}{i(\xi_{\vec{k},s} - \xi_{\vec{k}+\vec{q},s'}) - \Omega_j} - \frac{\Theta(-\xi_{\vec{k}+\vec{q},s'})}{i(\xi_{\vec{k},s} - \xi_{\vec{k}+\vec{q},s'} - \Omega_j)} \right] \quad (\text{B.12})$$

thus  $\Sigma^{res}(\xi_{\vec{k},s})$  just becomes

$$\begin{aligned} \Sigma_s^{res}(k, \xi_{\vec{k},s}) &= - \sum_{s'=\pm} \int \frac{d^2q}{(2\pi)^2} v_q^2 \left( \frac{1 + ss' \cos(\theta)}{2} \right) \frac{\Pi(q, \xi_{\vec{k},s} - \xi_{\vec{k}+\vec{q},s'})}{1 - v_q \Pi(q, \xi_{\vec{k},s} - \xi_{\vec{k}+\vec{q},s'})} \quad (\text{B.13}) \\ &[\Theta(\xi_{\vec{k},s} - \xi_{\vec{k}+\vec{q},s'}) - \Theta(-\xi_{\vec{k}+\vec{q},s'})] \end{aligned}$$

# Bibliography

- [1] R. Shankar. *Rev. Mod. Phys.*, 66:129, 1994.
- [2] P.W. Anderson. *Science*, 177:393, 1972.
- [3] K.S. Novoselov, A. K. Geim, S. V. Morozov, D. Jiang, M. I. Katsnelson, I. V. Grigorieva, S. V. Dubonos, A. A. Firsov. *Nature*, 438:197 2005.
- [4] Y.B. Zhang, Yan-Wen Tan, Horst L. Stormer, Philip Kim. *Nature*, 438:201 2005.
- [5] K. S. Novoselov, E. McCann, S. V. Morozov, V. I. Fal'ko, M. I. Katsnelson, U. Zeitler, D. Jiang, F. Schedin, A. K. Geim. *Nature Physics*, 2:177 (2006).
- [6] Y. Barlas, T. Pereg-Barnea, M. Polini, R. Asgari and A.H. MacDonald. *Phys. Rev. Lett.*, 98:236601 2007.
- [7] O. Vafek. *Phys. Rev. Lett.*, 99:047002 2007.
- [8] J. Gonzales, F. Guinea, and M.A.H. Vozmediano. *Phys. Rev. B* 59:2474 1999.
- [9] For a recent popular review see A.K. Geim and A.H. MacDonald. *Physics Today*, 60(8):35 2007.

- [10] A. H. Castro Neto, F. Guinea, N. M. R. Peres, K. S. Novoselov, A. K. Geim. *cond-mat/0709.1163*, 2007
- [11] T. Pereg-Barnea and M. Franz. *Phys. Rev. B*, 67:060503(R) 2003.
- [12] H. Min and A.H. MacDonald. *Phys. Rev. B* 77:155416 2008.
- [13] E. McCann and V. I. Fal'ko. *Phys. Rev. Lett.*, 96:086805 2006.
- [14] K. S. Novoselov, A. K. Geim, S. V. Morozov, D. Jiang, Y. Zhang, S. V. Dubonos, I. V. Grigorieva, and A. A. Firsov. *Science*, 306:666 2004.
- [15] P. R. Wallace. *Phys. Rev.*, 71:622
- [16] G.W. Semenoff. *Phys. Rev. Lett.*, 53:2449 1984.
- [17] E. Fradkin. *Phys. Rev. B*, 33:3263 1986.
- [18] F.D.M. Haldane. *Phys. Rev. Lett.* 61:2015 1988.
- [19] A. Calogeracos and N. Dombey. *Comtemp. Phys.*, 40:313 1999
- [20] C. Itzykson and J.B. Zuber. *Quantum Field Theory* Dover 2006.
- [21] Marco Polini, Reza Asgari, Yafis Barlas, Tami Pereg-Barnea and A.H.MacDonald. *Solid State Comm.* 143:58 2007.
- [22] M. Y. Han, B. zyilmaz, Y. Zhang, and P. Kim *Phys. Rev. Lett.* 98:206805 2007.
- [23] N.W. Ashcroft and N.D. Mermin. *Solid State Physics*, Saunders, 1976.

- [24] M.E. Peskin and D.V. Schroeder. *An Introduction to Quantum Field Theory*, Addison-Wesley Advanced, 1995
- [25] E. McCann. *Phys. Rev.B*, 71:161403(R), 2006
- [26] T. Ohta, A. Bostwick, T. Seyller, K. Horn, and E. Rotenberg. *Science* 313:951 2006.
- [27] B. Sahu, H. Min, A. H. MacDonald and S. K. Banerjee. *Phys. Rev. B* 78:045404 2008.
- [28] Hongki Min, Giovanni Borghi, Marco Polini and A.H. MacDonald. *Phys. Rev. B* 77:041407(R) 2008.
- [29] H. P. Dahal, T. O. Wehling, K. S. Bedell, J.-X. Zhu, and A. V. Balatsky *cond-mat/0706.1689*, 2007.
- [30] J. Nilsson, A. H. Castro Neto, N. M. R. Peres and F. Guinea. *Phys. Rev. B* 73:214418 (2006)
- [31] K. Nomura and A.H. MacDonald. *Phys. Rev. Lett.*, 96:256602 2006.
- [32] J. Alicea and M.P.A. Fisher. *Phys. Rev. B*, 74:075422 2006.
- [33] Y. Barlas, R. Cote, K. Nomura and A.H.MacDonald. *cond-mat/0803.0044* 2008.
- [34] K. von Klitzing, G. Dorda, M. Pepper. *Phys. Rev. Lett.*, 45:494 1980.
- [35] R. B. Laughlin. *Phys. Rev. B*. 23:5632 1981.

- [36] D.C. Tsui, H.L. Stormer, and A.C. Gossard. *Phys. Rev. Lett.*, 48:1559 1982.
- [37] R.B. Laughlin. *Phys. Rev. Lett.*, 50:1395 (1983)
- [38] K. S. Novoselov, Z. Jiang, Y. Zhang, S. V. Morozov, H. L. Stormer, U. Zeitler, J. C. Maan, G. S. Boebinger, P. Kim and A. K. Geim. *Science* 315:1379 2007
- [39] J. C. Slonczewski and P. R. Weiss. *Phys. Rev.* 109:272 1958.
- [40] G.F. Giuliani and G. Vignale, *Quantum Theory of the Electron Liquid* Cambridge University Press, Cambridge, 2005.
- [41] The density-density response function  $\chi^{(0)}$  of the doped two-dimensional MDF model was first considered by K.W.-K. Shung, *Phys. Rev. B* 34:979 1986 as a step toward a theory of collective excitations in graphite. The MDF  $\chi^{(0)}$  expression has been reconsidered recently by ourselves and by others with an eye toward applications to single layer graphene properties: X.F. Wang and T. Chakraborty, *cond-mat/0605498*; B. Wunsch, T. Stauber, F. Sols, and F. Guinea, *cond-mat/0610630*; E.H. Hwang and S. Das Sarma, *Phys. Rev. B* 75:205418 2007.
- [42] See for example Fig. 1 in Hongki Min *et al.*, *Phys. Rev. B* 74:165310 2006.
- [43] See for example J.P. Eisenstein, L.N. Pfeiffer, and K.W. West, *Phys. Rev. B* 50:1760 1994 and S.I. Dorozhkin *et al.*, *Phys Rev B* 63:121301 2001; S.

- Ilani *et al.*, *Phys. Rev. Lett.* 84:3133 2000; Similar measurements have recently been performed on carbon nanotubes: S. Ilani *et al.* *Nature Physics* 2:687 2006.
- [44] V.M. Pudalov *et al.*, *Phys. Rev. Lett.* 88:196404 2002; K. Vakili *et al.*, *ibid.* 92:226401 2004; A.A. Shashkin *et al.*, *ibid.* 96:036403 2006; Y.-W. Tan *et al.*, *Phys. Rev. B* 73:045334 2006.
- [45] The tendency of exchange interactions to suppress the spin-susceptibility at small doping was noted previously in a Hartree-Fock approximation at low doping by N.M.R. Perez, F. Guinea, and A.H. Castro-Neto, *Phys. Rev. B* 72:174406 2005.
- [46] D.Pines and P. Nozieres. *The Theory of Quantum Liquids*, Addison-Wesley, Menlo Park, 1996.
- [47] E. Tutuc, S. Melinte, and M. Shayegan. *Phys. Rev. Lett.* 88:036805 2002
- [48] J. Zhu *et al.*. *Phys. Rev. Lett.* 90:056805 2003.
- [49] Y.W. Tan. *et al.*. *Phys. Rev. B* 73:045334 2006.
- [50] S.D. Palo. *et al.*. *Phys. Rev. Lett* 94:226405 2005.
- [51] R. Asgari. *et al.*. *Phys. Rev. B* 71:045323 2005
- [52] For a through discussion of the random phase approximation applied to ordinary electron see [40]. The random phase approximation for the Fermi liquid properties of graphene has also been discussed recently by S.D.

Sarma, E.H. Hwang and W.K. Tse *Phys. Rev. B* 75:121406(R) 2007.  
The results presented here differ in several important aspects, but both works agree that doped graphene is a Fermi liquid.

- [53] J. Gonzalez, F. Guinea, and M.A.H. Vozmediano. *Phys. Rev. B* 59:2474(R) 1999.
- [54] T.M. Rice. *Ann. Phys.*, 31:100 1965.
- [55] V. Barone *et al.* *Phys. Rev. B* 74:195417 2006.
- [56] Y.W. Son *et al.* *Nature* 44:347 2006.
- [57] P.G. Silvestrov and K.B. Efetov *Phys. Rev. Lett* 98:016802 2007.
- [58] A.D. Martino *et al.* *Phys. Rev. Lett* 98:066802 2007.
- [59] A.K. Geim and K.S. Novoselov, *Nat. Mat.*, 6:183 2007;
- [60] M.I. Katnelson and K.S. Novoselov, *Solid State Commun.* , 143:3 2007.
- [61] A. Damascelli, Z. Hussain, and Z.-X. Shen. *Rev. Mod. Phys.*, 75:473 2003.
- [62] A. Bostwick *et al.*, *Nat. Phys.*, 3:36 2007.
- [63] S. Y. Zhou *et al.* *Nat. Mater.* 6:770 2007.
- [64] For a review on the properties of epitaxial graphene see W.A. de Heer *et al.*, *Solid State Commun.*, 143:92 2007.

- [65] C.-H. Park, F. Giustino, M. L. Cohen, and S. G. Louie. *Phys. Rev. Lett.*, 99:086804, 2007; W.-K. Tse and S. Das Sarma. *ibid.* 99:236802, 2007; M. Calandra and F. Mauri, *Phys. Rev. B*, 76:205411, 2007.
- [66] J. Gonzales, F. Guinea, and M.A.H. Vozmediano, *Phys. Rev. B* 59:2474 1999; M.I. Katsnelson, *Eur. Phys. J. B* 52:151 2006; E.G. Mishchenko, *Phys. Rev. Lett.* 98:216801 2007; O. Vafek, *Phys. Rev. Lett.* 98:216401 2007; S. Das Sarma, E.H. Hwang, and W.-K. Tse, *Phys. Rev. B* 75:121406(R) 2007; X.-Z. Yan and C.S. Ting, arXiv:0705.2752v1; D.E. Sheehy and J. Schmalian, arXiv:0707.2945v1.
- [67] E.H. Hwang, B.Y.-K. Hu, and S. Das Sarma, cond-mat/0612345.
- [68] B. Lundqvist, *Phys. Kondens. Mater.* 6:193 1967; L Hedin *et. al.*, *Solid State Comm.* 5:237 1967; R. Jalabert and S. Das Sarma, *Phys. Rev. B* 40:9723 1989.
- [69] S.Q. Murphy, J.P. Eisenstein, L.N. Pfeiffer and K.W. West. *Phys. Rev. B* 52:14825 1995
- [70] Interested reader can look at some excellent reviews on this subject A.H. MacDonald. *cond-mat/9410047*, 1994.
- [71] K Yang. *Quantum Hall Physics in low-dimensional strongly correlated systems*, PhD thesis, Indiana University.
- [72] F.D.M. Haldane. *Phys. Rev. Lett.*, 51:605 1983.

- [73] B.I. Halperin. *Phys. Rev. Lett.*, 52:1583 1984.
- [74] J.K. Jain *Phys. Rev. Lett.*, 63:1999 1989.
- [75] C. Nayak, S. H. Simon, A. Stern, M. Freedman and S.D. Sarma. *cond-mat/0707.1889* 2007
- [76] See for example *Perspectives in Quantum Hall Effects* edited by S.D. Sarma and A. Pinczuk, Wiley, New York, 1996.
- [77] S.L. Sondhi, A. Karlhede, E. H. Rezayi and S. A. Kivelson *Phys. Rev.B*, 47:16419 1993.
- [78] S.M. Girvin and A.H. MacDonald in [76].
- [79] A.H. MacDonald, P.M. Platzman, and G.S. Boebinger. *Phys. Rev. Lett.*, 65:775 1990.
- [80] J. Eisenstein and A.H. MacDonald. *Nature*, 432:691, 2004.
- [81] K. Yang, K. Moon, L. Zheng, A.H. MacDonald, S.M. Girvin, D. Yoshioka, and S.C. Zhang. *Phys. Rev. Lett.*, 72:732, 1994.
- [82] C. Kallin and B. I. Halperin, *Phys. Rev. B* **30**, 5655 (1984).
- [83] S. L. Sondhi *et. al.*, *Phys. Rev. B* **47**, 16419 (1993); I. Aleiner and L. I. Glazman, *Phys. Rev. B* **52**, 11296 (1995); M. M. Fogler and B. I. Shklovskii, *Phys. Rev. B* **52** 17366 (1995); B.A. Piot *et al.* *Phys. Rev. B.* **72**, 245325 (2005); B.A. Piot *et al.* *Phys. Rev. B.* **75**, 155332 (2007).

- [84] K. Moon *et al.*, Phys. Rev. B **51**, 5138 (1995).
- [85] T. Jungwirth and A. H. MacDonald, Phys. Rev. B **63**, 035305 (2000).
- [86] H. A. Fertig, Phys. Rev. B **40**, 1087 (1989); A. H. MacDonald, P. M. Platzman and G. S. Boebinger, Phys. Rev. Lett. **65**, 775 (1990).
- [87] A. H. MacDonald, Physica B, **298**, 129 (2001).
- [88] L. Zheng, R. J. Radtke and S. D. Sarma, Phys. Rev. Lett, **78**, 2453 (1997); S. D. Sarma, S. Sachdev and L. Zheng, *ibid.* **79**, 917 (1997); A. H. MacDonald, R. Rajaraman and T. Jungwirth, Phys. Rev. B **60**, 8817 (1999).
- [89] K. Nomura and A. H. MacDonald, Phys. Rev. Lett. **96**, 256602 (2006).
- [90] As shown in [5], the neglect of the trigonal warping effect is justified in a sufficiently strong magnetic field.
- [91] Since the K valley states in the octet are localized in the top (t) layer, and the K' valley states are localized in the bottom (b) layer, the valley (K,K') degree of freedom is equivalent to the layer (t,b) degree of freedom.
- [92] The derivation of the octet HF Hamiltonian differs from those for other quantum Hall ferromagnets (see for example A. H. MacDonald, J. Phys. C: Solid State Phys. **18**, 1003 (1985)) only in details related to the specific character of orbitals in the Hilbert space.

- [93] Y. Barlas, Jules Lambert, R. Côté, and A. H. MacDonald, (in preparation).
- [94] See for example Assa Auerbach, *Interacting Electrons and Quantum Magnetism*, (Springer, 1994).
- [95] A. A. Burkov and A. H. MacDonald, Phys. Rev. B **66**, 115320 (2002).

# Index

Abstract,	vi
<i>Acknowledgments,</i>	v
<i>Appendices,</i>	80
<i>Bibliography,</i>	91
<i>Correlation Self-energy of a quasi- particle in graphene,</i>	88
<i>Dedication,</i>	iv
<i>Graphene's Lindhard Function,</i>	81
<i>Chiral Hamiltonian,</i>	1

# Vita

Yafis Barlas was born in Karachi, Pakistan the son of Mirza Shahid Barlas and Anwer Barlas. He recieved a B.S. degree in Physics and Mathematics from University of Houston in May 2002. In August 2002 he joined Graduate School at Univerity of Texas at Austin to pursue a PhD in Physics.

Permanent address: 701 W North Loop Apt 106  
Austin, Texas 78751

This dissertation was typeset with L<sup>A</sup>T<sub>E</sub>X<sup>†</sup> by the author.

---

<sup>†</sup>L<sup>A</sup>T<sub>E</sub>X is a document preparation system developed by Leslie Lamport as a special version of Donald Knuth's T<sub>E</sub>X Program.